THE UNIVERSITY THOUGHT

PUBLICATION IN NATURAL SCIENCES

VOL. 9, N⁰ 2, 2019.

Aims and Scope

The University Thought - Publication in Natural Sciences (Univ. thought, Publ. nat. sci.) is a scientific journal founded in 1994. by the University of Priština, and was published semi annually until 1998.

Today, the University Thought - Publication in Natural Sciences is an international, peer reviewed, Open Access journal, published semi annually in the online and print version by the University of Priština, temporarily settled in Kosovska Mitrovica, Serbia. The Journal publishes articles on all aspects of research in Biology, Chemistry, Geography, Information technologies, Mathematics and Physics in the form of original papers, short communications and reviews (invited) by authors from the country and abroad.

The University Thought - Publication in Natural Sciences serves as an interdisciplinary forum covering a wide range of topics for a truly international audience. Journal is endeavor of the University of Priština to acquaint the scientific world with its achievements and wish to affirm the intellectual potential and natural resources of own region. Our aim is to put forward attitude of principle that science is universal and we invite all scientists to cooperate wherever their scope of research may be. We are convinced that shall contribute to do victory of science over barriers of all kinds erected throughout the Balkans.

CONTENTS

MATHEMATICS, COMPUTER SCIENCE AND MECHANICS

PHYSICS

EPIPHYTIC LICHENS IN THE TOWN OF ZVEČAN AND THEIR BIOINDICATIOR S VALUE

GORDANA ALEKSIĆ[1],[★], SLAVIŠA STAMENKOVIĆ[2], SVETLANA RISTIĆ[2], MARIJA MARKOVIĆ[2]

[1]Faculty of Natural Sciences and Mathematics, University of Priština, Kosovska Mitrovica, Serbia
[2]Faculty of Sciences and Mathematics, University of Niš, Niš, Serbia

ABSTRACT

This paper treats the long-term changes in area of the "lichen desert" of town Zvečan. Comparison of results obtained in 1926, when 67 lichen species where present, through the results in 1983 and 1988 when the "lichen desert", low or no lichen diversity was established because of the air pollution, with investigations carried out in 2014, 16 lichen species were identified. The "lichen desert" is no existing any more. The main reason that the lichens are present now is termination of operation of the "Trepča" company and cessation primary pollutants emissions. Using lichens as a bio-indicators in this investigation it was established the average air pollution, which is lichen "struggle zone",meaning increase air quality.

Keywords: "Lichen desert", Lichen "struggle zone", Bio-indicators, Air quality, Zvečan

INTRODUCTION

Knowledge of lichens, the ecology of certain species and the legitimacy of their distribution in urban areas is important for science for theoretical and applicative aspect.

Data on the works of Androssovsky and Szatal (1926) are available about the lichen in the area of Kosovska Mitrovica (Kušan, 1953). Beqiri et al. (1983) have done the lichenological zone of the Kosovska Mitrovica region, while Murati et al. (1988) and his associates investigated the efect of polluted air on the lichens development in this area.

After these lichens investigations 26 years have passed. During this time, there have been changes in urban and industrial terms. Kosovska Mitrovica has developed into one of the larger cities in the region. In 1999, the base of development and source of extreme environmental pollution of the area of Kosovska Mitrovica (Živić et al., 2014; Živić, 2015), RMHK "Trepčca", stopped working. This has led to a number of social problems, but it has contributed to the improvement of the environment and the recovery of diferent ecosystems (Živić et al., 2008). The enormous emissions of pollutants have ceased, which have deteriorated the living conditions in all aspects (water, air, soil). However, with the termination of operation of the "Trepča", environmental pollutants were not stopped by the secondary pollutants (Babović-Jakšić & Živić, 2008). Deposits containing large quantities of slag produced as a product of lead, zinc, bismuth and other metals metallurgy, followed by trash ore left behind in the flotation of ore, as well as other types of industrial and urban waste, even today deteriorate the environment in Kosovska Mitrovica and Zvečan. However, secondary pollution from the deposits still represent the threat for the human population health (Babović-Jakšić & Živić, 2008; Babović-Jakšić et al., 2013) and for the whole ecosystem.

One of the ways to control the quality of the environment is the application of bio-indication methods. They are based on the selective response of certain species to specific environmental factors. Jakšić (2013) and Živić (2015) use diferent species of invertebrates to investigate the ecosystems under the influence of pollution. In this sense, the lichens have proven to be good bioindicators for assessing the quality of atmospheric air. This special practical application is able to be used in the assessment of air pollution in urban areas, especially on the increased concentration of SO_2 - the main urban pollutant.

Starting from the fact that the lichens in Zvečan is not well known, we have approached theme with the aim of concluding on the basis of the analysis of the diversity and distribution of epiphytic lichen and the air quality in Zvečan. One of the ways to control the quality of the environment is the application of bioindication methods. They are based on the selective response of certain species to specific environmental factors. In this sense, the lichens have proven to be good bio-indicators for assessing the quality of atmospheric air. This special practical application is able to be used in the assessment of air pollution in urban areas, especially on the increased concentration of SO_2 - the main urban pollutant. Lichens, show the actual state of air pollution at the place where they live, and in that way they point to a real, long-lasting process of negative impact on people and other living organisms of the given area (Stamenković, 2004).

Starting from the fact that the lichens in Zvečan is not well known, we have approached theme with the aim of concluding on the basis of the analysis of the diversity and distribution of epiphytic lichen and the air quality in Zvečan.

★ Corresponding author: gordanaalekszic@gmail.com

MATERIALS AND METHODS

Lichenological material was collected in April 2014. Collection, determination and mapping of epiphytic lichens was carried out in the yard of Elementary School "Vuk Karadžić" in Zvečan. The method used in these investigation is developed by Kirschbaum & Wirth (1997).

The lichens were observed and determined on six trees of the same woody species, on the surface of 50 x 20 cm which is divided into squares of 10 x 10 cm. This measuring surface is at a height of 1 m from the surface of the soil on the examined tree. The abundance was determined or each lichen species on all six studied trees.

The sum of the average abundances for all six trees, for each lichen species, is the local index of air quality IAP (Index of Atmospheric Purity). In order to obtain the final result from the obtained value, the frequency of the species *Lecanora conizaeoides* is taken away, if present on the measuring surface. The IAP is equal to the value obtained. The air quality index was calculated according to the ratio: the sum of frequency frequencies = IAP.

Based on the established diversity of lichens, mapping was performed using lichens as bio-indicators based on the general scale of air quality determination according to IAP values (Conti Cecchetti, 2001) (Table 1).

The identification of the lichen species was done using the keys: Dobson (2011); Wirth (1995), while Index Fungorum was used to determine the nomenclature. The following reagents were used to determine more closely: concentrated HCL, saturated aqueous solution of chlorine lime ($CaClO_2$), 10% solution of NaOH in water and alcoholic solution J + KJ.
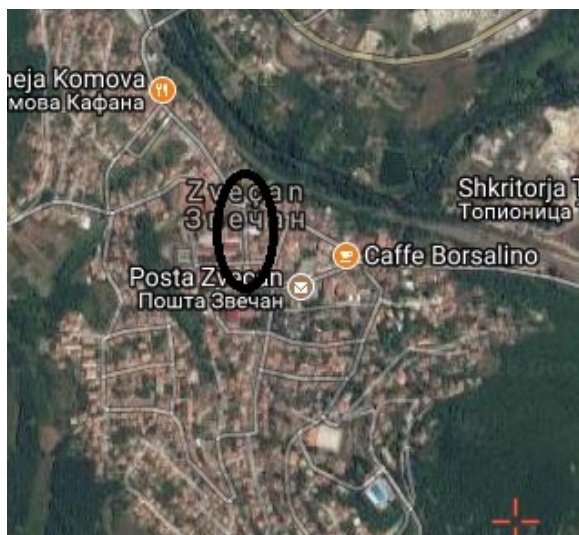
Figure 1. The position of the measuring point is indicated with an ellipse on the map of Zvečan

As a measuring point it was selected the park in the yard of the primary school "Vuk Karadzić" in Zvečan. Two woody species were selected for the substrate under which the investigation was carried out: *Aesculus hippocastanum* (L.) and Picea abies

(L.) Karsten. Measurement point coordinates are: 42.909818 N; 20.8384488E; Å = 578 m. The position of the measuring point is indicated with an ellipse on the map of Zvečan (Figure 1).

RESULTS AND DISCUSSION

Field analysis revealed the presence of 16 species of lichens from 11 genera.With crustose thallus type there are four, foliose 11 and a shrubby one lichen species (Table 2).

On the *Aesculus hippocastanum*, the presence of 11 lichen species was determinate. Present lichens species according to the gradient of decline: *Amandinea punctata* and *Physcia stellaris* (100%), *Hypogymnia physodes*, *Phaeophysia orbicularis*, *Physcia adscendens*, *Physconia grisea* (83,33%), *Physcia aipolia* (66,67), *Candelariella xanthostigma* and *Ramalina fraxinea* (50%), *Physcia tenella* and *Xanthoria parietina* (33.33%) (Table 3).
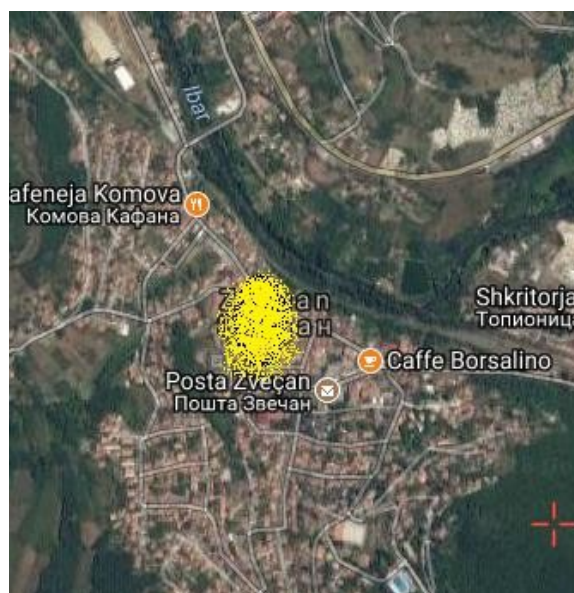
Figure 2. Mapping of the measuring point based on the general scale of air quality determination according to the IAP values (yellow color indicates the average air pollution, the lichen "struggle zone ")

On the *Picea abies* 10 lichens species have been identified. Present species of lichens according to the gradient of decline: *Caloplaca cerina, Melanelixia fuliginosa* subsp. *glabratula, Physcia adscendens, Physcia aipolia* and *Physcia tenella* (100%), *Physcia stelaris, Xanthoria parietina* and *Xanthoria polycarpa* (83,33%), *Caloplaca cerinella* (66.67%) and *Punctelia subrudecta* (50.00%) (Table 4).

Similarities are in the presence of the species *Physcia adscendens, Physcia aipolia, Physcia stellaris, Physcia tenella* and *Xanthoria parietia* on both substrates (Tables 3 and 4).

The diferences are that only at the *Aesculus hippocastanum* present species: *Amandinea punctata, Candelariella xanthostigma, Hypogymnia physodes, Phaeophyscia orbicularis,*

Table 1. General scale of air quality determination according to IAP values (Conti & Cecchetti, 2001)

Polution	Extreme high	Very high	High	Average	Weak	Very weak
Color						
IAP	0	12.5	25.0	37.5	50.0	
Lichens zone of indicators	"lichen desert"		" struggle zone"		"normal zone"	

Table 2. Identified lichen species and thallus type

Lichen species	Thallus type		
	crustose	foliose	fruticose (shrubby)
Amandinea punctat (Hoffm.) Massal.	+		
Caloplaca cerina (Ehrh. ex Hedw) Th. Fr.	+		
Caloplaca cerinella (Nyl.) Flagey	+		
Candelariella xanthostigma (Ach.) Lettau.	+		
Hypogymnia physodes (L.) Nyl.		+	
Melanelixia fuliginosa subsp. *glabratula* (Lamy) J.R. Laundon,		+	
Phaeophyscia orbicularis (Necker) Moberg		+	
Physcia adscendens (Fr.) H. Olivier.		+	
Physcia aipolia Ehrh. ex Humb.) Furnr.		+	
Physcia stellaris (L.) Nyl.		+	
Physcia tenella (Scop.) DC.		+	
Physconia grisea (Lam.) Poelt.		+	
Punctelia subrudecta (Nyl.) Krog.		+	
Ramalina fraxinea (L.) Ach.			+
Xanthoria parietina (L.) Th. Fr.		+	
Xanthoria polycarpa (Hoffm.) Rieber.		+	

Physconia grisea and *Ramalina fraxinea* while on the *Picea abies* are not present.

On the *Picea abies*, the presence of species was established: *Caloplaca cerina, Caloplaca cerinella, Melanelixia fuliginosa* subsp. *glabratula, Punctelia subrudecta* and *Xanthoria polycarpa*, while on the *Aesculus hippocastanum* are not present.

Comparing the lichen habitat on these two substrates, the lichens are present on the *Aesculus hippocastanum*, on the tree trunk, while on the *Picea abies* they are present only on the branches of the trees, but there are no exist on the trunk.

For the mapping of the measuring point using lichens as a bio-indicator, based on a general scale of air quality IAP values, following the used method, only diversity and lichen abundance on the *Aesculus hippocastanum* can be used. On the measuring surface required by the method, there are no lichens on the *Picea abies*, the diversity and the abundance are equal to zero (0). On this plant species, lichens are present only on the branches of the trees, not on the trunk. This is the reason for not taking the IAP value on *Picea abies* for mapping. Therefore, the mapping of the measuring point based on the IAP value on the *Aesculus hippocastanum* was used.

On the *Aesculus hippocastanum*, the IAP value is 34.67, indicating the average air pollution, which is the lichen "struggle zone" (Figure 2).

In 1926, Androssovsky and Szatala identified 18 families of lichens in the region Kosovska Mitrovica and Zvečan, classified in 24 genera and 67 species (Kušan, 1953). In 1983, Beqiri and associates performed the lichenological zone of the Kosovska Mitrovica. They noted in the "lichen desert" zone three species: *Lecanora erysibe, Calopa cadecipiens* and *Candelari vitelina*. This zone coincides with the site that was explored by this work.

In the second zone, the "zone of struggle" of the lichens, identified 10 taxa: *Xanthoria erysibe, Xanthoria parietina, Physcia ascendes, Lecanora muralis, Candelariella vitelina, Candelariella aurella, Lecidea sp., Caloplaca decipiens, Lecanora pallid, Lecanora subfusca*.

This zone coincides to a lesser extent with the research of this investigations, because it covers a wider zone with surrounding, more distant municipalities. In the third, "normal" zone, it was found that species from the family of Usnaceae appeared.

Species which were identified during previous investigations and now: *Xanthoria parietina*, and *Physcia adscendens*.

Comparing with earlier research by Murati with associates (1988), when the "lichen desert" was established, the lack of lichen

Table 3. Lichens diversity, abundance and frequency (%) on *Aesculus hippocastanum*

Lichen species	number of tree							%
	I	II	III	IV	V	VI	Average abundance	
Amandinea punctata	6	10	9	6	6	5	7,00	100
Candelariella xanthostigma	1	0	4	0	4	0	1,50	50
Hypogymnia physodes	1	0	4	5	5	2	2,83	83,33
Phaeophyscia orbicularis	10	0	3	8	8	5	5,63	83,33
Physcia adscendens	6	0	4	6	7	10	5,50	83,33
Physcia aipolia	7	0	0	3	3	1	2,33	66,67
Physcia stellaris	10	1	5	9	9	5	6,50	100
Physcia tenella	1	0	1	0	0	0	0,33	33,33
Physconia grisea	1	0	3	2	2	2	1,67	83,33
Ramalina fraxinea	0	0	2	1	1	0	0,67	33,33
Xanthoria parietina	0	0	1	0	0	3	0,67	50
Lecanora conizaeoides							0	
Index of Atmospheric Purity (sum of frequencies)							$\sum 34,67$	

Table 4. Lichens diversity, abundance and frequency (%) on *Picea abies*

Lichen species	number of tree							%
	I	II	III	IV	V	VI	Average abundance	
Caloplaca cerina	7	8	5	8	6	4	6,33	100
Caloplaca cerinella	0	1	0	1	1	2	0.83	66,67
Melanelixia fuliginosa subsp. *glabratula*	3	4	5	5	6	5	4.67	100
Physcia adscendens	10	10	9	9	10	10	9.67	100
Physcia aipolia	3	5	5	7	6	2	4.67	100
Physcia stellaris	1	1	0	1	2	2	1.16	83,33
Physcia tenella	6	4	5	8	6	9	6,33	100
Punctelia subrudecta	0	0	2	1	1	0	0,67	50
Xanthoria parietina	2	1	3	0	4	2	2.00	83,33
Punctelia subrudecta	0	1	3	1	4	2	1.83	83,33
Index of Atmospheric Purity (sum of frequencies)							$\sum 38,16$	

diversity, this investigation identified 16 species at this site. This indicates an increase in diversity, or improvement of habitats.

The reason for this is the termination of "Trepča" company and no primary emissions of pollutants.

CONCLUSION

Biomonitoring was carried out in the Park site in the yard of primary school "Vuk Karadžić" in Zvečan, April 2014. Two woody species were selected for the substrate under which it was applied: *Aesculus hippocastanum* and *Picea abies*. Analyzing the investigated samples, 16 species were identified within 11 genera.

The most common genera are: Physcia, four species (*P. stellaris, P. adscendens, P. tenella, P. aipolia*), *Caloplaca*, two species (*C. cerina and C. cerinella*), *Xanthoria* two species (*X. parietina and X. polycarpa*). Other genera are present with one species. Lichens are present on the *Aesculus hippocastanum* on the tree trunk, while on the *Picea abies* are present only on the branches

of trees, but there are not on the trunk. On the *Aesculus hippocastanum*, the IAP value is 34.67, indicating an average air pollution.

Mapping of the measuring point was performed based on the IAP value of the *Aesculus hippocastanum*.

Using the *Picea abies* as a substrat, value of the IAP is 38.16. After the "lichen desert" in the year of 1988. in 2014. it was established lichen "struggle zone".

REFERENCES

Babović-Jakšić, T., Živić, V. N., Stamenković, S., Đikić, A., & Sretić, L. 2013. The heavy metal influence on the human population in Kosovska Mitrovica. In V International Symposium of Ecologists of Montenegro – The Book of Abstracts and Programme. p. 99.

Babović-Jakšić, T. & Živić, V. N. 2008. Types of Ekological Projects Implemented by L/NGs in Kosovska Mitrovica from 1999-2008. Natura Montenegrina, 7(3), pp. 125-128. Podgorica, Montenegro.

Babović-Jakšić, T. & Živić, V. N. 2008. Female Population in Reproductive Period Awareness Presence and Harmful Influence of Lead in Kosovska Mitrovica. Natura Montenegrina, Podgorica, 7(3), pp. 503-508.

Beqiri, S., Bejtullahu, B., & Miletic, S. 1983. Ispitivanje zagađenosti vazduha Titove Mitrovice i okoline tokom 1982/83. god. In Simpozijum o stanju, zaštiti i unapređenju čovekove sredine. Zvečan. pp. 153-164.

Conti, M. E. & Cecchetti, G. 2001. Biological monitoring: lichens as bioindicators of air pollution assessment — a review. Environmental Pollution, 114(3), pp. 471-492. doi:10.1016/s0269-7491(00)00224-4.

Dobson, F. 2011. Lichens An Illustrated Guide to the British and Irish Species.England: The Richmond Publishing Co. Ltd.

Jakšić, T. 2013. Soil bioindication in the region of Kosovska Mitrovica. PhD degree. University of Pristina, Faculty of Sciences and Mathematics, Kosovska Mitrovica.

Kirschbaum, U. & Wirth, V. 1997. Les lichens bio-indicators. Paris: Edition Ulmer.

Kušan, F. 1953. Prodromus flore lišaja Jugoslavije.Zagreb: JAZU.

Murati, M., Pejčinović, D., & Hodža, E. 1988. Uticaj onečišćenog vazduha na razvoj lišajeva u području Titove Mitrovice. In Četvrti kongres ekologa Jugoslavije. Ohrid.

Stamenković, S. 2004. Bioindikacija stepena žagađenosti vazduha urbanih sredina korišćenjem lišaja kao bioindikatora – seminar. In .Univerzitet u Beogradu - Biološki fakultet - Institut za botaniku.Botanička bašta „Jevremovac". pp. 3-5.

Wirth, V. 1995. Die Flechten Baden-Wurttembergs-Teil 1 and 2. Stuttgart: Vergal Ulmer.

Živić, V. N. 2015. Characteristics of macro fauna invertebrates with an overview of the Oligochaete fauna in ecosystems under the influence of the thermal complex "Obilić" thermal power plant. University of Prishtina with dislocated in Kosovska Mitrovica - Faculty of Natural Sciences and Mathematics, pp. 1-155.

Živić, V. N., Atanacković, A., Milosević, S., & Milosavljević, M. 2014. The distribution of Astacidae (Decapoda) fauna in Kosovo and Metohija. Water Research and Management, 4(4), pp. 35-40.

Živić, V. N., Vukanić, V., Babović-Jakšić, T., & Miljanović, B. 2008. Distribution of macrozoobenthos in the tribuataries of river Ibar in the Northern part of Kosovo and Metohija. Natura Montenegrina, 7(2), pp. 401-411. Podgorica, Republic of Montenegro.

THE VENTRAL CRANIAL SIZE AND SHAPE VARIATION BETWEEN MALES AND FEMALES OF EUROPEAN BROWN FROGS: *RANA DALMATINA*, *R. GRAECA* AND *R. TEMPORARIA* (ANURA, AMPHIBIA)

JELENA KRSTIČIĆ RAČKOVIĆ [1*], NATAŠA TOMAŠEVIĆ KOLAROV [2], TANJA VUKOV [2]

[1]Faculty of Science and Mathematics, University of Priština, Kosovska Mitrovica, Serbia
[2]Institute for Biological Research „Siniša Stanković", University of Belgrade, Serbia

ABSTRACT

Sexual size and shape dimorphism is a very common phenomenon widely studied in the field of evolutionary biology. The differences between sexes are related to their life strategies and driven by the two evolutionary processes, sexual and natural selection. In amphibians, females are larger sex due to high correlation with fecundity, while dimorphism in body shape is often related to intrasexual competition for opposite sex during the breeding season. The main aim of this study is to describe patterns of ventral cranial size and shape variation between males and females of three species of European brown frogs, *Rana dalmatina, R. graeca, R. temporaria*, from the Balkan Peninsula. Our results showed that species *R. dalmatina* and *R. graeca* are sexually dimorphic for the ventral cranial size while species *R. graeca* and *R. temporaria* for the ventral cranial shape. Sexual dimorphism in cranial size is most probably an indirect consequence of natural selection favoring larger body for higher fecundity in explosive breeders like brown frogs. Cranial shape variation is under a strong influence of size variation but without allometric scaling between sexes. Sexual shape differences of analyzed brown frog species were most pronounced in the level of connection between cranium and jaw which indicate that differential diet of males and females can be a factor affecting observed sexual dimorphism patterns. More detailed studies of males and females microhabitats are necessary to conclude if differences in intersexual ecology affect intersexual size and shape differences in the cranium.

Keywords: Cranium, Sexual dimorphism, Geometric morphometrics.

INTRODUCTION

Size and shape variations are the principal sources of biological diversity (Hallgrímsson & Hall, 2005) and their origin and maintenance are in the focus of many biological disciplines. Sexual size and shape dimorphism, the morphological difference between sexually mature males and females, is a very common phenomenon widely studied in the field of evolutionary biology (Fairbairn, 2013). The differences between sexes are related to their life strategies and driven by the two evolutionary processes, sexual and natural selection (Shine, 1989; Monnet & Cherry, 2002).

Sexual dimorphism in size (*sexual size dimorphism,* SSD) is the most prominent and most obvious aspect of sexual dimorphism (Shine, 1989; Fairbairn, 1997; Fairbairn et al., 2007). SSD is the topic of a large number of studies for a long time (e.g. Snyder et al., 1976, Shine, 1979; Price, 1984; Cox & Calsbeek, 2010; McPherson & Chenoweth, 2012; Plavcan, 2012; Friedman & Remeš, 2016; Cooper, 2018; Ng et al., 2019), while sexual shape dimorphism (*sexual shape dimorphism,* SShD) is more extensively explored in the last two decades (e.g. Herrel et al., 1999; Bonduriansky, 2006; Berns, 2013; Vladić et al., 2019).

Amphibians are an appropriate group for the sexual dimorphism studies as the difference between males and females is evident for number of morphological features such as body size and shape and body coloration (Monnet & Cherry, 2002; Hoffman & Blouin, 2000; Bell & Zamudio, 2012; Zhang & Lu, 2013; Petrović et al., 2017; Vukov et al., 2018). For example, females are larger sex in 90% of anuran species as the larger body is correlated with higher fecundity (Shine, 1979). Dimorphism in body shape is often related to intrasexual competition through contests for dominance or attracting the opposite sex during the breeding season (Shine, 1979).

Even though the sexual dimorphism of the skull is widely studied in animal groups such as mammals (Gittleman & Valkenburgh, 1997; Morris & Carrier, 2016; Porobić et al., 2016) and lizards (Kuo et al., 2009; Ljubisavljević et al., 2010; Borczyk et al., 2014), it is understudied in amphibians (Ivanović et al., 2007; Ivanović et al., 2008; Ivanović & Kalezić, 2012), especially in anurans (but see Vukov et al., 2018; Krstičić Račković et al., 2019). Therefore, the aim of this study is to describe patterns of ventral cranial size and shape variation between males and females of three species of European brown frogs: *Rana temporaria, R. dalmatina* that are widely distributed throughout Europe (Sillero et al., 2014), and *R. graeca*, species endemic in the Balkan Peninsula (Džukić & Kalezić, 2004).

---

* Corresponding author: jelena.krsticic@pr.ac.rs
BIOLOGY

MATERIAL AND METHODS

In this study, we included 112 adult skulls (*R. dalmatina*: 20 males, 19 females; *R. graeca*: 19 males, 17 females; *R. temporaria*: 27 males, 10 females) obtained from the Batrachological Collections of the Institute for Biological Research "Siniša Stanković," Belgrade (Džukić et al., 2015). The sample size in this geometric morphometric study was large enough for the appropriate estimation of different parameters (Cardini & Elton, 2007).

Skulls were taken from adult specimens (determined by gonad examination) and they were cleared with trypsin and potassium hydroxide (KOH), stained with Alizarin Red S to distinguish cranial elements and their articulations better and then preserved in glycerol. Images of the ventral cranium were obtained with a Sony DSC-F828 digital camera (resolution 8.0 MP; Sony Corp., Tokyo, Japan). Eighteen specific two-dimensional landmarks for the ventral cranium were digitized using TpsDig2 software (Rohlf, 2008). The chosen configuration of landmarks provides an adequate summary of specific aspects of the ventral cranium morphology. The specific positions of the chosen landmarks are shown in Figure 1.
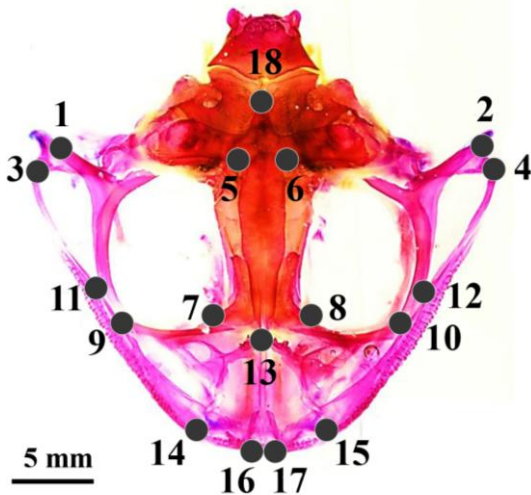
Figure 1. Location of the selected landmarks on the ventral cranium of a brown frog (*R. temporaria*). 1,2 Tip of lateral pterygoid process (towards the quadrate); 3,4 Most lateral point of quadrate; 5,6 Suture between parietal and prootic; 7,8 Lateralmost point of sphenethmoid (anterior); 9, 10 Lateralmost point of palatine (towards the maxilla); 11,12 Contact point between maxilla and anterior pterygoid process; 13 Anteriormost point of sphenethmoid; 14, 15 Anteriormost point of maxilla; 16, 17 Anteriormost point of premaxilla; 18 Posteriormost point of parasphenoid.

We applied Generalized Procrustes analysis (GPA) (Dryden & Mardia, 1998) to analyse interspecific, sexual, and body size-related variation in the ventral cranium of brown frogs'. A GPA was used to obtain a matrix of shape co-ordinates from which differences due to the position, scale, and orientation were removed (Dryden & Mardia, 1998). Variation in ventral cranial

size (centroid size - CS) was evaluated by ANOVA with sex as factors. Determining the level of sexual dimorphism in size, the standard index is calculated by CS values: I_{SSD} = size of the larger sex (females)/size of the smaller sex (males). The differences in shape between sexes are described as Procrustes distances. Procrustes distance, a linear measure of shape differences between landmark configurations, was used as an index of sexual dimorphism in shape (I_{SShD}).

To access the optimal estimate of the impact of allometry on shape changes, we employed two-way permutational MANCOVA with species and sex as factors and CS as covariable. Factor × CS interaction would indicate that size-dependent shape changes differ between the species or sexes. The percentage of predicted allometry with the statistical significance of the allometric regressions was tested with permutation tests against the null hypothesis of allometry independence. Residuals from the multivariate regression of shape variables on CS were used to visualize non-allometric shape changes in the ventral cranium between sexes by discriminant analysis, and to calculate size corrected index of sexual dimorphism in shape ($I_{SShDcorr.}$).

Analyses were performed in MorphoJ (Klingenberg, 2011), Statistica (StatSoft Inc., 2011), and in R 3.2.0 (R Core Team, 2015).

RESULTS

Cranial size differs significantly between sexes for *R. dalmatina* and *R. graeca* with larger cranium in females, but not for *R. temporaria* (Table 1). Females had larger body size in our sample (*R. dalmatina*: females L = 63.9 mm, males L = 57.2 mm; *R. graeca*: females L = 68.1 mm, males L = 61.9 mm; *R. temporaria*: females L = 85.1 mm, males L = 75.7). The calculated SSD indexes (Table 1) and mean CS values for *R. dalmatina* and *R. graeca* showed that females had 12% larger cranium than males.

Table 1. Means and standard deviations (SD) of cranial size (CS) for males (m) and females (f), and index of sexual size dimorphism (I_{SSD}). Statistically significant values in bold.

species		CS means	CS SD	I_{SSD}	P
R. dalmatina	m	33.47	2.73	1.13	**0.003**
	f	37.72	5.06		
R. graeca	m	45.71	3.95	1.13	**0.010**
	f	48.06	5.33		
R. temporaria	m	39.07	4.54	1.05	0.156
	f	44.01	5.48		

Regression analyses showed that the ventral cranium of males and females for all three analysed brown frog species share the same allometric trajectory (F = 0.6744, P = 0.6438), with 16.91% of shape variation explained by the size variation (P

< 0.0001). Sexual shape differences were significant for *R. graeca* and *R. temporaria*, and not significant for *R. dalmatina*, before and after removing the allometric component of the ventral cranium variation (Table 2). The calculated SShD indexes were similar for *R. graeca* and *R. temporaria* (Table 2).

Table 2. Indices of sexual size dimorphism before (I_{SShD}) and after removing allometric component of variation ($I_{SShDcorr.}$). Statistically significant values in bold.

species	I_{SShD}	P	$I_{SShDcorr.}$	P
R. dalmatina	0.02	0.060	0.01	0.292
R. graeca	0.03	**0.001**	0.02	**0.048**
R. temporaria	0.03	**0.001**	0.03	**0.001**

Patterns of the intersexual shape variation were the same before and after removing the allometric component. Females of the *R. graeca* had wider skull than males in the posterior part of the cranium (landmarks 1, 2, 3, 4) but shorter snout (landmarks 14, 15, 16, 17), with anteriorly displaced contact between pterygoid and maxilla (landmarks 11, 12) (Figure 2A). In the *R. temporaria* females compared to males the tips of lateral pterygoid process and quadrate bones were displaced posteriorly (landmarks 1, 2, 3, 4), contacts between the palatine and maxilla and pterygoid and maxilla anteriorly (landmarks 9, 10, 11, 12), and snout was slightly longer (landmarks 16, 17) (Figure 2B).
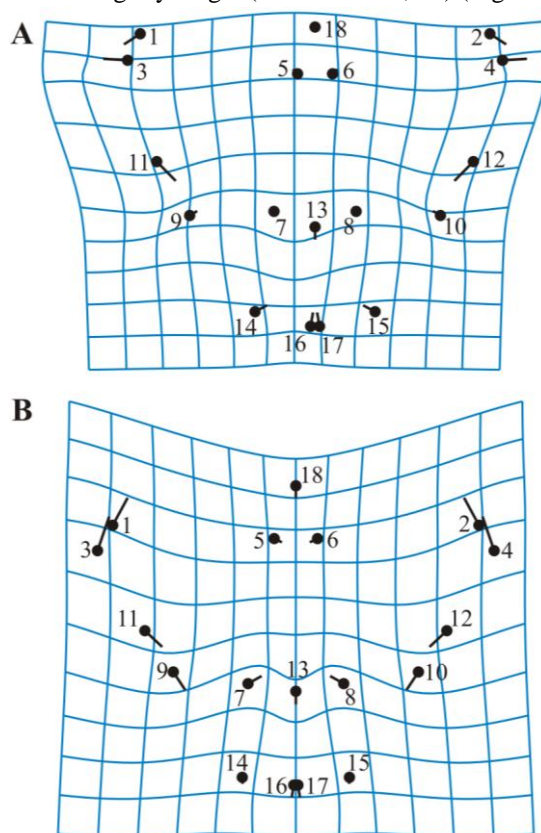
Figure 2. Shape changes associated with non-allometric SShD between sexes in *R. graeca* (A) and *R. temporaria* (B) (from males to females).

DISCUSSION

Three species of the European brown frogs are sexually dimorphic for the ventral cranial size in *R. dalmatina* and *R. graeca* and for the ventral cranial shape in *R. graeca* and *R. temporaria*. Cranial shape variation is under a strong influence of size variation but without allometric scaling between sexes. The most pronounced shape dissimilarities between sexes are found in the posterior part of the ventral cranium.

Two evolutionary processes, sexual and natural selection, have the highest impact on the morphological variability of males and females (Shine, 1989; Andersson, 1994; Fairbairn, 1997; Hendry et al., 2014). Therefore, the difference between sexes is a consequence of differential interaction of each sex with environment and interaction between sexes (Herrel et al., 2001; Sacchi et al., 2009; Peiman & Robinson, 2010; Lailvaux et al., 2012). In the context of sexual selection, sexually dimorphic size and shape of the cranium could evolve through intrasexual competition where cranial traits provide advantages in breeding opportunities to some individuals through contests of dominance or attracting the opposite sex. For example, maximum bite force linked to features of cranial-jaw complex contributes to successful breeding in reptiles (Lappin & Husak, 2005; McBrayer & Anderson, 2007). In addition, sexually dimorphic size and shape of the cranium could arise through natural selection and intersexual niche divergence in order to reduce intersexual competition for resources and habitat use. Indeed, many studies showed that skull dimorphism is mainly restricted to differences in the size and shape of the parts that can affect bite force and prey size (Vincent, et al., 2004; Herrel et al., 2007; Kaliontzopoulou et al., 2007; Ljubisavljević et al., 2010).

Our results showed that females had larger ventral cranium and bodies than males, therefore sexual dimorphism in cranial size is most probably an indirect consequence of natural selection favoring larger body for higher fecundity in explosive breeders like brown frogs (Woolbright, 1983). In addition, brown frogs do not display male to male combats or territorial contests, or intersexual interactions like copulatory bites, so sexual dimorphism in cranial size is probably not a consequence of sexual selection. Sexual shape differences of analyzed brown frog species were most pronounced in the level of connection between cranium and jaw which indicate that differential diet of males and females can be a factor affecting observed sexual dimorphism patterns. However, studies about the diet of brown frogs males and females are almost not existing (Cicort-Lucaciu et al., 2011) so the direct link between observed intersexual cranial shape variation and diet variation cannot be established. Study of the dorsal cranium variation in the European brown species showed that ecologically similar species (in habitat characteristics and type of locomotion) shared the cranial morphology (Krstičić Racković et al., 2019). However, more detailed studies of males and females microhabitats are necessary

to conclude if differences in intersexual ecology affect intersexual size and shape differences in the cranium.

Observed patterns of sexual dimorphism in cranial size and shape of three brown frog species indicate that further studies are necessary in order to find causes and consequences of intersexual variation of the cranium.

REFERENCES

Andersson, M. B. 1994. Sexual selection. Princeton, New Jersey: Princeton University Press.

Bell, R. C., & Zamudio, K. R. 2012. Sexual dichromatism in frogs: natural selection, sexual selection and unexpected diversity. Proceedings of the Royal Society B: Biological Sciences, 279, pp. 4687-4693. doi: 10.1098/rspb.2012.1609

Berns, C. M. 2013. The evolution of sexual dimorphism: understanding mechanisms of sexual shape differences, Sexual Dimorphism, IntechOpen doi:10.5772/55154

Bonduriansky, R. 2006. Convergent evolution of sexual shape dimorphism in Diptera. Journal of Morphology, 267(5), pp. 602-611. doi:10.1002/jmor.10426

Borczyk, B., Kusznierz, J., Paśko, Ł., & Turniak, E. 2014. Scaling of the sexual size and shape skull dimorphism in the sand lizard (Lacerta agilis L.). Vertebrate Zoology, 64(2), pp. 221-227.

Cardini, A., & Elton, S. 2007. Sample size and sampling error in geometric morphometric studies of size and shape. Zoomorphology, 126(2), pp. 121-134. doi:10.1007/s00435-007-0036-2

Cicort-Lucaciu, A. S., Sas, I, Roxin, M., Badar, L., & Goilean, C. 2011. The feeding study of a Rana dalmatina population from Carei Plain, South Western Horticulture. Biology and Environment, 2(1), pp. 35-46.

Cooper, M. I. 2018. Sexual size dimorphism and the rejection of Rensch's rule in Diplopoda (Arthropoda). Journal of Entomology and Zoology Studies, 6(1v), pp. 1582-1587. doi:10.22271/j.ento.2018.v6.i1v.07

Cox, R. M., & Calsbeek, R. 2010. Sex-specific selection and intraspecific variation in sexual size dimorphism. Evolution: International Journal of Organic Evolution, 64(3), pp. 798-809. doi: 10.1111/j.1558-5646.2009.00851.x

Dryden, I. L., & Mardia, K.V. 1998. Statistical analysis of shape. New York: John Wiley and Sons.

Džukić, G., & Kalezić, M. L. 2004. The biodiversity of amphibians and reptiles in the Balkan Peninsula. In H.I. Griffiths, B. Kryštufek, & J.M. Reed Eds., Balkan biodiversity: Pattern and process in the European hotspot.Dordrecht: Springer Nature. pp. 167-192; doi: 10.1007/978-1-4020-2854-0_10

Džukić, G., Cvijanović, M., Urošević, A., Vukov, T. D., Tomašević Kolarov, N., Slijepčević, M., Ivanović, A., & Kalezić, M. L. 2015. The batrachological collections of the Institute for biological research "Siniša Stanković", University of Belgrade. Bulletin of the Natural History Museum in Belgrade, 8, pp. 118-167. doi:10.5937/bnhmb1508118D

Fairbairn, D. J. 1997. Allometry for sexual size dimorphism: Pattern and Process in the Coevolution of Body Size in Males and Females. Annual Review of Ecology and Systematics, 28(1), pp. 659-687. doi:10.1146/annurev.ecolsys.28.1.659

Fairbairn, D. J. 2013. Odd Couples: Extraordinary differences between the sexes in the animal kingdom. Princeton: Walter de Gruyter GmbH. doi:10.1515/9781400847600

Fairbairn, D. J., Blanckenhorn, W.U., Székely, T., & Eds., 2007. Sex, size and gender roles: Evolutionary studies of sexual size dimorphism. Oxford: Oxford University Press. doi: 10.1093/acprof: oso/9780199208784.001.0001

Friedman, N. R., & Remeš, V. 2016. Global geographic patterns of sexual size dimorphism in birds,port for a latitudinal trend. Ecography, 39(1), pp. 17-25. sup; doi: 10.1111/ecog.01531

Gittleman, J. L., & Van, V. B. 1997. Sexual dimorphism in the canines and skulls of carnivores: effects of size, phylogency, and behavioural ecology. Journal of Zoology, 242(1), pp. 97-117. doi: 10.1111/j.1469-7998.1997.tb02932.x

Hallgrímsson, B., & Hall, B. K. 2005. Variation and variability: Central concepts in biology. In B. Hallgrímsson & B. K. Hall Eds., Variation. Burlington, MA, USA: Elsevier. pp. 1-7; doi: 10.1016/B978-012088777-4/50003-X

Hendry, C. R., Guiher, T. J., & Pyron, R. A. 2014. Ecological divergence and sexual selection drive sexual size dimorphism in new world pitvipers (Serpentes: Viperidae). Journal of evolutionary biology, 27(4), pp. 760-771. doi: 10.1111/jeb.12349

Herrel, A., Damme, R. V., Vanhooydonck, B., & Vree, F. D. 2001. The implications of bite performance for diet in two species of lacertid lizards. Canadian Journal of Zoology, 79, pp. 662-670. doi: 10.1139/z01-031

Herrel, A., Mcbrayer, L., & Larson, P. 2007. Functional basis for sexual differences in bite force in the lizard Anolis carolinensis. Biological Journal of the Linnean Society, 91, pp. 111-119. doi: 10.1111/j.1095-8312.2007.00772.x

Herrel, A., Spithoven, L., van Damme, R., & Vree, F. D. 1999. Sexual dimorphism of head size in Gallotia galloti: testing the niche divergence hypothesis by functional analyses. Functional Ecology, 13(3), pp. 289-297. doi: 10.1046/j.1365-2435.1999.00305.x

Hoffman, E. A., & Blouin, M. S. 2000. A review of colour and pattern polymorphisms in anurans. Biological Journal of the Linnean Society, 70(4), pp. 633-665. doi: 10.1111/j.1095-8312.2000.tb00221.x

Ivanović, A., & Kalezić, M. L. 2012. Sexual dimorphism in the skull geometry of newt species of Ichthyosaura, Triturus and Lissotriton (Salamandridae, Caudata Amphibia). Zoomorphology, 131(1), pp. 69-78. doi: 10.1007/s00435-011-0143-y

Ivanović, A., Sotiropoulos, K., Furtula, M., Džukić, G., & Kalezić, M. L. 2008. Sexual size and shape evolution in European newts (Amphibia: Caudata: Salamandridae) on the Balkan Peninsula. Journal of Zoological Systematics and

Evolutionary Research, 46(4), pp. 381-387. doi: 10.1111/j.1439-0469.2008.00479.x

Ivanović, A., Vukov, T. D., Džukić, G., Tomašević, N., & Kalezić, M. L. 2007. Ontogeny of skull size and shape changes within a framework of biphasic lifestyle: a case study in six Triturus species (Amphibia, Salamandridae). Zoomorphology, 126(3), pp. 173-183. doi: 10.1007/s00435-007-0037-1

Kaliontzopoulou, A., Carretero, M. A., & Llorente, G. A. 2007. Multivariate and geometric morphometrics in the analysis of sexual dimorphism variation in Podarcis lizards. Journal of Morphology, 268, pp. 152-165. doi: 10.1002/jmor.10494

Klingenberg, C. P. 2010. MorphoJ: an integrated software package for geometric morphometrics. Molecular Ecology Resources, 11(2), pp. 353-357. doi:10.1111/j.1755-0998.2010.02924.x

Krstičić, R. J., Tomašević, K. N. T., Labus, N., & Vukov, T. 2019. Interspecific size-and sex-related variation in the cranium of European brown frogs (Genus Rana). Zoomorphology, 138(2), pp 277–286. doi: 10.1007/s00435-019-00441-9

Kuo, C. Y., Lin, Y. T., & Lin, Y. S. 2009. Sexual size and shape dimorphism in an Agamid lizard, Japalura swinhonis (Squamata: Lacertilia: Agamidae). Zoological Studies, 48(3), pp. 351-361.

Lailvaux, S. P., Huyghe, K., & Van, D. R. 2012. 'Why can't we all just get along?, Interspecific aggression in resident and non-resident Podarcis melisellensis lizards'. Journal of Zoology, 288(3), pp. 207-213. doi: 10.1111/j.1469-7998.2012.00943.x

Lappin, A. K., & Husak, J. F. 2005. Weapon performance, not size, determines mating success and potential reproductive output in the collared lizard (Crotaphytus collaris). The American Naturalist, 166(3), pp. 426-436. doi: 10.1086/432564

Ljubisavljević, K., Urošević, A., Aleksić, I., & Ivanović, A. 2010. Sexual dimorphism of skull shape in a lacertid lizard species (Podarcis spp. Dalmatolacerta sp. Dinarolacerta sp.) revealed by geometric morphometrics. Zoology, 113(3), pp. 168-174. doi: 10.1016/j.zool.2009.09.003

Mcbrayer, L. D., & Anderson, R. A. 2007. Sexual size dimorphisms and bite force in the northern alligator lizard, Elgaria coerulea. Journal of Herpetology, 41(4), pp. 554-560. doi: 10.1670/07-045.1

Mcpherson, F. J., & Chenoweth, P. J. 2012. Mammalian sexual dimorphism. Animal reproduction science, 131(3-4), pp. 109-122. doi: 10.1016/j.anireprosci.2012.02.007

Monnet, J. M., & Cherry, M. I. 2002. 'Sexual size dimorphism in anurans', Proceedings of the Royal Society of London. Series B: Biological Sciences, 269(1507), pp. 2301-2307. doi: 10.1098/rspb.2002.2170

Morris, J. S., & Carrier, D. R. 2016. Sexual selection on skeletal shape in Carnivora. Evolution, 70(4), pp. 767-780. doi: 10.1111/evo.12904

Ng, T. P., Rolán-Alvarez, E., Dahlén, S. S., Davies, M. S., Estévez, D., Stafford, R., & Williams, G. A. 2019. The causal relationship between sexual selection and sexual size dimorphism in marine gastropods. Animal Behaviour, 148, pp. 53-62. doi: 10.1016/j.anbehav.2018.12.005

Peiman, K., & Robinson, B. 2010. Ecology and evolution of resource-related heterospecific aggression. The Quarterly Review of Biology, 85(2), pp. 133-158. doi: 10.1086/652374

Petrović, T. G., Vukov, T. D., & Kolarov, N. T. 2017. Sexual dimorphism in size and shape of traits related to locomotion in nine anuran species from Serbia and Montenegro. Folia Zoologica, 66(1), pp. 11-22. doi: 10.25225/fozo.v66.i1.a4.2017

Plavcan, J. M. 2012. Sexual Size Dimorphism, Canine Dimorphism, and Male-Male Competition in Primates. Human Nature, 23(1), pp. 45-67. doi:10.1007/s12110-012-9130-3

Porobić, J., Ćirović, D., & Jojić, V. 2016. Cranial variability of the Serbian golden jackal: Geographic variation, sexual dimorphism and allometry. Zoologischer Anzeiger-A Journal of Comparative Zoology, 261, pp. 38-47. doi: 10.1016/j.jcz.2016.03.004

Price, T. D. 1984. The Evolution of Sexual Size Dimorphism in Darwin's Finches. The American Naturalist, 123(4), pp. 500-518. doi:10.1086/284219

R Core Team 2015. R: a language and environment for statistical computing, Version 3.2.0, R Foundation for Statistical Computing, Vienna, http://cran.R-project.org

Rohlf, F. J. 2008. TpsDig. In Ecology and Evolution. SUNY at Stony Brook. Version 2.12.

Sacchi, R., Pupin, F., Gentilli, A., Rubolini, D., Scali, S., Fasola, M., & Galeotti, P. 2009. Male-male combats in a polymorphic lizard: Residency and size, but not color, affect fighting rules and contest outcome, Aggressive Behavior. Official Journal of the International Society for Research on Aggression, 35(3), pp. 274-283. doi: 10.1002/ab.20305

Shine, R. 1979. Sexual Selection and Sexual Dimorphism in the Amphibia. Copeia, 1979(2), p. 297. doi:10.2307/1443418

Shine, R. 1989. Ecological Causes for the Evolution of Sexual Dimorphism: A Review of the Evidence. The Quarterly Review of Biology, 64(4), pp. 419-461. doi:10.1086/416458

Sillero, N., Campos, J., Bonardi, A., Corti, C., Creemers, R., Crochet, P. A., Crnobrnja Isailović, J., Denoël, M., Ficetola, G. F., Gonçalves, J., Kuzmin, S., Lymberakis, P., de Pous, P., Rodríguez, A., Sindaco, R., Speybroeck, J., Toxopeus, B., Vieites, D. R., Vences, M. 2014. Updated distribution and biogeography of amphibians and reptiles of Europe. Amphibia-Reptilia, 35(1), pp. 1-31. doi:10.1163/15685381-00002935

Snyder, N. F., & Wiley, J. W. 1976. Sexual size dimorphism in hawks and owls of North America. Ornithological Monograph. Washington DC: American Ornithologists' Union. no. 20; doi: 10.2307/40166710

-StatSoft, Inc. 2011. Statistica (data analysis software system). version 10, www.statsoft.com

Vincent, S.E., Herrel, A., & Irschick, D.J. 2004. Sexual dimorphism in head shape and diet in the cottonmouth snake (Agkistrodon piscivorus). Journal of Zoology, 264(1), pp. 53-59. doi: 10.1017/S0952836904005503

Vladić, Ž. J., Benítez, H. A., Pirnat, A., Hristovski, S., & Jelaska, L. Š. 2019. Variations in body shape of mountain habitat specialist Carabus croaticus and its sister species Carabus caelatus (Coleoptera: Carabidae) populations across Dinaric

Alps. Zoomorphology, 138(1), pp. 85-96. doi: 10.1007/s00435-018-0428-5

Vukov, T., Krstičić, J., Petrović, T., & Tomašević, K. N. 2018. Patterns of cranial sexual dimorphism in the yellow-bellied toad (Bombina variegata, Bombinatoridae). North-Western Journal of Zoology, 14(1), pp. 44-49.

Woolbright, L. L. 1983. Sexual Selection and Size Dimorphism in Anuran Amphibia. The American Naturalist, 121(1), pp. 110-119. doi:10.1086/284042

Zhang, L., & Lu, X. 2013. Sexual size dimorphism in anurans: ontogenetic determination revealed by an across-species comparison. Evolutionary Biology, 40(1), pp. 84-91. doi: 10.1007/s11692-012-9187-2

SYNTHESIS OF BIODEGRADABLE POLYESTER BASED ON RENEWABLE RESOURCES

VOJISLAV JOVANOVIĆ[1*], IVAN RISTIĆ[2], ALEKSANDRA MILETIĆ[2], SUZANA CAKIĆ[3], JELENA TANASIĆ[2], JAROSLAVA BUDINSKI-SIMENDIĆ[2]

[1]Faculty of Natural Science and Mathematics, University of Priština, Kosovska Mitrovica, Serbia
[2]Faculty of Technology, University of Novi Sad, Serbia
[2]Faculty of Technology, University of Niš, Serbia

ABSTRACT

Due to the growing problem caused by waste plastics, academia and industry, invest great dials of efforts to solve this problem and enable the sustainability of polymeric materials. One way, which can successfully solve this problem, is certainly the synthesis of new polymeric materials based on renewable raw materials. Therefore, in this paper, synthesis of polyester based on ricinoleic acid (as well as the methyl ester of ricinoleic acid) is presented, in order to obtain the polyol of the desired molar masses. The polymerization of the ricinoleic acid was performed in the presence of diethylene glycol, as an initiator, and titanium isopropoxide, as a catalyst. By analyzing the molar masses of the obtained polyesters, it has been confirmed that the control of the molecular weight of the polyricinoleic acid can be successfully accomplished by the addition of a precisely determined amount of diethylene glycol, thus enabling in this way the synthesis of polyols of desired properties. The molecular structure of the synthesized polyols is confirmed by FTIR and NMR spectroscopy. The analysis of the thermal properties showed that the glass transition temperatures of the synthesized polyols range from -70 to -80ºC, which makes it possible to apply these materials in low-temperature applications. The slight increasment of thermal stability is observed, only with the increasment of molecular weight, which was confirmed by TG analysis. The viscosity measurement results confirmed that as the molar weight of synthesized polyester increases, the viscosity of the samples also increases.

Keywords: Biodegradable polyesters, Renewable resources, Polyricinoleate, Thermal properties.

INTRODUCTION

Due to the increased amount of polymeric waste, industry and academy community must reconsider old and finding new ways for protection of the environment, which is affected by the way of disposal of this waste so far. Besides of the attempts for decreasing of polymeric waste through decreasing of sources, reusing of products, recycling or using it as an energy source, biodegradation of polymers imposes as a potential solution for this problem (Krochta & De Mulder-Johnston., 1996). Biodegradability is a desirable property for various applications, among all for obtaining of an eco-friendly polymeric materials and biomedical materials for temporary surgical interventions and as drug carriers. Biodegradable polymers find their application in many different areas such as packaging, in medicine, agriculture, pharmacy, the auto industry and so on. Biodegradability of ester bonds is well known, and that is why they are the subject of special interest of researchers. Polymers which contain ester bonds in the main chain are part of the huge group of polymeric materials which are distinguished by great diversity within them. Theoretically, all polyesters are potentially degradable in presence of water, which implies breaking of ester

bonds in the main chain. In practice, the hydrophobicity of aromatic polyesters doesn't allow water molecules to surround labile esters bonds, while only aliphatic polyesters with short methylene units between ester bonds degrade in a shorter period of time.

Synthesis of polyesters is usually stepwise polymerization of di-functional monomers (diacid and diols) in the polycondensation reaction, in which the by-product is usually water. Limitation for wider use of aliphatic polyesters based on diacids and diols are poor mechanical properties and low melting temperatures. Mechanical properties can be improved by controlled synthesis of polyesters which affect the supermolecular structure of polyesters. Recent experiments on parameters of synthesis showed that using very efficient catalysts, in reactions of esterification, together with applying vacuum can result in obtaining aliphatic polyesters based on diols and diacids with high molecular weight (Mochizuki et al., 1997). A special class of polyesters is homopolymers, obtained by self-polymerization of difunctional monomers (such as fatty acid). Hydroxy fatty acids, such as ricinoleic acid, can polymerize by the mechanism of esterification into linear or branched polyol with desired molecular weight and OH-terminated. Fatty acids are suitable for synthesis of biodegradable polymers (Cakić et al., 2016; Ristić et al., 2013;

---

* Corresponding author: vojislav.jovanovic@pr.ac.rs
CHEMISTRY

Ristić et al., 2012) because they are naturally part of a human organism, and because of hydrophobic property they keep encapsulated drug longer and can be used as drug carriers.

The functionality of polyester polyols can be successfully controlled by addition of low molecular weight compounds with favorable functionality, so-called starters (Ristić et al., 2013). Glycol as a starter will give diol while starter with higher functionality gives polyol with the same functionality as starting compound. Free side chains in hydroxyl fatty acids inhibit crystallization and improve hydrolitical stability of polyesters, and can be used as soft segments in the synthesis of thermoplastic polyurethanes (Xu et al., 2008). Polyester polyols based on fatty acid can be used also for segmented polyester preparation. For this reason, in this work, two series of polyester polyols were synthesized from methyl ricinoleate and from pure ricinoleic acid. Chemical structures and the influence of molecular weight on the thermal properties of obtained polyesters were characterized in details.

EXPERIMENTAL

Materials and methods

Ricinoleic acid and methyl ricinoleate were supplied from Sigma Aldrich, titanium(IV)-isopropoxide, as catalyst, was from TCI Chemicals. Tetrahydrofuran, p-toluene sulfonyl isocyanate, tetrabuthyl ammonium hydroxide, deuterated chloroform, tetramethylsilane were supplied from Sigma Aldrich, and used without any purification.

Hydroxyl number of polyol was determined according to standard ASTM E 1899-97 by employing reaction with p-toluene sulfonyl isocyanate (TSI) and potentiometric titration with tetrabuthyl ammonium hydroxide.

GPC chromatograms were recorded at Waters system with 510 pump and 410 differential refractometer. Tetrahydrofuran (THF) with a feed rate of 1.00 ml/min at 30 °C was used as eluent. Four Phenogel columns (300x7.8 mm ID; particle size 5 mm, pore size 50, 100, 103 and 104 A, respectively) with the addition of guard column Phenogel were used. Polystyrene with a range of molar masses 102 to 30000 g mol^{-1} was used as a standard.

Chemical composition and structure of polyesters were examined by ^{1}H NMR spectroscopy at instrument Bruker DPX-300 NMR (300 MHz), Switzerland. Polyester samples were dissolved in deuterated chloroform, and as referent standard tetramethylsilane was used.

FTIR analysis was done at instrument Spectrum-1000 Fourier transform infrared (FTIR) spectrometer, Perkin Elmer, Waltham, MA, USA, in a range of wavelengths from 400 to 4000 cm^{-1} with resolution 2 cm^{-1} and interval of 0.5 cm^{-1} with 16 scans by the sample.

The viscosity of the obtained polyester was measured on the AR rheometer 2000 ex, TA Instruments, New Castle, DE, USA. The samples were analyzed at a temperature of 25 ° C and the recording was done with 12 significant points with precisely determined shear stress values.

Transition temperatures of synthesized polyesters were determined using DSC method. DSC thermograms were recorded at DSC instrument Q100 (TA Instruments). Samples were first cooled to -90 °C, and then heated to 150 °C, by a heating rate of 10 °C min^{-1}.

Thermogravimetric analysis of polymers was performed at instrument TGA 2940 (TA Instruments) in a nitrogen atmosphere from room temperature to 500°C with a heating rate of 20 °C min^{-1}.

Synthesis of polyester

For the synthesis of polyesters, a method of high-temperature polycondensation was used. Unsaturated polyesters based on methyl ricinoleate and ricinoleic acid were synthesized. Both series of polyesters were synthesized by reaction of esterification or transesterification in the melt, starting from appropriate acids or methyl esters with diethylene glycol as a starter, in the presence of titanium(IV)-isopropoxide, Ti(iPrO)$_4$, as a catalyst, scheme 1.
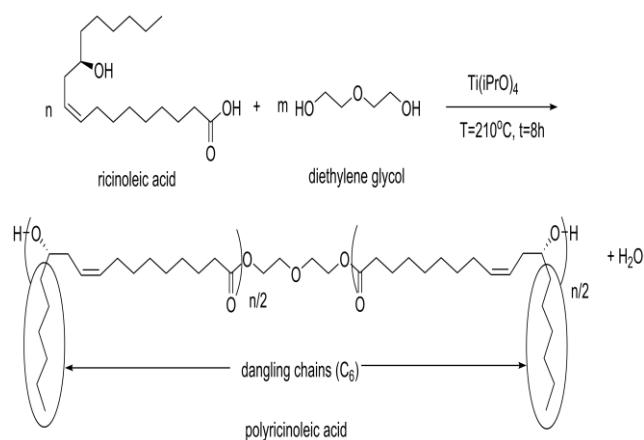
Scheme 1. Synthesis of polyricinoleate diol.

Into a 250 mL round-bottomed flask were charged appropriate amounts of methyl ricinoleate (or ricinoleic acid), diethylene glycol and catalyst. The mixture was heated at 200 °C under nitrogen purging and stirred with mechanical mixing. After the first phase, in which methanol is separated as a by-product during polymerization of methyl ricinoleate, or water in case of polymerization of ricinoleic acid, in the second phase under decreased pressure, polycondensation of created oligomers at 200 °C takes place for next 4h. Depending on the desired molar weight of polyester polyols different amounts of reaction components were added to the reactor, Table 1.

RESULTS AND DISCUSSION

Results of molecular weight analysis are summarised in Table 1. Molecular weights of obtained PRA-2000 and PMR-2000 diols are higher than expected (2000 g mol^{-1}), which is estimated according to the assumption that whole amount of diethylene. PRA and PMR abbreviations stand for samples synthesized from ricinoleic acid or methyl ricinoleate.

Expected molecular weight were calculated according to the equations 1a and 1b:

$$2000 = 106 + n(312,5-32) \quad (1a)$$
$$2000 = 106 + n(298,5-18) \quad (1b)$$

Where: 2000 is desired molecular weight of resulting polyester, n is number of moles, 312,5 (298,5) is molecular weight of methyl ricinoleate (ricinoleic acid) and 32 (18) is molecular weight of by-product, methanol (or water).

Deviation of obtained molecular weight from expected is probably due to loss of diethylene glycol within the polycondensation process at high temperature during separation of methanol. During polycondensation process, the small amount of diethylene glycol is lost which is the reason for obtaining polyricinoleate with higher molecular weight (Xu et al., 2008). Therefore, in other syntheses, a higher amount of diethylene glycol is added to control the molecular weight in the right way.

The obtained molar masses of poly(ricinoleic acid) are in good agreement with the expected, 4000 for the PRA-4000 and 6000 samples for the PRA-600 sample, Figure 1. GPC analysis of poly(methyl ricinoleate) PMR-4000 shows a molar mass of 4100 g mol^{-1} with polydispersity 1.39, Table 1. This narrow distribution of the molar mass can be explained by controlling the conditions of the synthesis, as well as by the presence of diethylene glycol, which is used as a chain extender and thus controls the molar mass. The degree of polydispersity of other samples is in the range of 1.33 to 1.49, which confirms the previous assertion about the effect of diethylene glycol on the molar mass of the polyester.

Table 1. Sample labels, formulation of reaction component for polyester polyol preparation and results of molecular weight analysis.

Sample	Ricinoleic acid, g (mol)	Methylricinoleate, g (mol)	Diethylene glycol, g (mol)	Mn, g mol^{-1} (GPC)	Q	M (calculated from OH number values)
PRA-2000	100 (0,338)	/	5,25 (0,049)	2690	1,49	2860
PRA-4000	100 (0,338)	/	2,56 (0,024)	4100	1,39	4056
PRA-6000	100 (0,338)	/	1,69 (0,016)	5980	1,33	6210
PMR-2000	/	100 (0,32)	5,03 (0,047)	3100	1,45	3506
PMR-4000	/	100 (0,32)	2,44 (0,023)	4250	1,35	4105
PMR-6000	/	100 (0,32)	1,61 (0,011)	6280	1,38	6240

PRA(PMR)-4000 is a sample synthesized from a ricinoleic acid (methyl ricinoleate) with the desired molecular weight of 4000 g mol^{-1}
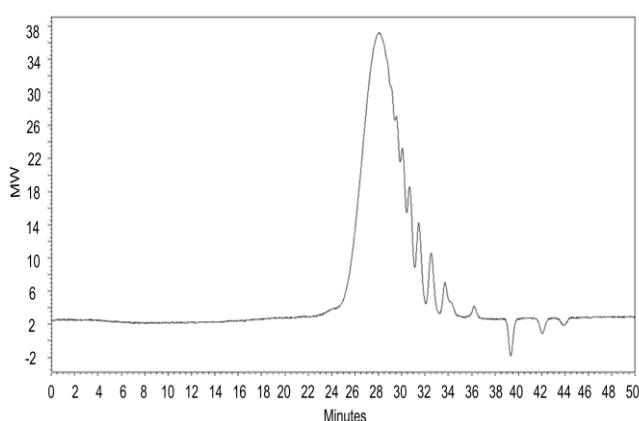
Figure 1. GPC chromatogram polyester poly(ricinoleic acid), PRA-2000.

The NMR spectrum of a poly(ricinoleic acid) synthesized in the presence of a chain extender, diethylene glycol, is shown in Figure 2. The structure and labeled characteristic protons whose displacements are detected on the ^{1}H NMR spectrum can be seen in the figure. Proton from the CH$_3$ group of the dangling chain, H1, appears at 0.87 ppm, while the protons from the -CH$_2$ group in dangling chain appears at 1.2 ppm. An obvious difference in the intensity of the peaks are observed, which is expected since the CH$_3$ and CH$_2$ group ration in the dangling chain is 1:5. CH$_2$ protons in the main chain appear at 1.7 ppm, proton H$_3$, while the C**H**$_2$-COO proton in the main chain shown a small peak at 2 ppm, proton H$_4$. The H5 proton with a peak at 2.3 ppm derives from the proton of the methylene group -CH=CH-C**H**$_2$-CH-(CH$_2$)-O-. Proton in the double bond in the main chain

-CH=CH- are at a position of 5.4 ppm, H_8. H_6 and H_7 denote the shift of the protons from ethylene glycol, whereby H_6 is 3.7 ppm from -CH$_2$-C**H$_2$**-O, while H_7 is 4.24 ppm of the protons -C**H$_2$**-O-C=O(CH$_2$).
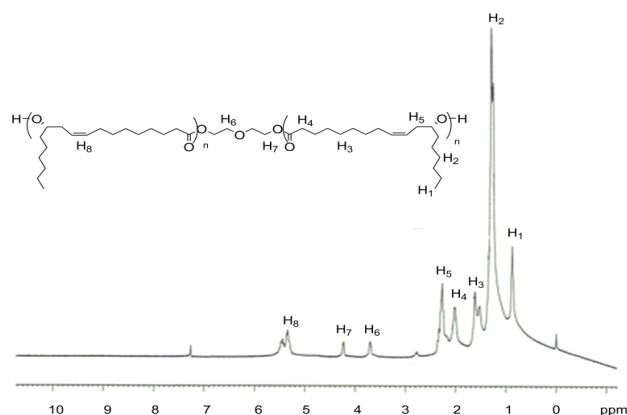
Figure 2. ^{1}H NMR spectra of polyester poly(ricinoleic acid), PRA-4000.

The FT-IR spectrum of methyl ricinoleate shows a wide band between 3650 and 3100 cm^{-1} which originates from the absorption of OH groups from the main chain, Figure 3. The position and shape of this strip are different for ricinic acid, due to the coupling of the OH group absorption in the main chain and OH group from -COOH, Figure 4.
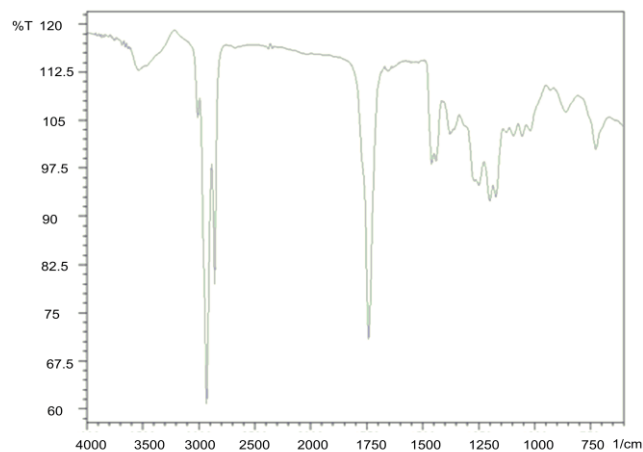
Figure 3. FT-IR spectra of methyl ricinoleate.

At low concentrations of hydroxyl in the polyester diol, the OH-group peak is split into two absorptions at 3410 and 3530 cm^{-1}, the first being attributed to OH groups that are hydrogen bonded and the other is from free OH groups. Deformation vibrations (δOH) of OH groups occurred at 1410 cm^{-1}. The band at 3007 cm^{-1} is originated from a double bond in the main monomer chain. This band is also present in the obtained polyester, which makes these materials more interesting in view of the possibility of subsequent linking of polymer chains. The characteristic band of carbonyl in the triglyceride ester appears at

1740 cm^{-1}, while in ricinolic acid the absorption of the same group occurs at substantially lower wavelengths, 1710 cm^{-1}. However, in the polyester, the absorption of the C=O group is shifted to 1740 cm^{-1} due to the formation of ester groups to connect the monomeric ricinic acid chains, Figure 5. The absorption of the ester C-O-C bond of the aliphatic chain shows a strong band with a position at 1180 cm^{-1}. Other bands that characterize the structure of the obtained polyester, such as the absorption of methyl and methylene groups in the region from 2800 to 2950 cm^{-1}, are also present in the FT-IR spectra of the resulting polymers.
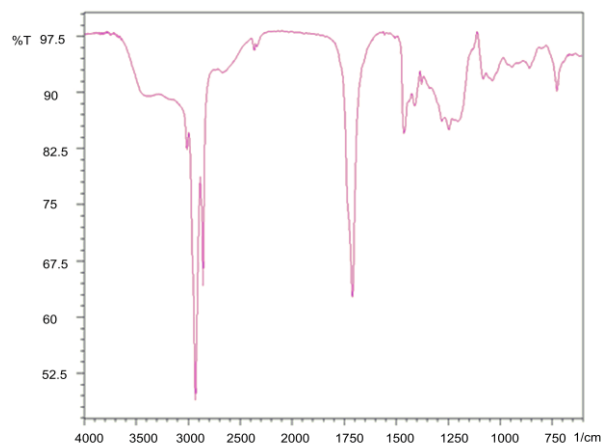
Figure 4. FT-IR spectra of ricinoleic acid.
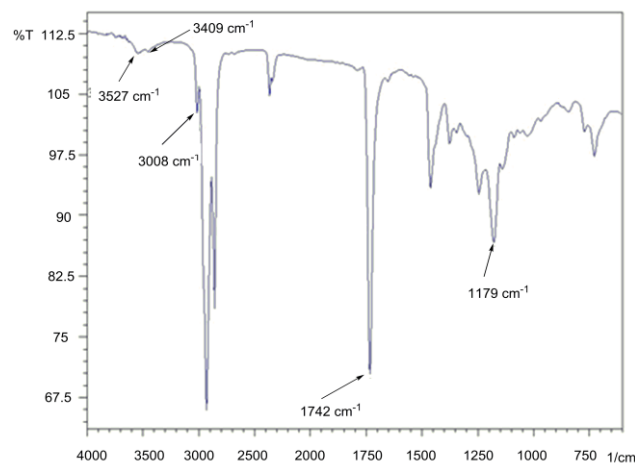
Figure 5. FT-IR spectra of poly(methyl ricinoleate), sample PMR-4000.

Figure 6 shows the viscosity dependence of the shear stress for the PMR-4000 sample. With this graph, the viscosity is calculated as the approximation to the zero stress. In this way, the resulting viscosity for the PMR-4000 sample is 1,390 Pa·s. These low viscosity values make it easy to process these materials, which significantly increases the possibility of their application. It is observed that as the molar weights increased and the viscosity of the samples increases, as it was expected, Figure 7. From the figure, the beginning of the plateau for a

molar mass of more than 4000 g mol⁻¹ is clearly seen. Thus, for polymers with a molecular weight greater than 4000 g mol⁻¹ the expected viscosity value is about 1.5 Pa s, which is in accordance with the literature data.
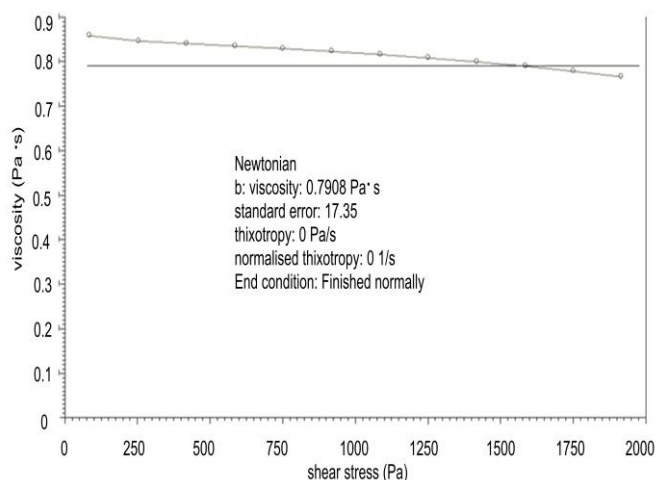
Figure 6. The viscosity of the PMR-2000 sample.

The samples synthesized from ricinoleic acid, having the same structure as the samples synthesized from methyl ricinoleate, and show a viscosity value that coincides with the previously explained dependence. The highest viscosity value has a PRA-6000 sample, 1.510 Pa· s, which also has the highest molar mass of 6000 g mol⁻¹, Figure 7.

The resulting polymers are characterized by a DSC method to determine the phase transition temperature. For polyesters derived from the methyl ester of ricinoleic acid and ricinoleic acid, the glass transition temperature is in the range -81 to -75 ° C, Table 2. This low Tg value is explained by the presence of dangling chains on the ricinolic acid molecules that further reduce the Tg value, Fig. 8 and 9. But with increasing of molecular weight influence of dangling chains decreasing, resulting in a higher value of Tg.
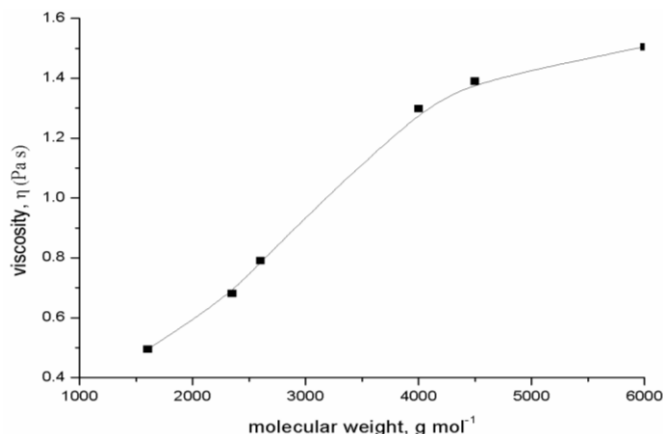
Figure 7. The viscosity dependence on the molar mass for the poly(ricinoleic acid) and poly(methyl ricinoleate).
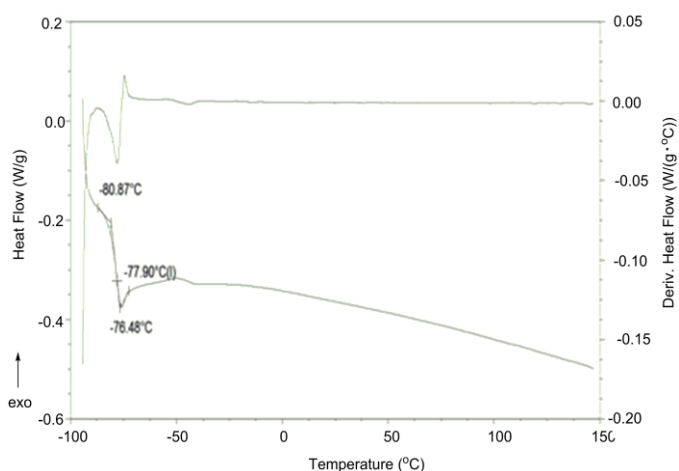
Figure 8. DSC thermogram of poly (methyl ricinoleate), PMR-2000.

Table 2. Thermal properties of synthesized polyesters.

Sample	Mn, g mol⁻¹ (GPC)	Tg, °C	T_{onset}, °C	DTG_{max}, °C
PRA-2000	2690	-81,24	321,56	357,24; 422,21; 510,87
PRA-4000	4100	-74,57	320,74	356,98; 431,11; 509,00
PRA-6000	5980	-71,56	327,65	359,02; 438,31; 508,98
PMR-2000	3100	-77,90	321,09	355,50; 429,25; 507,76
PMR-4000	4250	-74,01	321,75	351,64; 434,87; 511,28
PMR-6000	6280	-70,87	337,79	359,60; 440,05; 509,99
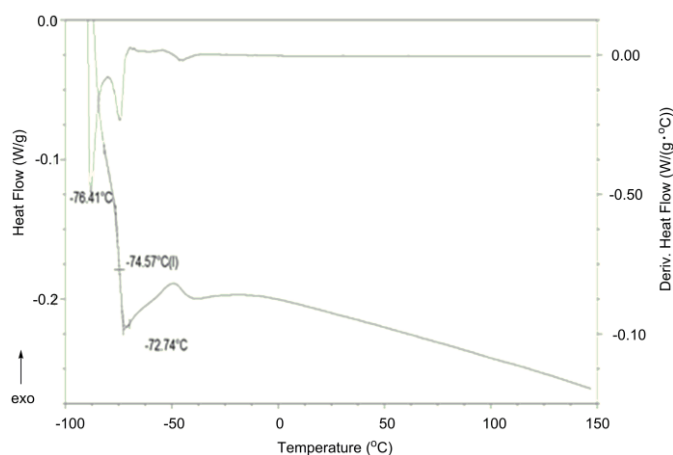
Figure 9. DSC thermogram of poly(ricinoleic acid) PRA-2000.
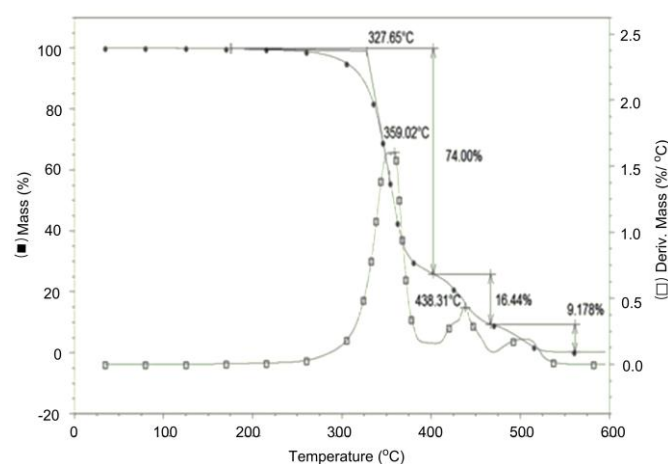
Figure 10. TG/DTG curve of poly(ricinoleic acid), PRA-6000.

Thermogravimetric analysis of synthesized polyester was performed in order to determine their temperature profile. The results of the TG analysis are summarized in Table 2. Figure 10 gives the views of a temperature degradation that takes place in three stages. In the first stage, ester bonds cleavage occurs and weight loss due to the degradation of diethylene glycol, as well as parts of ricinolic acid in dangling chains. In the first stage, up to 70% of the total sample weight is lost, which confirms the assumption of a possible degradation mechanism. As a result of ricinoleic acid degradation undecanoic acid and heptane may originate (Saunders & Frisch, 1963). Undecanoic acid is degraded in the first stage and heptane in the second. Also, due to the flexibility of the poly(ricinoleic acid) chains, during degradation, other low molecular compounds, whose degradation can occur in the third step, can also be generated. Due to the same chemical structure of polyricinoleic acid and poly methyl ricinoleate degradation profile of both series of synthesized samples are the same. Only with increasing of molecular weights slightly increasing of thermal stability are observed, Table 2.

CONCLUSION

In this paper, the synthesis of the polyester polyol based on ricinolic acid was successfully demonstrated. By using diethylene glycol, as the initiator of polymerization, the control of the molecular weight of the desired polyols was successful, which enables fine-tuning of the final properties of polyols. The FTIR and NMR spectroscopy were confirmed assumption about the polymerization mechanism, that is, diethylene glycol is incorporated into the middle of the polymer chain, i.e. that he had the role as initiator of polymerization. The DSC analysis showed that the glass transition temperatures of the synthesized polyols ranged from -70 to -80ºC, depending on the molar mass, and the control of the molar mass could influence the thermal properties of the polyol. Analysis of the thermal stability of the polyol showed that the molar mass does not significantly affect the thermal stability, since the degradation mechanics are the same for all samples, ie the degradation takes place in three stages.

ACKNOWLEDGMENTS

REFERENCES

Cakić, S. M., Ristić, I. S., M.-Cincović, M., Stojiljković, D. T., & B.-Simendić, J. 2016. Preparation and characterization of waterborne polyurethane/silica hybrid dispersions from castor oil polyols obtained by glycolysis poly(ethylene terephthalate) waste. International Journal of Adhesion and Adhesives, 70, pp. 329-341. doi:10.1016/j.ijadhadh.2016.07.010

Krochta, J. M., & De, M. C. L. C. 1996. Biodegradable Polymers from Agricultural Products. In G. Fuller, T. A. McKeon, & D. D. Bills Eds., Agricultural Materials as Renewable Resources, ACS Symposium Series..Washington, DC: American Chemical Society (ACS)., pp. 120-140. 647. doi:10.1021/bk-1996-0647.ch009

Mochizuki, M., Mukai, K., Yamada, K., Ichise, N., Murase, S., & Iwaya, Y. 1997. Structural Effects upon Enzymatic Hydrolysis of Poly(butylene succinate- co -ethylene succinate)s. Macromolecules, 30(24), pp. 7403-7407. doi:10.1021/ma970036k

Ristić, I. S., Bjelović, Z. D., Holló, B., Mészáros, S. K., Budinski-Simendić, J., Lazić, N., & Kićanović, M. 2013. Thermal stability of polyurethane materials based on castor oil as polyol component. Journal of Thermal Analysis and Calorimetry, 111(2), pp. 1083-1091. doi:10.1007/s10973-012-2497-x

Ristić, I. S., Budinski-Simendić, J., Krakovsky, I., Valentova, H., Radičević, R., Cakić, S., & Nikolić, N. 2012. The properties of polyurethane hybrid materials based on castor oil. Materials Chemistry and Physics, 132(1), pp. 74-81. doi:10.1016/j.matchemphys.2011.10.053

Ristić, I. S., Marinović-Cincović, M., Cakić, S. M., Tanasić, L. M., & Budinski-Simendić, J. K. 2013. Synthesis and properties of novel star-shaped polyesters based on l-lactide and castor oil. Polymer Bulletin, 70(6), pp. 1723-1738. doi:10.1007/s00289-013-0917-0

Xu, Y., Petrovic, Z., Das, S., & Wilkes, G. L. 2008. Morphology and properties of thermoplastic polyurethanes with dangling chains in ricinoleate-based soft segments. Polymer, 49(19), pp. 4248-4258. doi:10.1016/j.polymer.2008.07.027

Saunders, J. H., & Frisch, K. C. 1963. Polyurethane chemistry and technology.New York: Interscience. Part I, vol. 16., pp. 5.

A MINI-REVIEW OF ELECTROANALYTICAL METHODS FOR PESTICIDES QUANTIFICATION

SONJA JEVTIĆ[1*], DALIBOR STANKOVIĆ[2], ANJA JOKIĆ[1], BRANKA PETKOVIĆ[1]

[1] Faculty of Sciences, University of Priština, Kosovska Mitrovica, Serbia
[2] The Vinča Institute of Nuclear Sciences, University of Belgrade, Belgrade, Serbia.

ABSTRACT

This review paper shows the progress made in the last five years in electrochemical methods applied for the purpose of detection and quantification of pesticides - nowadays the most serious pollutants of the environment. Most pesticides can be successfully analyzed by chromatographic techniques, but because of high prices and immobility of the apparatus, the complexity of the method and the necessary special preparation of the samples, electrochemical methods have been recognized as an excellent alternative solution due to their advantages in speed, economy, simplicity and no exhaustive sample preparation. As the main limitation for use of this methods is electrochemical inactivity of many pesticides, this paper gives the essence of all elctroanalytical methods for pesticide quantification applied in last period, with an overview of the electrode materials and modifiers applied in a purpose to enhance analytical procedures application and characteristics of electrochemical sensors.

Keywords: Electroanalytical methods, Techniques, Pesticides quantification, Electrode modifiers.

INTRODUCTION

Nowadays, agricultural production has become unimaginable without the use of a variety of compounds that serve to increase the yield of the targeted plant culture, destroying weeds (herbicides), insects (insecticides) and fungus (fungicides). All these substances are covered by a common name - pesticides. Their significance in this area is borne out by the fact that the yield of agricultural crops would be about 50% smaller without the use of some of the pesticides, which would be a big problem, since the number of human population on a global level is increasing - only during the 20th century the population number rose from 1.65 billion to 6 billion ("The World at Six Billion"). And not only through agriculture, but also in other fields in everyday life, the use of pesticides raises the quality of our lives to a higher level (Damales, 2009). But, this application of pesticides has its price. Namely, the relationship between exposure to pesticides and many diseases has been established: Pakiston's disease, amyotrophic lateral sclerosis, diabetes, and numerous cancers. They are also the cause of respiratory diseases, nervous disorders, depression, hearing disorders, hepatitis, hormonal disorders, and so on. They remain long after use in soil and damage wild and domestic animals, birds and useful insects (Sanford et al., 2015; Andersson et al., 2014).

Evidently, it is essential to quickly, easily, efficiently, precisely and accurately determine the presence of pesticides in samples of any type. The most commonly used separation techniques are chromatography (gas (GC) and liquid (LC)) and mass spectrometry (MS). High performance liquid chromatography (HPLC) with mass or UV detection can determine a large number of pesticides with fulfilment of almost all the above conditions. Gas chromatography is used in combination with different detectors but is limited to volatile substances. Non-volatile substances can be converted into volatile derivatives and then detected and quantyfied by this technique. Another solution for those pesticides is their determination by the HPLC technique, but it should be noted that commercial detectors are limited in terms of selectivity and sensitivity. In addition, these techniques require a costly, non-mobile apparatus, special training for handling and interpreting results, as well as a special exhaustive sample preparation (Liang et al., 2014; Navaratne & Priyantha 2011).

The ideal method for determining pesticides is still being sought. Electrochemical methods have great predispositions in this field because they not only provide information on the quantitative content of pesticides, but also on the mechanisms of their oxidation and reduction, as well as on the possible products of decomposition. In addition, the equipment is cheaper and mobile and the measurement process is precise, accurate and fast, especially if it is performed on an unmodified electrode (Ni et al., 2014.). The disadvantages of unmodified electrodes can be overcome by modifying or coating the surface of the electrode with materials of different performances, which, if we use imagination, provides an unlimited number of possibilities.

Electrochemical methods and electrodynamics used in recent times for the determination of pesticides in real samples will be discussed in this review paper. Certainly, a prerequisite for electrochemical determination of all organic substances, as well as pesticides, is the presence of a group in a molecule that is electrochemically active in the working range of the selected

---

electrode. For example whether pesticides from the organochloride group can be determined electrochemically or not, depends on whether chlorine atoms can be separated from the rest of the structure. As their solubility in water is not satisfactory, determination of those compounds is performed in micellar water, usually by the differential pulse technique or by adsorptive stripping voltammetry (Bakirhan et al., 2018.). 38% of pesticides used on the global level are organophosphorus pesticides (Gothwal et al., 2014.) that contain a simple or double bond of bonded phosphorus and oxygen atoms, or phosphorus and sulfur, which is associated with their electrochemical activity. Triazines, compounds with a herbicidal effect, have two groups: s-triazine and asymmetric triazine with heterocyclic ring on which a reduction reaction occurs by protonation on nitrogen atom. Nitro pesticides, highly toxic compounds, are electrochemically active owing to the nitro group which usually passes into the form of hydroxylamine. Unlike them, sulphonylurea pesticides are low toxicity compounds rarely determined by electroanalytical methods. Bipyridinium pesticides are not all electrochemically active, and those that are, get reduced to nitro-monocations (Bakirhan et al., 2018.).

Next sections in this paper are dedicated to describing a purpose and advantages of electrochemical techniques, electrode materials and modifiers used in pesticide analysis. The summary of the basic data for pesticides electrochemically determined in the last five years are given in Table 1. Besides quantification methods and electrode modifiers, the table also contains data about used/optimal experimental conditions, method validation parameters and applied real samples.

ELECTROCHEMICAL TECHNIQUES IN PESTICIDE ANALYSIS

Electroanalytical determinations of pesticides usually were performed by pulse voltammetric techniques and amperometry, but sometimes cyclic voltammetry was used in this purpose (Figure 1).

Cyclic Voltammetry

Cyclic voltammetry (CV) is unavoidable in the electrochemical studies of not only pesticides, but also in many other electrochemically active organic and metal organic compounds. Although surpassed in the field of quantitative measurements, it remains an indispensable instrument for monitoring the oxidation and reduction mechanisms of the analyte as well as an indisputable indicator for possible intermediates (Skoog et al., 1997.). Cyclic voltammogram gives five important data: cathode and anode peaks corresponding to cathode and anode currents and the value of half potential. Those data, as well as their mutual relations, are parameters for determining the type of reaction on the electrode (reversible, irreversible, or quasi reversible) (Tonle & Ngameni, 2011.).
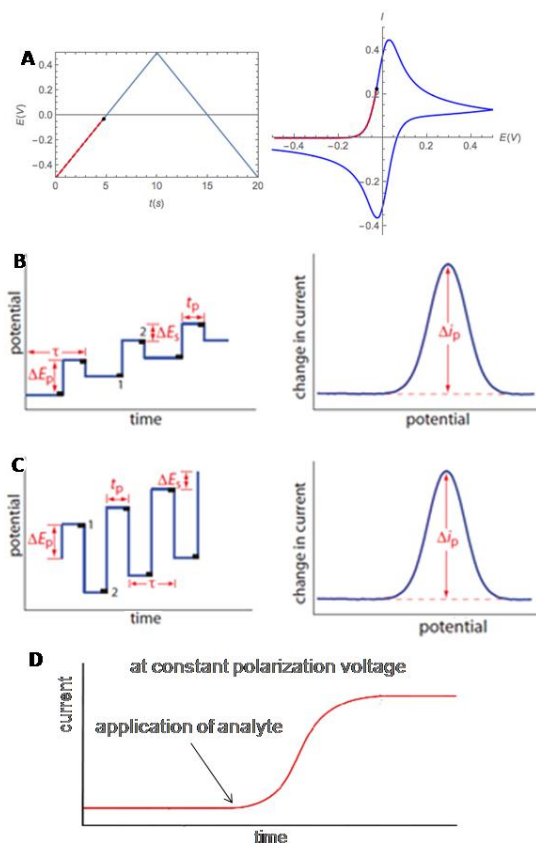
Fig. 1. Electrochemical techniques - parameters and characteristic voltammograms: A) cyclic voltammetry, B) differential pulse voltammetry, C) square-wave voltammetry and D) amperometry.

Any electrochemical pesticide investigation reported recently has been initiated by cyclic voltammetry. This is the perfect technique for confirming the success of the modification, as well as for finding the optimal conditions, the amount and the ratio of the modifiers. The concrete application of almost all electrodes modified in various ways is preceded by the precise recording of cyclic voltammograms. Thus, Olivera et al., 2014, using CV method came to optimum modifiers of the glassy carbon electrode. They combined two enzymes, laccase and tyrosinase, then enzymes with chitosan, and then enzymes, cytosan and gold nanoparticles. The last combination is due to the strongest current taken as optimal for the SWV quantification of ziram, carbaryl, propoxur and formethane pesticides. By studying the electrochemical behavior of relatively new pesticides, the first electrochemical data are obtained by cyclic voltammetry, using various electrodes and supporting electrolytes. Thus, the assumption that the herbicide pentoxamide can be determined electrochemically was precisely examined by Jevtić et al., 2018b., by CVs recorded in a potential range of -1.5 to 2 V in different pH values of Britton-Robinson buffer and based on a clear oxidation peak at +1.45 V. The quantification of this pesticide was performed with more suitable

square-wave voltammetric technique. Selva et al., 2017. showed that it is possible to determine pesticides from two groups (carbamates and organophosphates) in different concentrations precisely by cyclic voltammetry, and if more sensitivity is required, they proposed pulse methods.

Pulse methods

The key problem of voltammetric measurements is the insufficiently low detection limit as a direct consequence of the occurrence of a capacitive current. The solution to this problem was given by Barker and Jenkin in 1952. by introducing pulse methods among electrochemical analysis techniques. The essence of these methods is the same - electrode processes on working electrodes are triggered by pulse potential changes with a constant or increasing amplitude, which, at the end of the pulse duration, results in the measurement of the faradaic current, while at the same time the capacitive current almost completely disappears. The result of the measurement is the current peak whose height is directly proportional to the concentration of the analyte (Tonle & Ngameni, 2011.). The most commonly applicable are the differential pulse voltammetry (DPV) and square-wave voltammetry (SWV). In SWV, a potential in the form of symmetric square impulses is applied to the working electrode, and the current is recorded at two points - one at the end of the pulse, which causes a high value of the oxidative current, and one at the end of the pulse responsible for the jump in the reduction current. The resulting voltammogram is bell-shaped and its intensity is proportional to the concentration of the analyte. In DPV, the stimulating signal consists of small stepped pulses of constant potential, and the current is, as in the case of SWV, recorded in two points. How effective they are in the field of quantification of the target analyte shows the fact that the electrochemical determination of 85% of pesticides, after the first electrochemical data obtained by cyclic voltammetry, is quantified precisely by these methods. Costa et al., 2017. applied both types in the detection of methomyl pesticides, as was done by Jevtić et al., 2018a. in the detection of bentazone. In both cases, a small but significant advantage is given to DPV, but SWV is faster technique, and as it can be seen from Table 1, SWV is chosen for determination of pesticides in many cases. For the determination of three pesticides of chlorpropham, thiodicarb and aldicarb in soil, Babu et al. 2014. successfully applied DPV in combination with adsorptive stripping voltammetry.

Amperometry

Amperometry is based on the measurement of current that occurs as a result of the reduction or oxidation of electroactive species on the electrode (Mostafa, 2010.). The determination of almost all pesticides (in the target period of this review) by this method is in fact based on reducing the flow of current (inhibition) resulting from the decrease in the activity of acetylcholinesterase enzymes due to the action of very toxic pesticides from the group of organophosphates, rarely carbamates. The idea for this type of biosensor has came from the fact that pesticides (especially organophosphate type) are strong nurotoxins that act by esterifying a hydroxyl group of serine in acetylcholinesterase which is responsible for transmitting nerve impulses over the synapse. (Hassani et al., 2016.). Mogha et al., 2016. using a zirconium oxide electrode and a reduced graphene oxide in combination with immobilized acetylcholinesterase, quantified insecticide chlorpyrifos with the highest sensitivity in relation to the reported cases up to 10^{-13} M. The same insecticide, about one year earlier, was determined on a glassy carbon electrode modified by a combination of acetylcholinesterase, iron-oxide nanoparticles, and poly (indole-5-carboxylic acid) but with significantly less sensitivity (see Table 1). The insecticide of organophosphate type, methyl-paration was successfully amperometrically determined in vegetables and fruits by using an electrode that combines silver-graphene nanoribbons film and screen printed carbon electrode (Govindasamy et al., 2017.).

Potentiometry

Potentiometry involves measuring potential differences between the two electrodes, the indicator and the reference electrodes or between the two indicator electrodes separated by a semiconductor membrane, while there is no significant current flow between them. (Mostafa, 2010.). Potentiometry has not been particularly popular in the field of pesticide quantification lately, and this statement proves, as far as we can found, only one paper of this type reported in the last five years. Namely, Mashuni et al., 2016. quantified the diazinon - insecticide from the group of organophosphates with this method, using a golden electrode modified with an acetylcholinesterase immobilized in glutaraldehyde and cellulose acetate. After determining the optimal ratio of glutaraldehyde (25%) and cellulose acetate (15%), diazinone is quantified to a detection limit of 10^{-6} ppm where a stable potentiometric response is achieved in 5 min.

ELECTRODE MATERIALS

The effectiveness of electrochemical determinations depends to a large extent on the choice of the appropriate electrode material. An important criterion for this is the low background current, wide potential window, reproducibility, stability, and electron transfer kinetics. Adsorption is also an important factor because impurities or reaction products can deactivate the electrode, which would further require the electrode renewal (Uslu & Ozkan, 2007.).

Glassy carbon electrode

Although used for the first time in 1967, this electrode does not lose its significance, which is not surprising because it has a wide potential "window", it is solid, the surface is renewable and impermeable to gases, and it can be applied in negative

potentials and in the acidic environment (Sanghavi et al., 2015.). It is easily built up, polished and it is functional in the most commonly used solvents. The carbon atoms are sp² hybridized and arranged in layers as in the graphite, but more densely distributed and impregnation procedures are not required. It was found that this electrode material is significantly less oxidized in oxygen, carbon dioxide or water oxygen, than other carbon materials (Uslu & Ozkan, 2007.). Based on the data from the table, it could be concluded that the glassy carbon electrode (GC) is applied in almost 50% of the papers in the field of electrochemical determination of pesticides published in the last five years. It is very suitable for modification, and in most cases GC is modified, which results in better sensitivity and selectivity of determination. The only case where this electrode is not modified is the determination of pesticides of propoxur, paration, methyl parathion, carbofuran and carbaryl. The data about the detection limit and the linear potential is not given, since the purpose of the paper was to show that it is possible to separate pesticides from two classes of compounds (organophosphates and carbamates) on the basis of the fact that pesticides from the carbamate group have a peak at +1.4 V, and those of the organophosphate group at -0.6 V (Selva et al., 2017.). The applied modifiers are very diverse, ranging from those based on carbon nanoparticles (Teadoum et al., 2016; Xu F. et al., 2017; Xu G. et al., 2017; Irandoust & Haghighi 2016; Yao et al., 2014; Feng et al., 2015; Yang et al., 2015; Li et al., 2014;), to combinations of various types of nanoparticles with biocomponents (Cai et al., 2014; Chauhan et al., 2015; Guler et al., 2017; Zhang et al., 2015).

Carbon paste electrode

Carbon paste electrodes are essentially a mixture of graphite powder and water insoluble organic fluids, which after careful mixing is packaged in a suitable inert container with electrical contact on one side. The greatest advantage of this type of carbon electrode is its surface reproducibility as an important precondition for repeatability of results and low background currents. Its electrochemical properties depend on the applied organic fluids whose quantity must be selected so that it is enough to maintain the structure of the electrode, but in limited content, because the transfer of the electron would be disturbed and the background currents increased. This electrode is not selective, but is considered to be the most suitable for modifications, which indicates a number of possibilities used (Uslu & Ozkan, 2007.). For the determination of pesticides from the group of carbamates (chlorpropham, thiodicarb and aldicarb) in the soil, Babu et al., 2014. made an electrode of this type by mixing multi-walled nanotubes and castrol oils and packing the resulting mass into a Teflon tube. The achieved detection limit is about 1.09×10^{-7} M for each of mentioned pesticides. Pesticides carbaryl, propoxur formetanate and zyram were determined in citrus fruits with graphene-doped carbon paste electrode in combination with two enzymes, cytosan and gold nanoparticles.

This determination was advantageous in relation to the usual chromatographic determination in terms of speed and simplicity (Oliveira et al., 2014.).

Screen printed carbon electrode

A pesticide from the organophosphate group, methyl parathion is determined in fruit and plants using a modified screen printed electrode. The modification was done using silver nanoparticles supported by graphene nanotubes. The detection limit is 0.5 nM (Govindasamy et al., 2017.).

Two papers report a molecularly imprinted polymer electrode in combination with multidisciplinary nanoparticles and carbon monoxide for the detection of dichlorane. (Khadem et al., 2016; Shahtaheri et al., 2017.). Molecular imprinting is a technique in which a cocktail of functional monomers have reversible interaction with the target molecule using non-covalent forces. The complex is then networked and polymerized in the casting process, leaving behind a polymer with recognition sites complementary to the target molecule both in shape and functionality. Each such site consists of an induced molecular "memory" capable of selective binding to the chosen target sites (Jokanović, 2012.).

Gold electrodes

The limitation of the application of the gold electrode in the cathodic regions results in limitations in the analysis of the reducing substances. This problem is substantially resolved by the application of gold microelectrodes and the application of various types of modifiers (Fischer et al, 2011.). On the gold electrode Lin et al., 2017. applied a combination of anti atrazine and gold nanoparticles for modification, which significantly increased the surface area of the working electrode and under optimum conditions allowed detection of atrazine insecticide with a limit of 0.016 ng / mL. In the paper reported recently, the potentiometric biosensor was used, and the gold electrode is presented as carrier for acetylcholinesterase immobilized in glyceraldehyde and cellulose acetate. The insecticide diazinon from the organophosphate group was detected with detection limit of 10^{-6} ppm (Mashuni et al., 2016.). The gold electrode was also used by Ribeiro et al., 2014. as the basis for a modification with the laccase enzyme and gold nanoparticles to determine the pesticide formetanate hydrochloride with a good sensitivity of the magnitude of 10^{-8} M.

Boron-doped diamond electrodes

As a working electrode, the boron-doped diamond electrode possesses some remarkable features. Its exceptional performances confirms the fact that many pesticides were determined by this unmodified electrode, and modification was carried out in only two cases (carbaryl and paraquat) by graphene (Pop et al., 2017.). Compared to conventional carbon and metal electrodes, the boron-doped diamond electrode (BDDE) is significantly more inert and chemically stable, which makes it suitable for use in extreme chemical environments such as acidic solutions.

Table 1. List of pesticides with the most important data, determined electrochemically in period from 2014. to 2018.

Pesticide	Type	Chemical family	Electrode/ modifiers	Quantification method	pH, Electrolyte	Peak potential	Linear range	Detection limit	Applied sample	Ref.
Aldicarb	I	CB	MWCNT-PE	DPV and AdSV	pH 4 boric acid/ citric acid/ trisodium ortho phosphate	-0.45 V vs Ag/AgCl	10^{-5} to 10^{-10} M	1.09×10^{-7} M	soil	Babu et al., 2014.
Atrazine	H	TZ	anty-atrazine-AuNPs/GE	DPV	pH 5 phosphate buffer	0.21 V vs SCE	0.05 to 0.5 ng/mL	0.016 ng/mL	water	Liu et al., 2014.
Azametiphos	I	OPs	BDDE	SWV	pH 0 1 M nitric acid	1.7 V vs Ag/AgCl	2 to 100 μM	0.45 μM	river water	Vukojević et al., 2018.
Bentazone	H	TDZ	BDDE	DPV and SWV	pH 4 Britton-Robinson buffer	1.0 V vs Ag/AgCl	2 to 100 μM	0.5 μM	river water	Jevtić et. al., 2018.
Carbaryl	I	CB	LACC–TYR–AuNPs–CS/ GPE	SWV	pH 5.5 Britton–Robinson buffer	-0.6 V vs Ag/AgCl	9.90×10^{-8} to 2.91×10^{-6} M	1.98×10^{-8} M	citrus fruits	Oliveira et al., 2014.
			BDDE/GR	DPV	pH 5.6 acetate buffer	1.45 V vs. SCE	1 to 6 μM	0.07 μM	apple juice	Pop et al., 2017.
			GCE	/	pH 7 phosphate buffer	1.4 V vs Ag/AgCl	/	/	water	Selva et al., 2017.
Carbendazim	F	BI	Fullerene/MWCNT/ NA/GCE	SWV	pH 9 acetate buffer	0.67 V vs Ag/AgCl	2.0×10^{-8} to 3.5×10^{-7} M	1.7×10^{-8} mol/L	soil	Teadoum et al., 2016.
Carbofuran	I	CB	ITO/CoPc-AQ-LB	SWV	pH 7 phosphate buffer	1.20 V vs SCE	0.0397×10^{-6} to 2.82×10^{-6} M	5.81×10^{-7} M	water	Ipek et al. 2014.
			AChE/CNS/ GCE	AMP	pH 7.5 phosphate buffer	/	0.4 to 4.79 μg/L	0.082 μg/L	lettuce cabbage, oilseed	Cai et al., 2014.
			GCE	/	pH 7 phosphate buffer	1.4 V vs Ag/AgCl	/	/	water	Selva et al., 2017.

CHEMISTRY

Pesticide	Type	Chemical family	Electrode/ modifiers	Quantification method	pH, Electrolyte	Peak potential	Linear range	Detection limit	Applied sample	Ref.
Chlorpropham	H	CB	MWCNT-PE	DPV and AdSV	pH 4 boric acid/ citric acid/ trisodium ortho phosphate	-0.18 V vs Ag/AgCl	10^{-5} to 10^{-10} M	1.09×10^{-7} M	soil	Babu et al., 2014.
Chlorpyrifos	I	OPs	AChE /Pin5COOH/ Fe_3O_4NP/GCE	AMP	pH 7 phosphate buffer	/	1.5 to 70 nM	9.1 nM	water	Chauhan et al., 2015.
			AChE/ZrO_2/ RGO	AMP	pH 7 phosphate buffer	0.36 V vs Ag/AgCl	10^{-9} to 10^{-4} M	10^{-13} M	water	Mogha et al., 2016.
			CuO NFs-SWCNTs/GCE	DPV	pH 7 phosphate buffer	-0.35 V vs Ag/AgCl	0.1 to 150 ng/L	70 pg/mL	apple celery cabba-ge	Xu G. et al., 2017.
			NA/AuNPs/rGO -NH$_2$/ AChE/GCE	CV	pH 8 phosphate buffer	0.7 V vs Ag/AgCl	0.021 to 0.122 mg/mL	14 ng/mL	water	Guler et al., 2017.
			FTO-AuNPs-chl-Ab	DPV	pH 7.5 phosphate buffer	0.35 V	1 fM to 1 μM	10 fM	apple, pome-granae cabba-ge	Gandhi et al., 2018.
Clomazone	H	ISD	BDDE	SWV	pH 2 Britton-Robinson buffer	1.6 V vs Ag/AgCl	1 to 100 μM	0.21 μM	river water	Djurdjić et. al., 2018.
Diazinon	I	OPs	AchE/CA/GA/ GE	POT	pH 8 phosphate buffer	/	10^{-6} to 1 ppm	10^{-6} ppm	/	Mashuni et al., 2016.
Dicloran	F	NA	MWCNTs/ MIP/CPE	SWV	pH 8 phosphate buffer	0.1 V vs Ag/AgCl	1×10^{-6} to 1×10^{-9} mol/L	4.8×10^{-10} mol/L	urine and water	Khadem et al., 2016.
			MWCNTs/MIP/ CPE	SWV	pH 8 phosphate buffer	0.3 V	1×10^{-6} to 1×10^{-9} mol/L	4.8×10^{-10}	water, river water and urine	Shahtaheri et al., 2017.
Dimethylvi-nphos	I	OPs	RGO/CS/GCE	SWV	pH 6 Britton–Robinson buffer	-0.38 V vs Ag/AgCl	0.05 to 30.0 μg/L	0.036 mg/L	river water	Prasad et al., 2015.
Dinitramine	H	NP	MWCNT/GCE	SWV	pH 2 Britton–Robinson buffer	-0.50 V vs Ag/AgCl	4.0×10^{-8} to 1.4×10^{-6} mol/L	0.8×10^{-8} mol/L	water	Irandoust & Haghighi 2016.

CHEMISTRY

Pesticide	Type	Chemical family	Electrode/ modifiers	Quantification method	pH, Electrolyte	Peak potential	Linear range	Detection limit	Applied sample	Ref.
Eserine	I	CB	ITO/CoPc-AQ-LB	SWV	pH 7 phosphate buffer	-0.80 V vs SCE	0.00120×10^{-6} -1.42×10^{-6} M	6.40×10^{-9} M	water	Ipek et al., 2014.
Fenitrothion	I	OPs	AchE/CNS/GCE GCE	AMP /	pH 7.5 phosphate buffer pH 7 phosphate buffer	/ -0.6 V vs Ag/AgCl	6.26 to 125.31 µg/L /	2.61 µg/L /	lettuce cabbage, oilseed water	Cai et al., 2014. Selva et al., 2017.
Formetanate	I	CB	LACC–TYR–AuNPs–CS/ GPE Lacc /AuNPs/GE	SWV SWV	pH 5.5 Britton–Robinson buffer pH 5 Britton–Robinson buffer	-0.8 V vs Ag/AgCl 0.13 V vs Ag/AgCl	9.99×10^{-7} to 3.21×10^{-5} M 9.43×10^{-7} to 1.13×10^{-5}M	2.1×10^{-7} 9.5×10^{-8} M	citrus fruits fruits	Oliveira et al., 2014. Ribeiro et al., 2014;
Imidacloprid	I	NNC	BDDE	SWV	pH 7 0.05 M sodium sulfate	-1.21 V vs SCE	30 to 200 mmol/L	8.6 mmol/L	fruits	Ben Brahim et al., 2015.
Isoprocarb	I	CB	GCE	/	pH 7 phosphate buffer	1.4 V vs Ag/AgCl	/	/	water	Selva et al., 2017.
Linuron	H	UR	BDDE, BDDE/PtNPs	DPV	pH 2 Britton–Robinson buffer	1.29 V vs Ag/AgCl	0.61 to 26 µM/L	0.18 µM/L	water	Figueiredo-Filho et al., 2015.
Malation	I	OPs	AChE /Pin5COOH/ Fe_3O_4NP/GCE NA/AuNPs/rGO-NH_2/ AChE/GCE	AMP CV	pH 7 phosphate buffer pH 8 phosphate buffer	/ 0.7 V vs Ag/AgCl	0.1 to 60 nM 0.0063 to 0.077 mg/mL	6.6 nM 4.5 ng/mL	water water	Chauhan et al., 2015. Guler et al., 2017.
Melamine	H	TZ	MWCNTs-HTPB-PABFC	SWV	pH 7 phosphate buffer	0.8 V vs SCE	1×10^{-3} to 1×10^{-9} M	1.5×10^{-7} mol/L	Pear, apple, cucumber	Xu et al., 2017.
Methidathion	I	OPs	NA/AuNPs/rGO-NH_2/ AChE/GCE	CV	pH 8 phosphate buffer	0.7 V vs Ag/AgCl	0.012 to 0.105 mg/mL	9.5 ng/mL	water	Guler et al., 2017.

CHEMISTRY

Pesticide	Type	Chemical family	Electrode/ modifiers	Quantification method	pH, Electrolyte	Peak potential	Linear range	Detection limit	Applied sample	Ref.
Methiocarb	I	CB	BDDE	DPV	pH 6.62 citrate buffer	1.4 V vs Ag/AgCl	1 to 55 mg/mL	0.15 mg/mL	water	Chylkova at al., 2015.
Methomyl	I	CB	BDDE	DPV and SWV	pH 2 and 3 Britton–Robinson buffer	1.61 V 1.69 V vs Ag/AgCl	$6.6–42.0\times10^{-5}$ $5.0–410.0\times10^{-6}$ mol/L	1.2×10^{-6} and 1.9×10^{-5} mol/L	river water	Costa et al., 2017.
Methylpara-thion	I	OPs	GdHCF/GNs/ GCE	DPV	pH 6 phosphate buffer	-0.591 V vs SCE	0.008 to 10 mM	1 nM	water	Li et al., 2014.
			f-SWCNT–b-CD/GCE	DPV	pH 6 phosphate buffer	0 V vs SCE	0.002 to 17.5 μgm/L	0.4 ng/mL	crops	Yao et al., 2014.
			ZnO/Ag/ MPTMS/OHP	DPV	pH 7 phosphate buffer	0.4 Vvs Ag/AgCl	2.5 nM to 75 μM	0.07 nM	water	Thota et al., 2015.
			Ag-GNRs/SPCE	AMP	pH 7 phosphate buffer	-0.2 V vs Ag/AgCl	0.005 to 2780 μM /ml	0.5 nM/ml	Vege-tables and fruits	Govinda-samy et al., 2017.
			GCE	/	pH 7 phosphate buffer	-0.6 V vs Ag/AgCl	/	/	water	Selva et al., 2017.
Naftalofos	I	OPs	RGO/CS/GCE	SWV	pH 6 Britton–Robinson buffer	-0.63V vs Ag/AgCl	0.05 to 30.0 μg/L	0.044 mg/L	river water	Prasad et al., 2015.
Paraquat	H	BPy	BDDE/GR	DPV	pH 5.6 acetate buffer	-0.78 V vs SCE	0.2 to 1.2 μM	0.01 μM	apple juice	Pop et al., 2017;
Parathion	I	OPs	GCE	/	pH 7 phosphate buffer	-0.6 V vs Ag/AgCl	/	/	water	Selva et al., 2017.
Pentachloro-phenol	I, H	OC	ZnSe QDs-MWCNTs/GCE	DPV	pH 4 phosphate buffer	0.85 V vs SCE	8.0×10^{-8} to 4.0×10^{-6} mol/L	2.0×10^{-9} mol/L	fish meat	Feng et al., 2015.
Pethoxamid	H	OC	BDDE	SWV	pH 4 Britton-Robinson buffer	1.35 V vs Ag/AgCl	3 to 100 mM	1.37 mM	river water	Jevtić et. al., 2018.
Phoxim	I	OPs	AchE/ AgNPs/rGO/ GCE	DPV	pH 7 phosphate buffer	0.66 V vs Ag/AgCl	0.2 to 250 nM	81 pM	water	Zhang et al., 2015.

CHEMISTRY

Pesticide	Type	Chemical family	Electrode/ modifiers	Quantification method	pH, Electrolyte	Peak potential	Linear range	Detection limit	Applied sample	Ref.
Propoxur	I	CB	LACC–TYR–AuNPs–CS/GPE	SWV	pH 5.5 Britton–Robinson buffer	-0.2 V vs Ag/AgCl	4.99×10^{-7} to 1.92×10^{-5} M	1.87×10^{-7} M	citrus fruits	Oliveira et al., 2014;
			GCE	/	pH 7 phosphate buffer	1.4 V vs Ag/AgCl	/	/	water	Selva et al., 2017.
Pyrimethanil	F	AP	MWCNTs-IL/GCE	DPV	pH 6 phosphate buffer	0.82 V vs SCE	1.0×10^{-7} to 1.0×10^{-4} mol/L	1.6×10^{-8} mol/L	orange apple water	Yang et al., 2015.
Thiodicarb	I	CB	MWCNT-PE	DPV and AdSV	pH 4 boric acid/ citric acid/ trisodium orthophosphate	-0.39 V vs Ag/AgCl	10^{-5} to 10^{-10} M	1.07×10^{-7} M	soil	Babu et al., 2014.
Trichlorfon	I	OPs	MWCNTs-HTPB-PABFC	SWV	pH 7 phosphate buffer	0.49 V vs SCE	1×10^{-3} to 1×10^{-9} M	3.5×10^{-8} mol/L	pear apple cucumber	Xu et al., 2017.
Ziram	F	CB	LACC–TYR–AuNPs–CS/GPE	SWV	pH 5.5 Britton–Robinson buffer	-0.6 V vs Ag/AgCl	4.99×10^{-7} to 1.92×10^{-5}	1.87×10^{-7} M	citrus fruits	Oliveira et al., 2014.

Pesticide types: F - fungicide; H - herbicide; I - insecticide; Chemical family: AP - anilinopyrimidine; BI - benzimidazole; BPy - bipyridilium; CB - carbamates; ISD - isoxazolidinone; NA - nitroaniline; NNC - neonicotinoid; NP - nitropesticides; OC - organochlorines; OPs - organophosphate; TDZ - tiadizine; TZ - triazine; UR-urea pesticide. **Electrode/ modifiers:** AChE - acetylcholinesterase; AgNPs - silver nanoparticles; AuNPs - goldcnanoparticles; BDDE - boron-doped diamond electrode; CA - cellulose acetate; GA - glutaraldehyde; chl-Ab - chlorpyrifos antibodies; CNS - carbon nanosphere; CoPc-AQ- cobalt phthalocyanineanthraquinone hybrid; CPE - carbon paste electrode; CS - chitosan; CuO NFs - copper oxide nanoflowers; Fe$_3$O$_4$NP - iron oxide nanoparticles; f-SWCNT–b-CD - carboxylic acid-functionalized single-walled carbon nanotubes–b-cyclodextrin; FTO - fluorine doped tin-oxide; GCE - glassy carbon electrode; GdHCF - gadolinium hexacyanoferrate; GE -gold electrode; GNRs - graphene nanoribbons film; GNs - graphene nanosheets; GPE - graphene doped carbon paste electrode; GR - graphene; HTPB - hydroxyl-terminated polybutadiene; IL - ionic liquids; ITO - indium tin oxide; LACC - laccase; LB - Langmuir–Blodgett monolayer film; MIP - molecularly imprinted polymer; MPTMS - mercaptopropyltrimethoxysilane layers; MWCNT - multiwalled carbon nanotubes; NA - nafion; OHP - overhead projector films; PABFC - poly 4-acryloyloxybutyl(ethyl) ferrocene carboxylates; Pin5COOH - poly(indole-5-carboxylic acid); RGO - reduced graphene oxide; rGO-NH$_2$ - amine functionalized reduced graphene oxide; SPCE - screen printed carbon electrode; SWCNTs - single walled carbon nanotubes; TYR - tyrosinase; ZnSe QDs - ZnSe quantum dots; ZrO$_2$ - zirconium oxide. **Quantification methods:** AMP - amperometry; CV- cyclic voltammetry; DP-AdSV - differential pulse adsorptive stripping voltammetry; DPV - differential pulse voltammetry; POT potenciometry; SWV- square wave voltammetry.

In addition, it has the widest potental "window" (from -2V to 2V) of all reported electrodes, a small basic current, a large overvoltage in the separation of hydrogen and oxygen, and good mechanical performance (Uslu & Ozkan, 2007.). Jevtić et al., 2018a. applied BDDE for the determination of bentazone herbicide in river waters with significant advantages in terms of speed, sensitivity, simplicity, repeatability and efficiency compared to previously reported procedures for its quantification. The sensitivity of the method is 0.5. The electrochemical reduction of imidacloprid insecticide on BDDE was first performed by Benbrahim et al. 2015. The quantification was efficiently executed by SWV in fruit with high accuracy and

CHEMISTRY

precision. The first data on the electrochemical behavior of pentoxamid were given by Jevtić et al. 2018b. The assay was carried out in Britton-Robinson buffer at pH 4 and the result was an anode peak at 1.35 V *vs* reference Ag/AgCl electrode. With a detection limit of 1.37 µM this method is proposed as a fast, cheaper and simpler alternative to conventional chromatography. A similar situation exists in the case of detection of metiocarb with a detection limit of 0.15 mg / ml (Chylkova et al., 2015.), methomyl in commercial products and water with a detection limit of 1.2×10^{-6} mol / L (Costa et al ., 2017.) and clomazone in surface waters with a detection limit of 0.2 µM (Djurdjić et al., 2018.).

ELECTRODE MODIFIERS

Nanomaterials

Intensive efforts to improve selectivity and sensitivity in determining the most serious pesticide pollutants today have led to the mass introduction of nanomaterials in electrochemistry (Govindhan et al., 2014.). The International Organization for Standardization of Nanomaterials defines them as materials whose particles are between 1 and 100 nm. In combination with modern electrochemical techniques, they are a very effective instrument for controlling pollution due to significant advantages such as effective catalysis, rapid mass transport and large surface area (Saini et al., 2017.). Nanomaterials that have been used in the target period as modifiers are discussed below, and their connection with the electrodes on which they are applied and numerous other data are given in Table 1. As it can be seen, carbon materials were extensively used as electrode materials and also as electrode modifiers. Structures of mentioned carbon materials were presented in Figure 2.

Carbon nanotubes (CNTs)

Carbon nanotubes exist in the form of single-walled nanotubes that contain one layer of graphene curved in the tube (SWNTs) and multi-walled nanotubes containing several layers in the form of tubes concentrated around the same axis (MWNTs). They are characterized by good conductivity, stability, flexibility and reactivity. Despite the difficulties in isolating single-walled nanotubes, their application was reported in the analysis of chlorpyrifos, insecticides from the organophosphate group, with a detection limit of 70 pg / ml under optimal conditions. They are applied in combination with copper-oxide nanoparticles to GCE. The sensor is easily regenerated by urea and allows detection of this pesticide with excellent selectivity (Xu G. et al., 2017.). In combination with cyclodextrin, the GC nanoparticles were applied for the purpose of analyzing methyl parathion in plant specimens where a detection limit of 0.4 ng / ml was reached (Yao et al., 2014.).
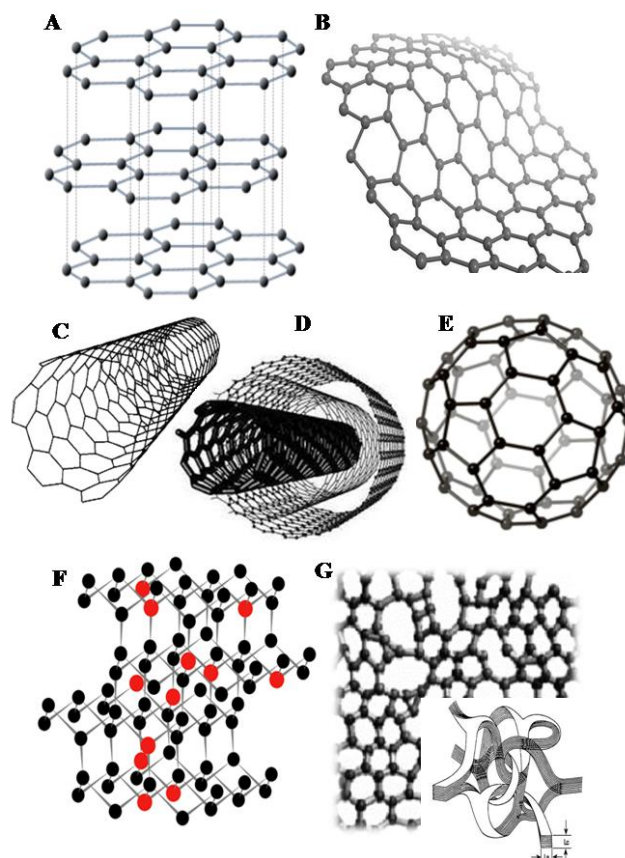
Fig. 2. Carbon material used as electrode materials and modifiers: A) graphite, B) graphene, C) single-walled carbon nanotubes, D) multi- walled carbon nanotubes, E) fullerene, F) boron-doped diamond and G) glassy carbon.

Graphene

Graphene, either in its basic form or in the form of oxide or reduced oxide, possesses unique physico-chemical properties very suitable for use, among others in electrochemistry (Zeng et al., 2016.). The reported case of BDDE modification by graphene led to significantly enhanced pixel intensity in relation to the application of an unmodified electrode. Simultaneous detection of pesticide paraquat and carbaryl in apple juice was performed by DPV technique with a detection limit of 0.01 µM and 0.07 µM respectively. (Pop et al., 2017.). Prasad et al., 2015. determined dimethylvinphos and naphthalofos using GCE modified reduced graphene oxide and ciosane. The electrochemical response was significantly better than that without the presence of graphene derivative, which was explained by the strong absorption of targeted pesticides on the film of the modifier, and due to its excellent conductivity. The large surface area significantly improved the sensitivity of the method. Graphene-oxide nanotubes are not as popular as other graphene derivatives, but were successfully applied in combination with silver particles and screen printed technology for methyl paration detection. The electrocatalytic ability of

CHEMISTRY

silver in combination with the good properties of these nanotubes (good conductivity, large contact surface and catalytic capacities) make this sensor very suitable for the detection of the mentioned pesticide in fruit and vegetables with a detection limit of 0.5 nM (Govindasamy et al., 2017.).

Fullerene

The behavior of graphene and carbon nanotubes is very similar to the behavior of fullerene, the difference lies in the larger surface of the graphene due to its one-layer structure. In spite of that, the chemical activity of the graphene is lower than the indicated fullerene (Chehimi & Pinson 2013.). Fullerene, in combination with multidisciplinary nanoparticles and nafion, was used to detect carbendazim fungicide from benzimidazole with a detection limit of 10^{-8} mol / L. (Teadoum et al., 2016.).

Biocomponents and Metal nanoparticles

The biosensors for detection of pesticides function on the principle of loss of activity of the biocomponent due to the smallest amount of highly toxic pesticides, or on the direct interaction of biocomponents with targeted analytes (Sassolas et al., 2012.). In past five years, the most commonly used bio-component in biosensors for pesticide analysis is the acetylcholinesterase enzyme, and in almost all cases it is applied in combination with some nanoparticles. Zhang et al., 2015. determined pesticide phoxim using a combination of acetylcholinesterase, gold nanoparticles and reduced graphene oxide. Acetylcholinesterase, in normal conditions, naturally accelerates the decomposition of acetylcholine chloride to thiocholine, which is electro-active. Reduction of this electroactivity in electrochemical measurements is proportional to the presence of phoxim. On this principle, its application in combination with Fe_3O_4 NPs for the amperometric detection of chlorpyrifos which reach LOD of 9.1 nM. (Chauhan et al., 2015.), and in combination with carbon nanoferms for the detection of carbofuran and phenitrothion (Cai et al., 2014.), was presented. Laccase and tyrosinase enzymes for voltammetric detection of ziram, propoxur, carbaryl and formetanates were used together with golden nanoparticles and cytosan. The sensor shows better characteristics in the presence of both enzymes, compared to the presence of only one of them. The reason for this synergy effect is a stronger flow of electricity due to their simultaneous catalytic action on phenol compounds (Oliveira et al., 2014.).

As can be seen, from metal nanoparticles, lately, the gold nanoparticles have undoubtedly been the most popular. Althought gold is considered to be an inert material in redox exchanges, in nano scale it becomes an excellent component for making chemical and biological sensors (Tang & Tang 2015.). Guler et al., 2017. used these nanoparticles in combination with reduced graphene oxide, naphion and enzyme acetylcholinesterase for the detection of chlorpyrifos, malathion and methidathion, and in a similar combinations, without nafion

the insecticide proxima was also selected (Zhang et al., 2015.). Fluorine doped tin oxide, chlorpyrifos antibodies, and gold nanoparticles are the combination for detection of chlorpyrifos with a detection limit of 10 μM (Gandhi et al., 2018.).

Cytosan is one of the most commonly used natural polymers. Its presence provides a suitable biocompatible environment for enzymes. It is also easily formed into films or any other form (Arduini et al., 2016). With the reduced graphene oxide on GC electrode it was used to detect naphthalofos and dimethylvinphos by a group of researchers, Prasad et al., 2015

The exceptional specificity of the antigen-antibody interaction found its place in electrochemistry. Liu et al., 2014. determined atrazines with a combination of anti-atrazine with gold nanoparticles applied to the gold electrode with a detection limit of 0.016 ng / mL. With fluorine-doped tin oxide (FTO) and gold nanoparticles, anti-chlorpyrifos antibodies for the detection of chlorpyrifos were combined. (Gandhi et al., 2018.). The FTO has the role of a modifier carrier on gold or carbon-based electrodes.

CONCLUSION

A literature review brings us to a conclusion that electrochemical techniques have a good chance of replacing conventional chromatographic pesticide quantification in future. Cyclic voltammetry remains an indispensable instrument for observing reaction mechanisms, while amperometry, and especially pulse methods, are applied to achieve as low as possible detection limits. The sensitivity and selectivity of the products from year to year are getting better owing to the use of electrodes of various performances additionally enhanced by modification using different materials. In this field, the popularity of nano-sized materials, especially those based on carbon, is evident. The use of biomaterials, enzymes and antibodies, as well as combinations of biomaterials and nanoparticles, also greatly contributed to the improvement of the techniques.

In the future, the goals are in speed simplifying and speeding up the method, lowering the detection limits, increaseing selectivity and, in view of the nature of pesticide contamination, finding a suitable way to monitor them on the ground in all conditions and real samples. Different combinations of electrochemical techniques, electrode materials, modifiers, and production techniques, miniaturization due to construction of microelectrodes, taking the best of all, almost certainly prove that these goals of application of electroanalytical methods in pesticide control are highly achievable.

CHEMISTRY

REFERENCES

Arduini, F., Cinti, S., Scognamiglio, V., & Moscone, D. 2016. Nanomaterials in electrochemical biosensors for pesticide detection: advances and challenges in food analysis. Microchimica Acta, 183(7), pp. 2063-2083. doi:10.1007/s00604-016-1858-8

Babu, T. R., Reddy, S. R., & Sujana, P. 2014. Comparative voltammetric study and determination of carbamate pesticide residues in soil at carbon nanotubes paste electrodes. Journal of Electrochemical Science and Engineering, doi:10.5599/jese.2013.0041

Bakirhan, N. K., Uslu, B., & Ozkan, S. A. 2018. Food Safety and Preservation. Netherlands: Elsevier.

Ben, B. M., Belhadj, A. H., Abdelhédi, R., & Samet, Y. 2016. Electrochemical behavior and analytical detection of Imidacloprid insecticide on a BDD electrode using square-wave voltammetric method. Chinese Chemical Letters, 27(5), pp. 666-672. doi:10.1016/j.cclet.2015.12.032

Cai, J., Zhou, L., & Han, E. 2014. A Sensitive Amperometric Acetylcholine Biosensor Based on Carbon Nanosphere and Acetylcholinesterase Modified Electrode for Detection of Pesticide Residues. Analytical Sciences, 30(6), pp. 669-673. doi:10.2116/analsci.30.669

Chauhan, N., Narang, J., & Jain, U. 2016. Amperometric acetylcholinesterase biosensor for pesticides monitoring utilising iron oxide nanoparticles and poly(indole-5-carboxylic acid).Journal of Experimental Nanoscience, 11(2), pp. 111-122. doi:10.1080/17458080.2015.1030712

Chehimi, M. M., & Pinson, J. 2013. Applied surface chemistry of nanomaterials. New York: Nova publishers.

Chýlková, J., Tomášková, M., Švancara, I, Janíková, L., & Šelešovská, R. 2015. Determination of methiocarb pesticide using differential pulse voltammetry with a boron-doped diamond electrode. Analytical Methods, 7(11), pp. 4671-4677. doi:10.1039/c5ay00979k

Costa, D. J. E., Santos, J. C. S., Sanches-Brandão, F. A. C., Ribeiro, W. F., Salazar-Banda, G. R., & Araujo, M. C. U. 2017. Boron-doped diamond electrode acting as a voltammetric sensor for the detection of methomyl pesticide. Journal of Electroanalytical Chemistry, 789, pp. 100-107. doi:10.1016/j.jelechem.2017.02.036

Damalas, C. A. 2009. Understanding benefits and risks of pesticide use. review. Scientific Research and Essay, 4(10), pp. 945-949.

Djurdjić, S., Vukojević, V., Jevtić, S., Pergal, M. V., Petković, B. B., & Stanković, D. M. 2018. Herbicide Clomazone Detection Using Electroanalytical Approach Using Boron Doped. Int. J. Electrochem. Sci. . Diamond Electrode. Int. J. Electrochem. Sci., 13, pp. 2791 – 2799. doi: 10.20964/2018.03.39

Feng, S., Yang, R., Ding, X., Li, J., Guo, C., & Qu, L. 2015. Sensitive electrochemical sensor for the determination of pentachlorophenol in fish meat based on ZnSe quantum dots decorated multiwall carbon nanotubes nanocomposite. Ionics, 21(12), pp. 3257-3266. doi:10.1007/s11581-015-1512-1

Figueiredo-Filho, L. C. S., Sartori, E. R., & Fatibello-Filho, O. 2015. Electroanalytical determination of the linuron herbicide using a cathodically pretreated boron-doped diamond electrode: comparison with a boron-doped diamond electrode modified with platinum nanoparticles. Analytical Methods, 7(2), pp. 643-649. doi:10.1039/c4ay02182g

Fischer, J., Dejmkova, H., & Barek, J. 2011. Electrochemistry of Pesticides and its Analytical Applications. Current Organic Chemistry, 15(17), pp. 2923-2935. doi:10.2174/138527211798357146

Gothwal, A., Beniwal, P., Dhull, V., & Hooda, V. 2014. Preparation of Electrochemical Biosensor for Detection of Organophosphorus Pesticides. International Journal of Analytical Chemistry, 2014, pp. 1-8. doi:10.1155/2014/303641

Govindasamy, M., Mani, V., Chen, S., Chen, T., & Sundramoorthy, A.K. 2017. Methyl parathion detection in vegetables and fruits using silver@graphene nanoribbons nanocomposite modified screen printed electrode. Scientific Reports, 7(1). doi:10.1038/srep46471

Guler, M., Turkoglu, V., & Basi, Z. 2017. Determination of malation, methidathion, and chlorpyrifos ethyl pesticides using acetylcholinesterase biosensor based on Nafion/Ag@rGO-NH2 nanocomposites. Electrochimica Acta, 240, pp. 129-135. doi:10.1016/j.electacta.2017.04.069

Hassani, S., Momtaz, S., Vakhshiteh, F., Maghsoudi, A. S., Ganjali, M. R., Norouzi, P., & Abdollahi, M. 2017. Biosensors and their applications in detection of organophosphorus pesticides in the environment. Archives of Toxicology, 91(1), pp. 109-130. doi:10.1007/s00204-016-1875-8

İpek, Y., Şener, M. K., & Koca, A. 2015. Electrochemical pesticide sensor based on Langmuir–Blodgett film of cobalt phthalocyanine-anthraquinone hybrid. Journal of Porphyrins and Phthalocyanines, 19(05), pp. 708-718. doi:10.1142/s1088424615500182

Irandoust, M., & Haghighi, M. 2016. Electrochemical Study and Determination of Dinitramine Using Glassy Carbon Electrodes Modified with Multi-walled Carbon Nanotubes. Electrochemistry, 84(4), pp. 228-233. doi:10.5796/electrochemistry.84.228

Jevtić, S., Stefanović, A., Stanković, D. M., Pergal, M. V., Ivanović, A. T., Jokić, A., & Petković, B. B. 2018. Boron-doped diamond electrode — A prestigious unmodified carbon electrode for simple and fast determination of bentazone in river water samples. Diamond and Related Materials, 81, pp. 133-137. doi:10.1016/j.diamond.2017.12.009

Jevtić, S., Vukojević, V., Djurdjić, S., Pergal, M. V., Manojlović, D. D., Petković, B. B., & Stanković, D. M. 2018. First electrochemistry of herbicide pethoxamid and its quantification using electroanalytical approach from mixed commercial product. Electrochimica Acta, 277, pp. 136-142. doi:10.1016/j.electacta.2018.05.004

CHEMISTRY

Jokanović, V. 2013. Nanomedicina - najveći izazov 21. veka. Beograd: Data status.

Khadem, M., Faridbod, F., Norouzi, P., Foroushani, A. R., Ganjali, M. R., & Shahtaheri, S. J. 2016. Biomimetic electrochemical sensor based on molecularly imprinted polymer for dicloran pesticide determination in biological and environmental samples. Journal of the Iranian Chemical Society, 13(11), pp. 2077-2084. doi:10.1007/s13738-016-0925-8

Li, Y., Xu, M., Li, P., Dong, J., & Ai, S. 2014. Nonenzymatic sensing of methyl parathion based on graphene/gadolinium Prussian Blue analogue nanocomposite modified glassy carbon electrode. Analytical Methods, 6(7), p. 2157. doi:10.1039/c3ay41820k

Liang, H. C., Bilon, N., & Hay, M. T. 2014. Analytical Methods for Pesticide Residues. Water Environment Research, 86(10), pp. 2132-2155. doi:10.2175/106143014x13975035526185

Liu, X., Li, W., Li, L., Yang, Y., Mao, L., & Peng, Z. 2014. A label-free electrochemical immunosensor based on gold nanoparticles for direct detection of atrazine. Sensors and Actuators B: Chemical, 191, pp. 408-414. doi:10.1016/j.snb.2013.10.033

Mashuni, Ramadhan, L. O. A. N., Jahiding, M., & Herniati, 2016. Analysis of diazinon pesticide using potentiometric biosensor based on enzyme immobilized cellulose acetate membrane in gold electrode. IOP Conference Series: Materials Science and Engineering, 107, p. 12013. doi:10.1088/1757-899x/107/1/012013

Melo, L. C., Julião, M. S. S., Milhome, M. A. L., do Nascimento, R. F., De, S. D., de Lima-Neto, P., & Correia, A. N. 2018. Square Wave Adsorptive Stripping Voltammetry Determination of Chlorpyriphos in Irrigation Agricultural Water. Journal of Analytical Chemistry, 73(7), pp. 695-704. doi:10.1134/s1061934818070109

Mogha, N. K., Sahu, V., Sharma, M., Sharma, R. K., & Masram, D. T. 2016. Biocompatible ZrO 2 - reduced graphene oxide immobilized AChE biosensor for chlorpyrifos detection. Materials & Design, 111, pp. 312-320. doi:10.1016/j.matdes.2016.09.019

Mostafa, G. 2010. Electrochemical Biosensors for the Detection of Pesticides. The Open Electrochemistry Journal, 2(1), pp. 22-42. doi:10.2174/1876505x01002010022

Navaratne, A., & Priyanth, N. 2011. Chemically Modified Electrodes for Detection of Pesticides. In M. Stoytcheva Ed., Pesticides in the Modern World - Trends in Pesticides Analysis.IntechOpen. doi:10.5772/17320

Ni, Y., Qiu, P., & Kokot, S. 2005. Simultaneous voltammetric determination of four carbamate pesticides with the use of chemometrics. Analytica Chimica Acta, 537(1-2), pp. 321-330. doi:10.1016/j.aca.2004.12.080

Oliveira, T. M. B. F., Barroso, M. F., Morais, S., Araujo, M., Freire, C., Lima-Neto, P., Correia, A.N., Oliveira, M. B. P. P., & Delerue-Matos, C. 2014. Sensitive bi-enzymatic biosensor based on polyphenoloxidases–gold nanoparticles–chitosan hybrid film–graphene doped carbon paste electrode

for carbamates detection. Bioelectrochemistry, 98, pp. 20-29. doi:10.1016/j.bioelechem.2014.02.003

-Population Division Department of Economic and Social Affairs United Nations Secretariat. . The World at Six Billion. http://mysite.du.edu/~rkuhn/ints4465/world-at-six-billion.pdf.

Pop, A., Manea, F., Flueras, A., & Schoonman, J. 2017. Simultaneous Voltammetric Detection of Carbaryl and Paraquat Pesticides on Graphene-Modified Boron-Doped Diamond Electrode. Sensors, 17(9), p. 2033. doi:10.3390/s17092033

Reddy, P. P., Ofamaja, A. E., Reddy, C. N., & Naido, E. B. 2016. Square Wave Voltammetric Detection of Dimethylvinphos and Naftalofos in Food and Environmental Samples Using RGO/CS modified Glassy Carbon Electrode. Int. J. Electrochem. Sci, 11, pp. 65-79.

Ribeiro, F. W. P., Barroso, M. F., Morais, S., Viswanathan, S., Lima-Neto, P., Correia, A. N., Oliveira, M. B. P. P., & Delerue-Matos, C. 2014. Simple laccase-based biosensor for formetanate hydrochloride quantification in fruits. Bioelectrochemistry, 95, pp. 7-14. doi:10.1016/j.bioelechem.2013.09.005

Sanford, C., Sabapathy, D., Morrison, H., & Gaudreau, K. 2015. Systematic Review. In Pesticides and human health. Prince Edward Island, Canada. Part 1.

Sanghavi, B. J., Wolfbeis, O. S., Hirsch, T., & Swami, N. S. 2015. Nanomaterial-based electrochemical sensing of neurological drugs and neurotransmitters. Microchimica Acta, 182(1-2), pp. 1-41. doi:10.1007/s00604-014-1308-4

Sani, R. K., Bagri, L. P., & Bajpai, A. K. 2017. New Pesticides and Soil Sensors. Netherlands: Elsevier. chapter 14.

Sassolas, A., Prieto-Simón, B., & Marty, J. 2012. Biosensors for Pesticide Detection: New Trends. American Journal of Analytical Chemistry, 03(03), pp. 210-232. doi:10.4236/ajac.2012.33030

Selva, T. M. G., Araujo, W. R., & Paixao, T. R. L. C. 2017. Electrochemical sensor for discrimination of carbamates and organophosphorus pesticides. In 2017 ISOCS/IEEE International Symposium on Olfaction and Electronic Nose (ISOEN).Institute of Electrical and Electronics Engineers (IEEE), pp. 1-3. doi:10.1109/isoen.2017.7968922

Shahtaheri, S. J., Faridbod, F., & Khadem, M. 2017. Highly Selective Voltammetric Sensor Based on Molecularly Imprinted Polymer and Carbon Nanotubes to Determine the Dicloran Pesticide in Biological and Environmental Samples. Procedia Technology, 27, pp. 96-97. doi:10.1016/j.protcy.2017.04.041

Skoog, D. A., Holler, F. J., & Nieman, A. T. 1997. Principles of instrumental analysis. Unite States of America: Books/Cole. fifth edition.

Talan, A., Mishra, A., Eremin, S. A., Narang, J., Kumar, A., & Gandhi, S. 2018. Ultrasensitive electrochemical immuno-sensing platform based on gold nanoparticles triggering chlorpyrifos detection in fruits and vegetables. Biosensors and Bioelectronics, 105, pp. 14-21. doi:10.1016/j.bios.2018.01.013

CHEMISTRY

Tago, D., Andersson, H., & Treich, N. 2014. Pesticides and Health: A Review of Evidence on Health Effects, Valuation of Risks, and Benefit-Cost Analysis. In G. C. Blomquist& K. Bolin Eds., Adv Health Econ Health Serv Res.Emerald., pp. 203-295. doi:10.1108/s0731-2199_2014_0000024006

Tang, J., & Tang, D. 2015. Non-enzymatic electrochemical immunoassay using noble metal nanoparticles: a review. Microchimica Acta, 182(13-14), pp. 2077-2089. doi:10.1007/s00604-015-1567-8

Teadoum, D. N., Noumbo, S. K., Arnaud, K. T., Ranil, T. T., Mvondo, Z. A. D., & Tonle, I.K. 2016. Square Wave Voltammetric Determination of Residues of Carbendazim Using a Fullerene/Multiwalled Carbon Nanotubes/Nafion//Coated Glassy Carbon Electrode. International Journal of Electrochemistry, 2016, pp. 1-9. doi:10.1155/2016/7839708

Thota, R., & Ganesh, V. 2016. Selective and sensitive electrochemical detection of methyl parathion using chemically modified overhead projector sheets as flexible electrodes. Sensors and Actuators B: Chemical, 227, pp. 169-177. doi:10.1016/j.snb.2015.12.008

Tonle, I., & Ngameni, E. 2011. Voltammetric Analysis of Pesticides. In M. Stoytcheva Ed., Pesticides in the Modern World - Trends in Pesticides Analysis.IntechOpen. doi:10.5772/18623

Uslu, B., & Ozkan, S. 2007. Electroanalytical Application of Carbon Based Electrodes to the Pharmaceuticals. Analytical Letters, 40(5), pp. 817-853. doi:10.1080/00032710701242121

Vukojević, V., Djurdjić, S., Jevtić, S., Pergal, M., Marković, A., Mutić, J., Petković, B. B. & Stanković D. M. 2018. First electrochemical investigation of organophosphorus pesticide azametiphos and its quantification using electroanalytical approach. International Journal of Environmental Analytical Chemistry, 98(13), pp. 1175-1185. doi:10.1080/03067319.2018.1537394

Xu, F., Cui, Z., Li, H., & Luo, Y. 2017. Electrochemical determination of trace pesticide residues based on multiwalled carbon nanotube grafted acryloyloxy ferrocene carboxylates with different spacers. RSC Advances, 7(12), pp. 7431-7441. doi:10.1039/c6ra26436k

Xu, G., Huo, D., Hou, C., Zhao, Y., Bao, J., Yang, M., & Fa, H. 2018. A regenerative and selective electrochemical aptasensor based on copper oxide nanoflowers-single walled carbon nanotubes nanocomposite for chlorpyrifos detection. Talanta, 178, pp. 1046-1052. doi:10.1016/j.talanta.2017.08.086

Yang, J., Wang, Q., Zhang, M., Zhang, S., & Zhang, L. 2015. An electrochemical fungicide pyrimethanil sensor based on carbon nanotubes/ionic-liquid construction modified electrode. Food Chemistry, 187, pp. 1-6. doi:10.1016/j.foodchem.2015.04.009

Yao, Y., Zhang, L., Xu, J., Wang, X., Duan, X., & Wen, Y. 2014. Rapid and sensitive stripping voltammetric analysis of methyl parathion in vegetable samples at carboxylic acid-functionalized SWCNTs–β-cyclodextrin modified electrode. Journal of Electroanalytical Chemistry, 713, pp. 1-8. doi:10.1016/j.jelechem.2013.11.024

Zeng, Y., Zhu, Z., Du, D., & Lin, Y. 2016. Nanomaterial-based electrochemical biosensors for food safety. Journal of Electroanalytical Chemistry, 781, pp. 147-154. doi:10.1016/j.jelechem.2016.10.030

Zhang, Y., Liu, H., Yang, Z., Ji, S., Wang, J., Pang, P., Feng, L., Wang, H., Wu, Z., & Yang, W. 2015. An acetylcholinesterase inhibition biosensor based on a reduced graphene oxide/silver nanocluster/chitosan nanocomposite for detection of organophosphorus pesticides. Analytical Methods, 7(15), pp. 6213-6219. doi:10.1039/c5ay01439e

CHEMISTRY

GENERALIZATION AND CHARTOMETRIC ANALYSIS OF THE SITNICA RIVER NETWORK SYSTEM

BOJANA JANDŽIKOVIĆ[1*]

[1]Faculty of Natural Sciences and Mathematics, University of Priština, Kosovska Mitrovica, Serbia

ABSTRACT

The basin of Sitnica river represents a good option for chartometric investigation. In modern hydrology, digital and GIS analyses play very important role today. In this research we were able to obtain the main properties of the river basin and river network with the help of digital line generalization. The results from the two kind of maps with two scales 1:25.000 and 1:50.000 showed differences in length of the main river Sitnica and its tributaries. These differences may be included into the analysis of the Sitnica river network. For the first time it was concluded that the Sitnica river has bi-polar dendritic parallel network. The 80% of right tributaries have angles between 2° and 5° degrees in direction of the Sitnica river. The left tributaries have angles between 1° and 2° degrees with the main water-course.

Keywords: Sitnica, River network, Generalization, GIS, Remote Sensing, Chartometric method.

INTRODUCTION

Cartographic generalization has five main concepts. These concepts play main role, especially in the presentation in the Hydrology science. Hydrology as any other spatial science has the necessity for cartographic visualization and abstraction. The Hydrology analysis of the river network system must be used in any complete analysis of watershed. The main algorithms in the analogue generalization are classification, simplification, exaggeration, symbolization and induction (Arnhiem, 1976; Bertin, 1983).

Land waters includes rivers, water streams, lakes, swamps, etc. A river which is presented on a particular map surface joined with river systems represent the river network on a territory.

A chartometric and network analysis must contain two elements. These are length and width of the river. These data presented on the maps would be very important for cartographic generalization. For the rivers presented on the maps as lines, two kinds of generalization are very important. The first is *classification* and the second is *simplification*.

The goal of classification on the maps is to express the salient character of a distribution. Classification presents ordering and scaling as well as grouping of features according to their attributes (Douglas & Peucker, 1973; Szyperski & Murer, 2002).

Also, the classification presents an intellectual process that will group very similar features in good order. There are two common ways of performing classification on the maps. The first is allocation of similar qualitative attributes, like land use or river networks. After that quantitative attribute values may be transformed into numerically defined groups. The second is attribute value at a selected location to create a typical feature on the maps. Usually, the classification includes class interval selection and various routines. One important manipulation in this process is called clustering. Clustering is necessary when numerous discrete and concrete features characterize the distribution and it reduces the map scale for more than 50%. The simplification must reduce the amount of information to the map ability and legibility (Court, 1966). The essential geographical characteristics of the mapped phenomena will be presented to show hydrology properties.

The map space available to portray selected features is a functional scale. The map scale, i.e. ratio must be reduced by the square of the difference in linear scale. The reducing of scale by one-half, rather than three-halves reduces the map area to one-quarter. For example, a territory mapped at 1:50.000 scale will only occupy one-fourth of a map space when mapped at 1:100.000. But, the most important law for cartographic line generalization is called Topfer Radiallaw (Topfer & Pilliwizer, 1996). On applying this radical law, it is possible to determine the number of items to be expected on the new complied map. For the purpose of this research we used this law and GIS chartometric analysis in hope of better understanding the Sitnica drainage river network. Upon establishing the Topfer law, it is possible to expect the following algorithms and procedures on the map. We then have generalized sets, such as 1-point features sets; 2-linear features sets; 3-area features sets (Mackaness & Edwards, 2002; Kraak & Ormeling, 1996; Petere, 2001; Robinson, 1995).

This radical Topfer law may be implemented into GIS software. The Sitnica rivers flows in the central part of Kosovo. The Sitnica river system occupies the area of 2861 km2. This river system covers 26% of the Kosovo and Metohija territory or 35% of the basin of river Ibar. With its tributaries included, the Sitnica river system covers 22.6% of the Ibar river system. One of the leading hydrologists Plana claims that the Sitnica springs directly from the river Toplica, and the hydrologist Labus thinks that the Sitnica emerges at the village of Robovac from two

---

GEOGRAPHY, GEOSCIENCE AND ASTRONOMY

streams, Sazlija its right tributary, and Stimljanka its left tributary (Labus, 1974; Ivanović et al., 2016). After total chartometric and GIS numerical analysis we derived precise network drainage system of the river Sitnica.

MATERIALS AND METHODS

GIS multi-criteria analysis

After determing physical and hydrological charateristics of the river Sitnica basin, we went on to determine the chartometric and drainage network properties (Valjarević et al., 2013). In this investigation we used two kinds of GIS softwares. These softwares are QGIS (Quantum Geographical Information System) and SAGA (System for Automated Geoscientific Analyses).

By using these softwares we have the possibility for georeferencing, digitizing and vectorizing all attributes of the elements of the river. QGIS has the possibility of printing these images on a single sheet of paper in many different formats. The concrete advantage is that QGIS is capable of characterizing and integrating vector and raster data (Harrie & Weibel, 2007). The software is also capable of creating phase digitalization and vector data. The other tools of the software are supported and generated later in database. The digitally supported generalization has certain advantages in comparison with analogue generalization. The main advantage is in very precise segmental processing algorithms of line river generalization. The final database is presented in two kinds of codes ASCII and PostGIS. We used 16 sheets of the topographic maps in scale 1:25.000. These maps are labeled as Podujevo, Pristina, Kosovska Mitrovica. Software QGIS 2.18.4 was used for digitizing and vectorising maps with two scales 1:25.000 and 1:50.000. Another software SAGA used in this research will be excellent in the estimation of DEM (Digital Elevation Model) and calculating of a watershed. In this software, in order to calculate river network, it is necessary to use the procedures as follows. The first is the method of downloading data from the satellites. In this research Aster global DEM with resolution of 30 m was used. Today, there are plenty of methods which would be useful in DEM estimation, segregation and calculations (Valjarević et al., 2018a; Abrams, 2010; Schneider et al., 2014; Valjarević et al., 2018b). The analysis of relief conducted by special DEM calculations may be applied onto many areas of geospatial sciences (Milanović et al., 2017; Lukić et al., 2009).

SPECIAL METHODS IN THE RESEARCH

Topfer's Radical law

The Topfer's radical law is very important in modern GIS technologies, especially in line segmental generalization. The first equation Eq. (1) which presents the relationship between map scale and number of items on the map is:

$$n_c = n_s \sqrt{\frac{S_c}{S_s}} \qquad (1)$$

Where;

n_C-presents the number of items on a derived map with a scale fraction (ratio) of S_c,

n_c -presents the number of items on a source (original) map with a scale fraction (ratio) of S_S.

The main problem of simplification in the process of generalization is the nature of the source data. For example, features of islands or swamps are generally presented without process of exaggeration. On the other hand, items like industry objects for example, with their associated names, take up a much larger proportion of space, and may be retained. Due to everything listed before, it is necessary to introduce two uniform constant, C_e and C_i into radical law. The next Eq. 2 describes this postulate:

$$n_c = n_s C_e C_f \sqrt{\frac{S_c}{S_s}} \qquad (2)$$

C_e-presents the constant of symbolic exaggeration and has three forms:

C_{e1}-presents normal symbolization or elements on the maps appearing without exaggeration.

$C_{e2} = \sqrt{\frac{S_s}{S_c}}$ presents feature of areal extent on the map, shown in outline, without exaggeration, like lakes and swamps.

$C_{e3} = \sqrt{\frac{S_c}{S_s}}$ presents symbolization involving great exaggeration of the area on the map or required on the complied map,

C_{e3} presents constant of symbolic form and also has three types:

$C_{f1} = 1.0$ presents symbols or features complied without essential change,

$C_{f2} = \frac{\omega_s}{\omega_c} \sqrt{\frac{S_s}{S_c}}$ was taken for linear symbols (rivers), which line widths on the source map ω_S and the newly derived map ω_C are the main items in generalization.

$C_{f3} = \frac{a_s}{a_c} \sqrt{\frac{S_c}{S_s}}$ presents relation for area symbols in which the areas of the symbols on the source map α_C and the newly derived map α_C are the important items in the process of generalization. The equation 2 presents the most important relation in the process and procedures of line generalization. Line generalization in our case was very accurate, since scale of the maps is 1:25.000 and 1:50.000.

GIS and calculation of data and their modelling in combination with algorithms of line generalization are very powerful tools for calculating properties of a river drainage network and network basin (Wu & Chen, 2016). The river basin of the river Sitnica presents one interesting territory for GIS analysis and calculations. The raster data with a very precise resolution of 30 m, were downloaded and converted into universal projection UTM as well as WGS84 ellipsoid. With the help of two types of software QGIS and SAGA we also determined the properties of watershed and river drainage network. In analyzing the Sitnica river basin, we used printed topographic maps from different periods (1953, 1977, and 1987) with the two scales (1:25.000; 1:50.000). After digitization and vectorization, we obtained digitized maps. In this process of digitization, we used the open-source software QGIS and SAGA. High-resolution data from 2013, with a grid of 10 x 10 pixels at 30 m resolution, were downloaded from USGS (United States Geological Survey) and from the official web page Earth Explorer – LAND SAT (http://earthexplorer.usgs.gov/). GIS analysis in combination with numerical methods is very powerful tool for calculating drainage network properties. The process of DEM and basic relief analysis in an area provides letter manipulation in GIS software. Although there are many other methods, the priority is given to 3D modelling and watershed analysis (Valjarević et al., 2018c).

RESULTS

The drainage system of the Sitnica river shows the following characteristics. The south-east basin has an average slope of 7.8°, the north-east has 4.4°, whereas the south part has 4.3°. The minimum altitude in the basin is 159 m, the maximum is 1767 m. The average altitude is 480 m. The total number of tributaries according to the scale of 1:25.000 is 92, and according to a scale of 1:50.000, it is 91. Some of the biggest tributaries in the Sitinica river network are the Drenica with 41.1 km of length in scale 1:25.000, in scale 1:50.000 is 41.0 km, the Vrbica length in scale 1:25.000 is 24.1 and in scale 1:50.000 is 25.0. The Žegovka with length of 22.3 km in scale 1:25.000 and with length of 23.0 km in scale 1:50.000. The Prištevka with length of 19.9 km in scale 1:25.000 and with length of 20.0 km in scale 1:50.000. The Janjevka with length of 16.0 km in scale 1:50.000 and 16.5 km in scale 1:25.000. The Gračanka 17.0 km of length in scale 1:50.000 and 16.9 km of length in scale 1:25.000. The Prištevka with length of 20.0 km in scale 1:50.000 with length of 19.9 km. The Lab with length in scale 1:25.000 of 57.0 km and with length of 59.1 km in scale 1:50.000. The Batlava with length of 20 km in scale 1:25.000 and with length of 20.2 in scale 1:50.000. The Dubnička with length of 24.0 km in scale 1:25.000 and with length of 22.1 km in scale 1:50.000. The Bredaška with length of 14 km in scale 1:25.000 and with length

of 14,4 km. The Kačandolska with length of 30.0 km in scale 1:25.000 and with length of 29.1 km in scale 1:50.000. The Crvena with length of 15.0 km in scale 1:25.000 and with length of 15.9 km in scale 1:50.000. The Slatina with length of 10 km in scale 1:25.000 and with length of 10.6 km in scale 1:50.000. The Margulska with length of 17.0 km in scale 1:25.000 and with length of 17.5 km in scale 1:50.000. After chartometric method supported with GIS and remote sensing analysis we concluded that 70% of the rivers in the Sitnica network are right tributaries and 30% are left tributaries (Figure 1). The errors in the segmental line digital generalization are presented in the (Table 1). The 80% of right tributaries have angles between 2° and 5° degrees in direction with the Sitnica river. The left tributaries have angles between 1° and 2° degrees with the main water-course.

Table 1. The Sitnica river network, presenting some of its rivers with included error of generalization in %.

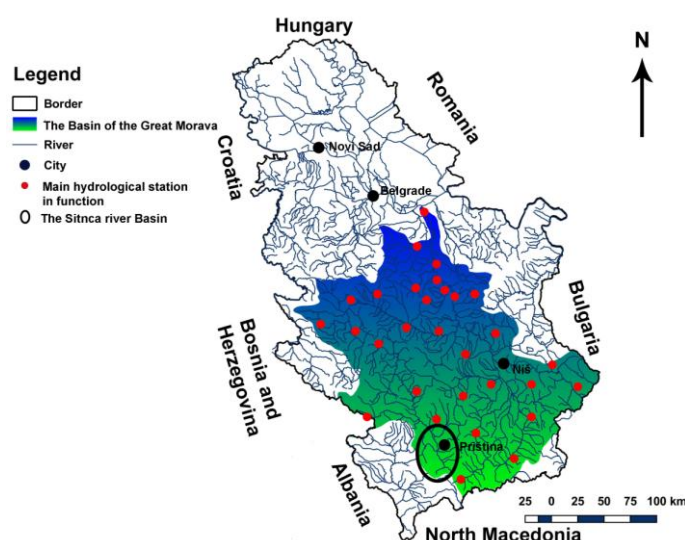| Name	Position of tributary	1:25.000	1:50.000
Drenica	Left	0.5%	0.9%
Vrbica	Right	0.4%	0.8%
Žegovka	Right	0.3%	0.7%
Prištevka	Right	0.4%	0.9%
Crvena	Right	0.2%	0.8%
Grčanka	Right	0.5%	1.0%
Batlava	Left	0.3%	0.8%
Dubnička	Left	0.2%	0.9%
Bradeška	Left	0.2%	0.8%
Kačandolska	Right	0.4%	0.9%
Slatina	Left	0.5%	1.0%

Figure 1. The basin of Sitnica river and the river network of Serbia.

According to the results from the Table 1, we concluded that rivers with meanders have higher volume of line

generalization a Rivers with five or less meanders have smaller volume of line generalization, being less than 0.5% (Figure 2).
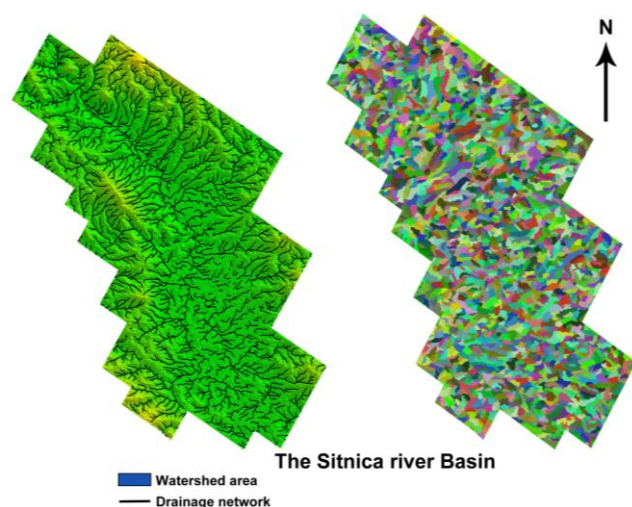

Figure 2. Generalized Sitnica river basin with drainage network and watershed areas.

CONCLUSION

With the help of two types of software, QGIS and SAGA results of line generalization were satisfactory. The line generalization supported by GIS and remote sensing methods gave very interesting results in hydrological research The river basin and the river network present two most important features of a river's hydrography. In this research, we used the Sitnica river basin, because of its interesting geographical position, separating two main parts of Kosovo. The river Sitnica presents the part of small Kosovo. Line generalization with chartometric methods in this research led to some conclusions. The first is: When we have doubled scale, the generalization grows for 5%. The error in generalization at two scales 1:25.000 and 1:50.000, at the length of 1 km of the Sitnica was 0.02%, and 0.05 % respectively. The rivers with five or more meanders have higher volume of generalization on digital and analogue maps. After total GIS and chartometric analysis we came to a conclusion that the Sitnica river has bi-polar dendritic drainage patterns and parallel network.

ACKNOWLEGMENTS

REFERENCES

Abrams, M. 2000. The Advanced Spaceborne Thermal Emission and Reflection Radiometer (ASTER): Data products for the high spatial resolution imager on NASA's Terra platform. International Journal of Remote Sensing, 21(5), pp. 847-859. doi:10.1080/014311600210326

Arnheim, R. 1976. The Perception of Maps. The American Cartographer, 3(1), pp. 5-10. doi:10.1559/152304076784080276

Bertin, J. 1983. Semiology of Graphics: Diagrams, Networks, Maps. University of Wisconsin Press.

Brunner, F. 1997. Continuous Monitoring of Deformations using the Global Positioning System. AvH-Magazine, 69.

Court, A. 1966. The Inter-Neighbor Interval. Yearbook of the Association of Pacific Coast Geographers, 28(1), pp. 180-182. doi:10.1353/pcg.1966.0005

Douglas, D., & Peucker, T. 1973. Algorithms for the Reduction of the Number of Points Required to Represent a Digitized Line or its Caricature. Canadian Cartography, 10, pp. 111-122.

Harrie, L., & Weibel, R. 2007. Modelling the Overall Process of Generalisation. In W. A. Mackaness, A. Ruas, & L. T. Sarjakoski Eds., Generalisation of Geographic Information.Elsevier BV., pp. 67-87. doi:10.1016/b978-008045374-3/50006-5

Ivanović, R., Valjarević, A., Vukoičić, D., & Radovanović, D. 2016. Climatic regions of Kosovo and Metohija. The University Thought - Publication in Natural Sciences, 6(1), pp. 49-54. doi:10.5937/univtho6-10409

Jun, C., Ban, Y., & Li, S. 2014. China: Open access to Earth land-cover map. Nature, 514(7523), pp. 434-434. doi:10.1038/514434c

Kraak, M. J., & Ormeling, F. J. 1996. Cartography: Visualization of spatial data. London: Longman.

Labus, D. 1974. Hydrological regions in Kosovo. In Collecting paper of the University of Pristina. Pristina. pp. 123-140.

Lukić, T., Marković, S. B., Stevens, T., Vasiljević, D. A., Machalett, B., Milojković, N., Basarin, B., & Obreht, I. 2009. The Loess "Cave" Near the Village of Surduk: An Unusual Pseudokarst Landform in the Loess of Vojvodina, Serbia. Acta Carsologica, 38(2-3). doi:10.3986/ac.v38i2-3.124

Mackaness, W., & Edwards, G. 2002. The Importance of The Modelling Pattern and Structure in Automated Map Generalization. In Proceeding of the Joint Workshop on Multi-Scale Representations of Spatial Data. Ottawa. pp. 1243-1249.

Milanović, M., Tomić, M., Perović, V., Radovanović, M., Mukherjee, S., Jakšić, D., Petrović, M., & Radovanović, A. 2017. Land degradation analysis of mine-impacted zone of Kolubara in Serbia. Environmental Earth Sciences, 76(16). doi:10.1007/s12665-017-6896-y

Petere, B. 2001. Measure for the Generalization of Polygonal Maps with Categorical Data. In Fourth ICA Workshop on Progress in Automated Map Generalization, Bejing.

Robinson, H. A. 1995. Elements of Cartography.New York: John Wiley and Sons, Inc.

Schneider, U., Becker, A., Finger, P., Meyer-Christoffer, A., Ziese, M., & Rudolf, B. 2014. GPCC's new land surface precipitation climatology based on quality-controlled in situ data and its role in quantifying the global water cycle. Theoretical and Applied Climatology, 115(1-2), pp. 15-40. doi:10.1007/s00704-013-0860-x

Szyperski, C., & Murer, D. 2002. Component Software.Addison Waslay. pp. 123-129; 2nd Edition.

Topfer, F., & Pilliwizer, W. 1996. The Principles of Selections. Cartography Journal, 3, pp. 10-16.

Valjarević, A., Živković, D., & Stevanović, V. 2013. Comparison of an analogue and computer supported line generalisation following the concrete example of the Sitnica River system. Scientific Research and Essays, 8(34), pp. 637-1648. doi:10.5897/sre11.1804

Valjarević, A., Srećković-Batoćanin, D., Valjarević, D., & Matović, V. 2018a. A GIS-based method for analysis of a better utilization of thermal-mineral springs in the municipality of Kursumlija (Serbia). Renewable and Sustainable Energy Reviews, 92, pp. 948-957. doi:10.1016/j.rser.2018.05.005

Valjarević, A., Djekić, T., Stevanović, V., Ivanović, R., & Jandziković, B. 2018b. GIS numerical and remote sensing analyses of forest changes in the Toplica region for the period of 1953–2013. Applied Geography, 92, pp. 131-139. doi:10.1016/j.apgeog.2018.01.016

Valjarević, A., & Živković, D. 2018c. Digital topographic modelling in case with higher flood in the municipality Obrenovac. The University Thought - Publication in Natural Sciences, 8(2), pp. 44-48. doi:10.5937/univtho8-18679

Wu, S., & Chen, Y. 2016. Examining eco-environmental changes at major recreational sites in Kenting National Park in Taiwan by integrating SPOT satellite images and NDVI. Tourism Management, 57, pp. 23-36. doi:10.1016/j.tourman.2016.05.006

MAPPING OF THE ENVIRONMENT USING MULTISPECTRAL SATELLITE IMAGERY

IVAN POTIĆ[1*], VANJA ŠIMUNIĆ[2]

[1]Republic Geodetic Authority, Belgrade, Serbia
[2]Faculty of Forestry, Belgrade, Serbia

ABSTRACT

Continuous environmental mapping has never been more necessary because of the fast-paced lifestyle, technology development, climate change. Monitoring changes in the environment has become one of the most important tasks todayto understand those changes and take the necessary measures to coordinate sustainable development with the emerging natural and socio-economic events. Remote sensing combined with cartography gives us the opportunity to obtain current information on the state of the environment and react suitablyin order to reduce damage to a minimum in accordance with sustainable development.

Keywords: Environment Monitoring, Supervised classification, Land Cover, Landsat 8, Town Bor.

INTRODUCTION

Classifying and interpreting satellite imagery is one of the remote sensing main tasks. This is most commonly used to analyze multispectral satellite imagery, which is presented bypixel classification from animagery into a spectral class, representing classification.

There are two types of classification: supervised and unsupervised classification. As stated by Richards, 1993 supervised classification is the primary method of obtaining quantitative data from multispectral satellite imagery. To use this method, it is necessary to know the part of the area being analyzed to obtain from these "known" pixels enough data to classify the other parts of the area being monitored. This step is called "training". Once trained, the "classifier" then classifies the entire imagery (area) by the classes we have defined (Figure 1).
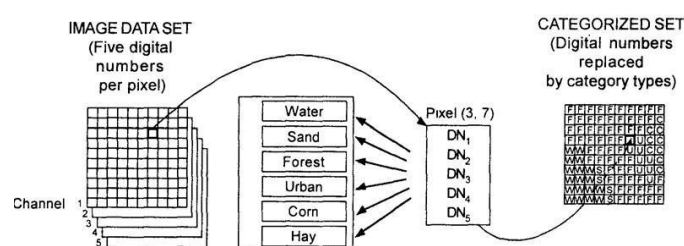

Figure 1. Supervised classification main steps.
Source: Reddy, 2008.

The most commonly used method for supervised classification is "maximum likelihood classification" (MLC). This classification uses imagery data to estimate mean and variance categories, which are used to estimate probability (Campbell, 1996).

Geospatial changes are very common in the environment. Therefore, remote sensing provides proper tool to detect environment state at given moment and map them. This is very important for afflicted areas where the environment is severely influenced by human activities, such as open mines.

Cartographic modellingis often used for presenting the state of the environment in geography and related fields. Researchers use cartographic methods to present their results which have a geospatial component, as for the changes in forest cover (Valjarević et al., 2018; Potić et al., 2017) and vegetation cover change in sensitive areas (Potić et al., 2015). In the environmental stress analysis, GIS, remote sensing and cartographic methods used for processing geospatial data is also employed to present the influence of small hydropower plants on the environment (Potić, 2018), wildfire stress analysis (Potić et al., 2017), major infrastructure projects (Potić & Potić, 2017). In the renewable energy field, different GIS and remote sensing approaches for mapping and selecting the best locations for solar power plants (Potić et al., 2016; Valjarević, 2016) and small hydropower plants (Potić, 2018; Goyal et al., 2015). Presenting the results of the GIS analysis for the climatic elements, specific climatic indices and field research data is also convenient to employ cartographic modelling (Ivanović et al., 2016). Remote sensing and GIS also have notable role in research related to the impact of high-rise buildings on generating heat islands (Đorđević et al., 2019).

For the multispectral analysis, the area near the town of Bor, located in northeastern Serbia, in the Timok region, Borska River valleywas selected. The altitude of the city is 360 m. The landscape is dominated by large open mines, factory chimneys and surrounded by the southern Carpathian Mountains and Borsko Lake (Stanković, 2001) (Figure 2).

The natural environment of the town of Bor primarily consists of forests with 37.1%, while the economy is based on mining and metallurgy. Despite the large forests area, environmental pollution is high. Significant economic and social problems are reflected in economy diversification, unemploymentand other problems, while the solution is seen in

*Corresponding author: ipotic@gmail.com

GEOGRAPHY, GEOSCIENCE AND ASTRONOMY

gaining new perspectives on tourism development,agricultural production, mining and development of small and medium-sized enterprises, wood processing industry, forestry (Strategic Plan for Social Policy of the City of Bor for the Period 2019–2023, 2018).

Figure 2. Area of interest.

EXPERIMENTAL

Materials and methods

Landsat 8 multispectral imagery recorded on the August 2013 were used for this research. The main features of the mission and the imagery are described as follows.

Landsat 8 consists of two instruments: an OLI (operational land imager) sensor that is similar to the Landsat 7 ETM + sensor (Figure 3), with the addition of two new spectral channels, a Coastal aerosol visible band (Band 1), which can be used to detect water and coastal terrain and a new infrared band Cirrus (Band 9) for detecting cirrus clouds. The TIRSsensor (Thermal Infrared Sensor)is used to collect data in two spectral channels of 10.6-11.9 and 11.5-12.51μm wavelengths (Table 1, Figure 3).

Table 1. Landsat 8 Operational Land Imager (OLI) and Thermal Infrared Sensor (TIRS) (Launched February 11, 2013).

Bands	Wavelength (micrometers)	Resolution (meters)
Band 1 - Coastal aerosol	0.43 - 0.45	30
Band 2 – Blue	0.45 - 0.51	30
Band 3 – Green	0.53 - 0.59	30
Band 4 – Red	0.64 - 0.67	30
Band 5 - Near Infrared (NIR)	0.85 - 0.88	30
Band 6 - SWIR 1	1.57 - 1.65	30
Band 7 - SWIR 2	2.11 - 2.29	30
Band 8 – Panchromatic	0.50 - 0.68	15
Band 9 – Cirrus	1.36 - 1.38	30
Band 10 - Thermal Infrared (TIRS) 1	10.60 - 11.19	100
Band 11 - Thermal Infrared (TIRS) 2	11.50 - 12.51	100

Source: Landsat 8 (L8) Data Users Handbook, Version 5.0, 2019.

The novelty in Landsat 8 satellite systemis the Quality Assessment Band (QA) which reduces the impact of reflections

and anomalies and provides more accurate data for scientific researchand compared to older radiometric resolution of Landsat sensors, Landsat 8 bands are 16bit (Landsat 8 (L8) Data Users Handbook, 2019).
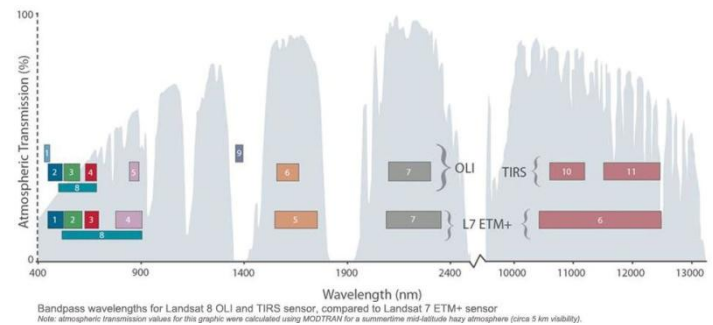
Figure 3. Landsat 8 and Landsat 7 multispectral bands. Source: Landsat 8 (L8) Data Users Handbook, 2019.

Three bands from the visible part of the spectrum (Blue, Green and Red) and one from the infrared part of the spectrum (near infrared) were selected for the supervised classification process in open source QGIS software.

MLC takes advantage of the mean vectors and multivariate propagation of each class and canidentify these extended classes (Liu, -). However, the effect of MLC depends on accurate estimation of the mean vector m and the covariance matrix for each spectral class (Richards, 1993). When the classes are multimodally distributed then we get the wrong results, and it is adopted that an indefinite distribution of classes is made in the multivariate space (Liu, -).

The maximum Gaussian probability classifier quantifies the spectral pattern when classifying an unknown pixel. It calculates the statistical probability that a given pixel belongs to a particular class (Milanović & Lješević, 2009).

The following steps are characteristic formaximum likelihood classification algorithm(Liu, -) (Figure 1):

a. Determination and display of required multispectral bands for land cover classification;

b. A training phase in which we identify the known classes from which the numerical values of the spectral signatures are obtained for each class in the scene;

c. The phase of determining the mean vectors and covariance matrices for the MLC classifier. These two parameters determine the properties of normal multivariate models.

d. The classification phase in which each pixel is categorized into the class to which it most likely belongs. Pixels that are not sufficiently similar to the classifier are marked as "unknown" (Reddy, 2008). The discriminant function *g(x)* is:

$$g(x) = -\ln\left(\left|\sum i\right|\right) - (x - mi)^t \sum i^{-1} (x - mi). \qquad (1)$$

where *mi* and Σ*i* represent the mean vector and the covariance matrix of data from the class ω*i.* To reduce misclassification,

threshold values for each *Ti* value is set based on 95% of the pixel's values being classified.Threshold values can be obtainedusing formulae 2:

$$Ti = -12.6 - \ln\left(\left|\sum i\right|\right). \qquad (2)$$

The final MLC agorithm is :

$$x \in \omega i, \text{ if } gi(x) > gj(x) \text{ and } gi(x) > Ti \text{ for all } j \neq i. \qquad (3)$$

Pixels that do not meet condition (3) are classified as "unknown" (Liu, -).

*e.*The last step is the processing and presentation of the obtained results.

Classification process started determining 7 classes to be extracted from the Landsat 8 imagery:

1) Water
2) Polluted water
3) Forest
4) Agriculture
5) Pastures and low vegetation
6) Open pit and tailings
7) Urban area

Training zones are digitized using selected pan-sharpened (15m) Landsat 8 imagery for large areas (where the areas are large enough so the training zone can be accurately digitized e.g. forest area, large water area, urban area).For zones where the boundaries are unclearly defined satellite and aerial orthophotos with high spatial resolution (Google Earth and Bing Maps 0.4 – 0.6m satellite orthophotos (Bing maps, 2013; Google, 2013)) were used (Figure 4).

Figure 4. Training zone sample for the class Agriculture.
Source: Bing maps, 2013.

After training zone selection, software calculates statistics for each class using selected algorithm (figures 5 and 6).

Univariate				
Layer	Minimum	Maximum	Mean	Std. Dev.
1	7746.000	9366.000	8341.109	233.855
2	7002.000	9285.000	7819.911	319.804
3	6402.000	9949.000	7711.183	507.605
4	7699.000	15485.000	10776.698	1028.297

Covariance				
Layer	1	2	3	4
1	54688.357	71992.925	115323.933	7973.490
2	71992.925	102274.525	155898.410	74504.012
3	115323.933	155898.410	257662.825	-6944.757
4	7973.490	74504.012	-6944.757	1057395.588

Figure 5. Agriculture training zones statistics.

Class #	>	Signature Name	Color	Red	Green ▼	Blue	Value	Order	Count	Prob
1	▶	Agriculture		0.285	0.666	0.602	12	12	3628	1.0
2		Pastures and low vegetation		0.606	0.616	0.598	15	26	984	1.0
3		Urban area		0.438	0.864	0.846	7	33	1812	1.0
4		Water		0.000	0.149	0.104	5	39	311	1.0
5		Polluted water		0.000	0.470	0.932	5	44	424	1.0
6		Open pit and tailings		0.477	1.000	1.000	13	53	2192	1.0
7		Forest		0.809	0.328	0.374	13	60	5059	1.0

Figure 6. Signature editor classes from training zones.

Using above mentioned data, algorithm classifies image pixels into the given classes.

RESULTS

Final MLC algorithm result can be cartographically presented as a map of the area at a given moment, showing the state of the environment.

In this case, the class *Urban area*containsroads that extend along the studied area, as well as bare rocks for which there is no separate class as for the roads, which can be seen in the north and northeast part of the area. *Water* and *polluted water* classes, as well as the *forest* and *open pitand tailings* are very well classified. The *Agriculture* class includes areas with low grass and bare soil, while a similar problem occurs in the *Pastures and Low Vegetation* class. Class overlap is one of a major problem with supervised classification. In this case, no *Unknown* class is obtained, which means that the algorithm recognized all the pixels, and that there was little overlap, but that we could not inevitably say that certain classes were precisely defined (figure 7). Depending on the quality of the training zone, we will receive better quality data.
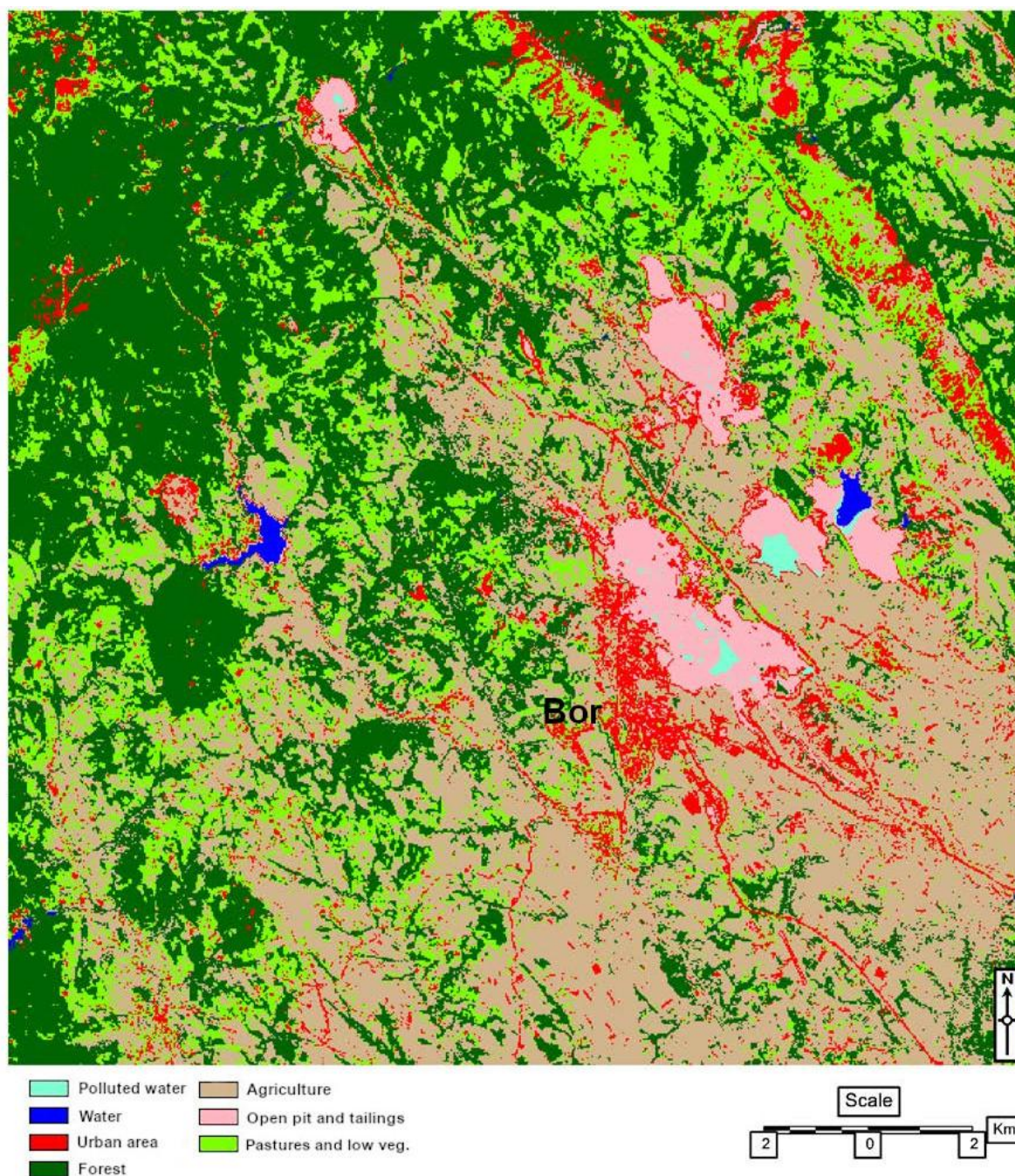
Figure 7. Research area Land Cover map.

CONCLUSION

Using the supervised multispectral analysis, we were able to obtain a land cover map of the area of interestwhich covers the town of Bor and the surrounding area, located in northeastern Serbia. From the obtained land cover map we can confirm the relative accuracy of the obtained classes, where out of 7 selected, four completely coincide with the situation on the ground, while in the three classes we have noticedmisclassified mixed pixels, which requires an increase in the number of classes and new supervised analysis iterations to obtain 10 classes that would

accurately represent the land cover of the area. Class mixing and the difference between terrain (shown in higher resolution imagery) may also be due to the small spatial resolution of 30m per pixel. Overall, the results are satisfactory and could be used to derive land cover map for which the supervised maximum likelihood classification (MLC) is designed.

Supervised classification advantages are:

- The analyst has control of training zones choice;
- The selected information category menu is specific to the region and purpose;

- This classification is usually related to specific surfaces of known classes;
- With this classification, the analyst has no problem in aligning the spectral regions (on the final map) with the interest information categories.
- An operator can detect serious errors by examining the data (to determine if they are accurately classified, which does not mean that the other classes are correct).

The disadvantages and limitations of the supervised classification are numerous. The defined categories may not be the same as in the field. Data are often defined by information categories, and only secondary to spectral properties, which can be selected by the analysts. This is used when we have large areas. The analyst may have trouble matching the data on the maps and aerial images with those classified from the imagery. This type of classification may not recognize and/or represent specific or unique categories (Mulahusić, 2007).

REFERENCES

Campbell, B. A. 1996. Introduction to Remote Sensing. In Introduction to Space Sciences and Spacecraft Applications. London: Taylor and Francis.

Đorđević, T., Potić, I. & Milanović, M. 2019. Quantification of the Impact of High-rise Buildings on Generating Heat Islands in the Area of the Realisation of the Special Purpose Plan "Belgrade Waterfront" in Belgrade. In Mihajlović, M. (Eds.), Conference proceedings International scientific conference Environmental impact of illegal construction, poor planning and design IMPEDE 2019, 10 – 11 October 2019, Belgrade, Serbia (378-387). Association of Chemists and Chemical Engineers of Serbia (UHTS), Belgrade.

Goyal, M. K., Singh, V. & Meena, A. H. 2015. Geospatial and hydrological modeling to assess hydropower potential zones and site location over rainfall dependent Inland catchment. Water Resour. Manage. 29: 2875.

Ivanović, R., Valjarević, A., Vukoičić, D., & Radovanović, D. 2016. Climatic regions of Kosovo and Metohija. The University Thought-Publication in Natural Sciences, 6(1), pp 49-54. doi:10.5937/univtho6-10409

Landsat 8 (L8) Data Users Handbook, Version 5.0 (2019). Department of the Interior, U.S. Geological Survey, EROS, Sioux Falls, South Dakota.

Liu, X. (-) Supervised classification and Unsupervised classification. Harvard: Smithsonian Center for Astrophysics. ATS 670 Class Project; Available: https://www.cfa.harvard.edu/~xliu/presentations/SRS1_project_report.PDF.

Milanović, M., & Lješević, M. 2009. Teledetekcione metode istraživanja životne sredine. Beograd: Geografski fakultet.

Mulahusić, A. 2007. Kreiranje tematskih karti na osnovu satelitskih snimaka korištenjem Maximum likelihood klasifikacije. Sarajevo: Geodetski glasnik. br. 39.

Potić, I. 2018. Geosistemska analiza višestrukih stresova životne sredine u valorizacijama lihhidro elektrana Srbije. Doctoral dissertation, University of Belgrade, Faculty of Geography.

Potić, I., & Potić, M. 2017. Remote sensing machine learning algorithms in environmental stress detection: Case study of Pan-European south section of Corridor 10 in Serbia. The University Thought-Publication in Natural Sciences, 7(2), pp. 41-46. doi:10.5937/univtho7-14957

Potić, I., Ćurčić, N., Potić, M., Radovanović, M. & Tretiakova, T. 2017. Remote sensing role in environmental stress analysis: East Serbia wildfires case study (2007–2017). Journal of the Geographical Institute "Jovan Cvijić" SASA, 67(3), pp. 249–264.

Potić, I., Golić, R. & Joksimović, T. (2016). Analysis of insolation potential of Knjaževac Municipality (Serbia) using multi-criteria approach. Renewable and Sustainable Energy Reviews, 56, pp. 235-245. doi.org/10.1016/j.rser.2015.11.056

Potić I, Joksimović M & Golić, R. 2015. Changes in vegetation cover on Staraplanina: towards sustainable management of ski resorts in sensitive areas. Bull Serb Geogr Soc 95(2), pp.25-40.

Reddy, A. 2008. Textbook of Remote Sensing and Geographical Information Systems. Hyderbad: BS Publications. Third Edition.

Richards, J. A. 1993. Remote sensing digital image analysis: An introduction. Springer-Verlag. second edition.

Stanković, S. 2001. Putevima Jugoslavije. Beograd: Zavod za udžbenike i nastavna sredstva.

Strategic Plan for Social Policy of the City of Bor for the Period 2019-2023 2018. Available: http://bor.rs/wp-content/uploads/2019/04/Strateški-plan-za-socijalnu-politiku-grada-Bora-za-period-2019-2023.pdf.

Valjarević, A., Djekić, T., Stevanović, V., Ivanović, R. & Jandziković, B. 2018. GIS numerical and remote sensing analyses of forest changes in the Toplica region for the period of 1953–2013. Applied geography, 92, pp. 131-139.

Valjarević, A. 2016. GIS modelling of solar potential in Toplica region. The University Thought-Publication in Natural Sciences, 6(1), pp. 44-48.doi:10.5937/univtho6-10739

Bing maps 2013. [Bing aerial]. Retrieved in 2013, from URL: [https://www.bing.com/maps?osid=674cd93c-5ad8-4557-a37e4ae51c5a801e&cp=44.073285~22.097064&lvl=16&v=2&sV=2&form=S00027]

Google 2013. [Google satellite]. Retrieved in 2013, from URL: [https://www.google.com/maps/@44.0693725,22.0919778,1816m/data=!3m1!1e3]

OSCILLATION CRITERIA FOR SECOND ORDER HALF-LINEAR DIFFERENTIAL EQUATIONS WITH DELAY

RADICA BOJIČIĆ[1,★], TANJA JOVANOVIĆ[2]

[1]Faculty of Ekonomy, University of Priština, Kosovska Mitrovica, Serbia
[2]Faculty of Natural Sciences and Mathematics, University of Priština, Kosovska Mitrovica, Serbia

ABSTRACT

The oscillation criteria of different types of differential equations are often the topic of numerous scientific papers, because their application in nuclear physics, fluid mechanics, relativistic mechanics, the study of chemical reactions in the system and in general are large in science. In this paper, the oscillation criteria using averaging functions of the half-linear differential equation are generalized to the half-linear differential equation with delay, under the appropriate assumptions for the delay function. Suitable examples illustrate the application of set oscillation criteria.

Keywords: Half-linear differential equations with delay, Oscillation criteria, Averaging function.

INTRODUCTION

Part of the qualitative analysis of differential equations is particularly intense in the last thirty years. During this time, new testing methods were developed and important and useful results were obtained. Probably the highest-studied differential equation of the second order is the Sturm-Liouville linear differential equation of the second order:

$$(L) \qquad [p(t)u'(t)]' + q(t)u(t) = 0$$

In the last decade of the last century, significant progress was made in determining the qualitative similarity of the solution of the equation (L) and the second-order half-linear differential equation:

$$(HL) \qquad [p(t)\Phi(u'(t))]' + q(t)\Phi(u(t)) = 0$$

where $q \in C([t_0, \infty)), p \in C^1([t_0, \infty); (0, \infty)), \Phi : \mathbb{R} \to \mathbb{R}$ defined by $\Phi(s) := |s|^{\alpha-1} s, \alpha > 0$ is a constant. Especially it is necessary to point out the articles of Mirzov (Mirzov, 1976) and Elbert (Elbert, 1979), who first established that the equations (L) and (HL) have similar properties describing the character of the oscillations solutions.

Between the large number of oscillation criteria shown using averaging functions, it can be noted that as a weight function is the most frequently used or positive, continuous differentiable function ρ, such that ρ' is a nonnegative and decreasing function, or the function $(t - s)^\alpha$ for α is a natural or real number greater than the unit, or product of these functions. Articles Philos (Philos, 1989) and Li (Li, 1995) on the oscillatory of a linear differential equation were given a positive answer to the question posed by the mathematicians who dealt with this problem - can a wider family of functions be used as a weight function?

Ten years later, J. Manojlović, who made an outstanding contribution to the whole theory of the oscillation of differential

equations, announces the paper (Manojlović, 1999) in which one step further.

In the last years of the last century, the attention of the author has attracted a second-order differential equation known as **half-linear differential equation with a delay** of form:

$$(RHL) \qquad \left[p(t)|u'(t)|^{\alpha-1}u'(t)\right]' + q(t)|u(\tau(t))|^{\alpha-1}u(\tau(t)) = 0$$

where $\alpha > 0$ is a constant, and functions $p(t), q(t), \tau(t)$ which satisfy the conditions:

$$(a) \qquad p \in C^1([t_0, \infty); [0, \infty)), \ p'(t) \geq 0, \quad \text{na} \ [t_0, \infty);$$

$$(b) \qquad q \in C([t_0, \infty); [0, \infty));$$

$$(c) \quad \tau \in C^1([t_0, \infty); [0, \infty)), \ \tau(t) \leq t, \ \text{na} \ [t_0, \infty), \ \lim_{t \to \infty} \tau(t) = \infty;$$

$$(d) \qquad \lim_{t \to \infty} \int_{t_0}^{t} p^{-\frac{1}{\alpha}}(s) \, ds = \infty.$$

By studying these equations, led to the conclusion that there is a certain qualitative similarity of its solutions and solutions of the equation (HL). The contribution to this study is given in the papers (Hsu & Yeh, 1996), (Kusano & Naito, 1997), (Kusano & Wang, 1995), (El-Sheikh & Sallam, 2000) and (Wang, 1997).

In this paper, the given oscillatory criteria using averaging functions (HL) given in the paper (Manojlović, 1999), will be generalized to the equation (RHL).

MAIN RESULTS

Given the differential equation (RHL), in which the functions p, q and τ satisfy the conditions $(a) - (d)$.

★ Corresponding author: radica.bojicic@pr.ac.rs
MATHEMATICS, COMPUTER SCIENCE AND MECHANICS

Theorem 1. *The equation* (*RHL*) *is an oscillatory if exist constant* $\lambda \in (0,1)$ *and function* $H \in \mathcal{H}^+(\mathcal{D})$ *such that it is:*

$$(\mathbb{C}_1) \qquad \lim_{t \to \infty} \frac{1}{H(t, t_0)} \cdot$$

$$\cdot \int_{t_0}^{t} \left[q(s) H(t,s) \left(\frac{\tau(s)}{s} \right)^\alpha - \frac{p(s) h^{\alpha+1}(t,s)}{\lambda (\alpha+1)^{\alpha+1} H^\alpha(t,s)} \right] ds = \infty$$

where is

$$h(t,s) = -\frac{\partial H(t,s)}{\partial s}.$$

Proof. Suppose the opposite, that there exists a nonoscillatory solution of $u(t)$ of equation (*RHL*). According to Lemma 1.1. from (Bojičić, 2015), there exists $T_0 \geqslant t_0$ such that $u(t) > 0$, $u(\tau(t)) > 0$, $u'(t) > 0 \ \wedge \ u''(t) \leqslant 0$ for $\forall t \geqslant T_0$.

We define in $[T_0, \infty)$ function w as:

$$w(t) = \frac{p(t)(u'(t))^\alpha}{u^\alpha(t)}. \qquad (1)$$

From here we have:

$$w'(t) = \frac{[p(t)(u'(t))^\alpha]'}{u^\alpha(t)} - \frac{\alpha p(t)(u'(t))^{\alpha+1}}{u^{\alpha+1}(t)}$$

$$= \frac{-q(t)(u(\tau(t)))^\alpha}{u^\alpha(t)} - \alpha p(t) \left[\frac{w(t)}{p(t)} \right]^{\frac{\alpha+1}{\alpha}}.$$

According to Lemma 1.2. (Bojičić, 2015), for every $\mu \in (0,1)$, we obtain

$$\left[\frac{u(\tau(t))}{u(t)} \right]^\alpha \geqslant \lambda \left(\frac{\tau(t)}{t} \right)^\alpha, \quad t \geqslant T_0$$

where is $\lambda = \mu^\alpha \in (0,1)$. Hence, we have

$$w'(t) \leqslant -q(t) \lambda \left(\frac{\tau(t)}{t} \right)^\alpha - \alpha \frac{w^{\frac{\alpha+1}{\alpha}}(t)}{p^{\frac{1}{\alpha}}(t)}, \quad t \geqslant T_0. \qquad (2)$$

If we multiply last inequality by $H(t,s)$, and integrate it from T to t for $T \geqslant T_0$, we get:

$$\int_{T}^{t} w'(s) H(t,s) \, ds \leqslant$$

$$-\int_{T}^{t} \lambda q(s) \left(\frac{\tau(s)}{s} \right)^\alpha H(t,s) \, ds - \int_{T}^{t} \alpha \frac{w^{\frac{\alpha+1}{\alpha}}(s)}{p^{\frac{1}{\alpha}}(s)} H(t,s) \, ds. \qquad (3)$$

Using integration by parts, we have

$$\int_{T}^{t} w'(s) H(t,s) \, ds = w(s) H(t,s) \Big|_{s=T}^{s=t} - \int_{T}^{t} w(s) \frac{\partial H(t,s)}{\partial s} ds =$$

$$= -w(T) H(t,T) + \int_{T}^{t} w(s) h(t,s) \, ds,$$

so that from equality (3) we obtain

$$\lambda \int_{T}^{t} q(s) \left(\frac{\tau(s)}{s} \right)^\alpha H(t,s) \, ds \leqslant \qquad (4)$$

$$\leqslant w(T) H(t,T) - \int_{T}^{t} w(s) h(t,s) \, ds - \alpha \int_{T}^{t} \frac{w^{\frac{\alpha+1}{\alpha}}(s)}{p^{\frac{1}{\alpha}}(s)} H(t,s) \, ds.$$

If we use a inequality Hardly, Littewood & Polya (Hardly et al., 1988) and put

$$X = [\alpha H(t,s)]^{\frac{\alpha}{\alpha+1}} \frac{w(s)}{p^{\frac{1}{\alpha+1}}(s)}$$

$$Y = \frac{\alpha^{\frac{\alpha}{\alpha+1}}}{(\alpha+1)^\alpha} \frac{p^{\frac{\alpha}{\alpha+1}}(s) h^\alpha(t,s)}{H^{\frac{\alpha^2}{\alpha+1}}(t,s)}$$

$$\gamma = \frac{\alpha+1}{\alpha} = 1 + \frac{1}{\alpha} > 1,$$

we get

$$w(s) h(t,s) - \frac{\alpha H(t,s) w^{\frac{\alpha+1}{\alpha}}(s)}{p^{\frac{1}{\alpha}}(s)} \leqslant \frac{p(s) h^{\alpha+1}(t,s)}{(\alpha+1)^{\alpha+1} H^\alpha(t,s)}, \quad t \geqslant s \geqslant T_0.$$

Therefore, for $t \geqslant T \geqslant T_0$ is valid inequality

$$\lambda \int_{T}^{t} q(s) \left(\frac{\tau(s)}{s} \right)^\alpha H(t,s) \, ds \leqslant$$

$$w(T) H(t,T) + \int_{T}^{t} \frac{p(s) h^{\alpha+1}(t,s)}{(\alpha+1)^{\alpha+1} H^\alpha(t,s)} ds. \qquad (5)$$

Since $H \in \mathcal{H}^+$, i.e. monotonically non-increasing by s, then for every $t \geqslant T_0 \geqslant t_0$

$$H(t, t_0) \geqslant H(t, T_0).$$

Therefore, from (5) we obtain

$$\lambda \int_{T_0}^{t} q(s) \left(\frac{\tau(s)}{s} \right)^\alpha H(t,s) \, ds \leqslant$$

$$w(T_0) H(t, T_0) + \int_{T_0}^{t} \frac{p(s) h^{\alpha+1}(t,s)}{(\alpha+1)^{\alpha+1} H^\alpha(t,s)} ds$$

$$\leqslant w(T_0) H(t, t_0) + \int_{t_0}^{t} \frac{p(s) h^{\alpha+1}(t,s)}{(\alpha+1)^{\alpha+1} H^\alpha(t,s)} ds,$$

whence we conclude

$$\lambda \int_{t_0}^{t} q(s) \left(\frac{\tau(s)}{s} \right)^\alpha H(t,s) \, ds =$$

$$\lambda \int_{t_0}^{T_0} q(s) \left(\frac{\tau(s)}{s} \right)^\alpha H(t,s) \, ds + \lambda \int_{T_0}^{t} q(s) \left(\frac{\tau(s)}{s} \right)^\alpha H(t,s) \, ds$$

$$\leqslant \lambda H(t, t_0) \int_{t_0}^{T_0} q(s) \left(\frac{\tau(s)}{s} \right)^\alpha ds + H(t, t_0) |w(T_0)| +$$

$$\int_{t_0}^{t} \frac{p(s) h^{\alpha+1}(t,s)}{(\alpha+1)^{\alpha+1} H^\alpha(t,s)} ds, \quad t \geqslant T_0.$$

From the last inequality it is obvious that:

$$\limsup_{t\to\infty} \frac{1}{H(t,t_0)} \int_{t_0}^{t} \left[q(s) H(t,s) \left(\frac{\tau(s)}{s} \right)^{\alpha} - \frac{p(s) h^{\alpha+1}(t,s)}{\lambda(\alpha+1)^{\alpha+1} H^{\alpha}(t,s)} \right] ds$$

$$\leqslant \int_{t_0}^{T_0} q(s) \left(\frac{\tau(s)}{s} \right)^{\alpha} ds + \frac{w(T_0)}{\lambda}.$$

According to the condition $(\mathbb{C}_1)$, we obtain a contradiction. Hence, the equation (RHL) doesn't have nonoscillatory solutions, i.e. its equation is oscillatory.

Corollary 2. *Equation (RHL) is oscillatory if exist function $H \in \mathcal{H}^{+}(\mathcal{D})$ such that hold conditions:*

$$\limsup_{t\to\infty} \frac{1}{H(t,t_0)} \int_{t_0}^{t} \frac{p(s) h^{\alpha+1}(t,s)}{H^{\alpha}(t,s)} ds < \infty$$

and

$$\limsup_{t\to\infty} \frac{1}{H(t,t_0)} \int_{t_0}^{t} q(s) \left(\frac{\tau(s)}{s} \right)^{\alpha} H(t,s) ds = \infty.$$

In order to illustrate the previously proven criteria, we consider the following example:

Example 3. Consider the differential equation:

$$(E_1) \qquad \left[t^{\gamma} |u'(t)|^{\alpha-1} u'(t) \right]' + t^{\mu} \left| u\left(\frac{t}{3} \right) \right|^{a-1} u\left(\frac{t}{3} \right) = 0$$

where is ν, α, μ are arbitrary constants that satisfy the conditions $\mu > 0$ and $0 \leqslant \nu < \alpha \neq 2$. We check the conditions of Theorem 1:

$$p(t) = t^{\gamma} > 0, \ \forall t \geqslant t_0, \nu \geqslant 0;$$

$$p'(t) = \nu t^{\gamma-1} \geqslant 0 \ \text{jer je } \nu \geqslant 0;$$

$$\int_{t_0}^{t} \frac{ds}{p^{\frac{1}{\alpha}}(s)} = \int_{t_0}^{t} \frac{ds}{s^{\frac{\gamma}{\alpha}}} = \frac{1}{1 - \frac{\nu}{\alpha}} \left. s^{1-\frac{\gamma}{\alpha}} \right|_{t_0}^{t} = \frac{\alpha}{\alpha - \nu} \left. s^{1-\frac{\gamma}{\alpha}} \right|_{t_0}^{t} \underset{t\to\infty}{\longrightarrow} \infty$$

Let $H(t,s) = (t-s)^2$ weight function. Then:

$$h(t,s) = -\frac{\partial H(t,s)}{\partial s} = 2(t-s) \geqslant 0, \ t \geqslant s \geqslant t_0$$

It remains to be determined whether the condition $(\mathbb{C}_1)$ is valid:

$$\frac{1}{t^2} \int_{t_0}^{t} \left[q(s) H(t,s) \left(\frac{\tau(s)}{s} \right)^{\alpha} - \frac{p(s) h^{\alpha+1}(t,s)}{\lambda(\alpha+1)^{\alpha+1} H^{\alpha}(t,s)} \right] ds$$

$$= \frac{1}{t^2} \int_{t_0}^{t} \left[s^{\mu} (t-s)^2 \frac{1}{3^{\alpha}} - \frac{s^{\gamma} 2^{\alpha+1} (t-s)^{\alpha+1}}{\lambda(\alpha+1)^{\alpha+1} (t-s)^{2\alpha}} \right] ds$$

$$= \frac{1}{3^{\alpha} t^2} \int_{t_0}^{t} s^{\mu} (t-s)^2 ds - \frac{2^{\alpha+1}}{t^2} \int_{t_0}^{t} s^{\gamma} (t-s)^{1-\alpha} ds$$

$$\geqslant \frac{t_0^{\mu}}{3^{\alpha} t^2} \int_{t_0}^{t} (t-t_0)^2 ds - \frac{2^{\alpha+1} t^{\gamma}}{t^2} \int_{t_0}^{t} s^{\gamma} (t-s)^{1-\alpha} ds$$

$$= \frac{t_0^{\mu}}{3^{\alpha+1} t^2} (t-t_0)^3 - \frac{2^{\alpha+1}}{t^{2-\gamma}} \frac{1}{2-\alpha} (t-t_0)^{2-\alpha}$$

$$= \frac{t_0^{\mu} t^3}{3^{\alpha+1}} \left(1 - \frac{t_0}{t} \right)^3 - \frac{2^{\alpha+1}}{2-\alpha} \frac{1}{t^{\alpha-\gamma}} \left(1 - \frac{t_0}{t} \right)^{2-\alpha} \underset{t\to\infty}{\longrightarrow} \infty,$$

where, due to the arbitrariness of constants $\lambda \in (0,1)$ we take $\lambda = \left(\frac{1}{\alpha+1} \right)^{\alpha+1}$.

Consequently, condition $(\mathbb{C}_1)$ is satisfied, hence from here follows equation (E_1) is oscillatory by Theorem 1.

Theorem 4. *Suppose there is a function $H \in \widetilde{\mathcal{H}}(D)$ such that the following condition is satisfied:*

$$(\mathbb{C}_2) \qquad \limsup_{t\to\infty} \frac{1}{H(t,t_0)} \int_{t_0}^{t} \frac{p(s) h^{\alpha+1}(t,s)}{H^{\alpha}(t,s)} ds < \infty.$$

If exist constant $\lambda \in (0,1)$ and function $\varphi \in C([t_o, \infty))$ such that:

$$(\mathbb{C}_3) \qquad \limsup_{t\to\infty} \frac{1}{H(t,T)} \cdot$$

$$\int_{T}^{t} \left[q(s) H(t,s) \left(\frac{\tau(s)}{s} \right)^{\alpha} - \frac{p(s) h^{\alpha+1}(t,s)}{\lambda(\alpha+1)^{\alpha+1} H^{\alpha}(t,s)} \right] ds \geqslant \varphi(T)$$

for every $T \geqslant t_0$ and

$$(\mathbb{C}_4) \qquad \int_{t_0}^{\infty} \frac{\varphi_+^{\frac{\alpha+1}{\alpha}}(s)}{p^{\frac{1}{\alpha}}(s)} ds = \infty,$$

then equation (RHL) is oscillatory.

Proof. We suppose that there exists a solution $u(t)$ of equation (RHL) such that $u(t) > 0$, $t \geqslant T_0$. Defining the function $w(t)$ as in the proof of Theorem 1, we get (4) and (5), for every $t \geqslant T \geqslant T_0$ Then, for (5), we have

$$\varphi(T) \leqslant \limsup_{t\to\infty} \frac{1}{H(t,T)} \cdot$$

$$\cdot \int_{T}^{t} \left[q(s) H(t,s) \left(\frac{\tau(s)}{s} \right)^{\alpha} - \frac{p(s) h^{\alpha+1}(t,s)}{\lambda(\alpha+1)^{\alpha+1} H^{\alpha}(t,s)} \right] ds \leqslant \frac{w(T)}{\lambda}$$

Therefore, it is true that:

$$\varphi(T) \leqslant \frac{w(T)}{\lambda}, \text{ for every } T \geqslant T_0. \qquad (6)$$

Now, we can conclude:

$$\limsup_{t\to\infty} \frac{1}{H(t,T_0)} \int_{T_0}^{t} q(s) H(t,s) \left(\frac{\tau(s)}{s} \right)^{\alpha} ds \geqslant \varphi(T_0). \qquad (7)$$

We define functions

$$F(t) := \frac{1}{\lambda H(t,T_0)} \int_{T_0}^{t} w(s) h(t,s) ds, \ t \geqslant T_0$$

and

$$G(t) := \frac{\alpha}{\lambda H(t, T_0)} \int_{T_0}^{t} \frac{w^{\frac{\alpha+1}{\alpha}}(s)}{p^{\frac{1}{\alpha}}(s)} H(t, s)\, ds, \quad t \geqslant T_0.$$

Then, by (4) and (7) we see that

$$\liminf_{t \to \infty} [G(t) - F(t)] \leqslant \frac{w(T_0)}{\lambda} - \tag{8}$$

$$- \limsup_{t \to \infty} \frac{1}{H(t, T_0)} \int_{T_0}^{t} q(s) H(t, s) \left(\frac{\tau(s)}{s}\right)^{\alpha} ds$$

$$\leqslant \frac{w(T_0)}{\lambda} - \varphi(T_0) < \infty.$$

It remains to be proved

$$\int_{T_0}^{\infty} \frac{|w(s)|^{\frac{\alpha+1}{\alpha}}}{p^{\frac{1}{\alpha}}(s)} ds < \infty. \tag{9}$$

If we suppose that (9) fails, there exists $T_1 > T_0$ such that

$$\int_{T_0}^{t} \frac{|w(s)|^{\frac{\alpha+1}{\alpha}}}{p^{\frac{1}{\alpha}}(s)} ds \geqslant \frac{\mu}{\alpha\xi} \quad \text{for } t \geqslant T_1, \tag{10}$$

where $\mu > 0$ is arbitrary number, and ξ is a positive constant, such that

$$\inf_{s \geqslant T_0} \left(\liminf_{t \to \infty} \frac{H(t, s)}{H(t, t_0)} \right) > \xi > 0. \tag{11}$$

Then we have

$$G(t) = \frac{\alpha}{\lambda H(t, T_0)} \int_{T_0}^{t} \frac{w^{\frac{\alpha+1}{\alpha}}(s)}{p^{\frac{1}{\alpha}}(s)} H(t, s)\, ds =$$

$$= \frac{\alpha}{\lambda H(t, T_0)} \int_{T_0}^{t} H(t, s)\, d\left(\int_{T_0}^{s} \frac{w^{\frac{\alpha+1}{\alpha}}(\delta)}{p^{\frac{1}{\alpha}}(\delta)} d\delta\right) =$$

$$= \frac{\alpha}{\lambda H(t, T_0)} \left(H(t, s) \int_{T_0}^{s} \frac{w^{\frac{\alpha+1}{\alpha}}(\delta)}{p^{\frac{1}{\alpha}}(\delta)} d\delta\right)\Bigg|_{s=T_0}^{s=t} -$$

$$- \frac{\alpha}{\lambda H(t, T_0)} \int_{T_0}^{t} \frac{\partial H(t, s)}{\partial s}\left(\int_{T_0}^{s} \frac{w^{\frac{\alpha+1}{\alpha}}(\delta)}{p^{\frac{1}{\alpha}}(\delta)} d\delta\right) ds =$$

$$= -\frac{\alpha}{\lambda H(t, T_0)} \int_{T_0}^{t} \frac{\partial H(t, s)}{\partial s}\left(\int_{T_0}^{s} \frac{w^{\frac{\alpha+1}{\alpha}}(\delta)}{p^{\frac{1}{\alpha}}(\delta)} d\delta\right) ds$$

$$\geqslant -\frac{\alpha}{\lambda H(t, T_0)} \int_{T_1}^{t} \frac{\partial H(t, s)}{\partial s}\left(\int_{T_0}^{s} \frac{w^{\frac{\alpha+1}{\alpha}}(\delta)}{p^{\frac{1}{\alpha}}(\delta)} d\delta\right) ds$$

$$\geqslant -\frac{\mu}{\lambda\xi H(t, T_0)} \int_{T_1}^{t} \frac{\partial H(t, s)}{\partial s} ds = -\frac{\mu}{\lambda\xi H(t, T_0)} H(t, s)\big|_{s=T_1}^{s=t}$$

$$= \frac{\mu}{\lambda\xi} \frac{H(t, T_1)}{H(t, T_0)} = \frac{\overline{\mu}}{\xi} \frac{H(t, T_1)}{H(t, T_0)}, \quad \text{for all } t \geqslant T_1 > T_0,$$

where with $\overline{\mu}$ we denote $\overline{\mu} = \frac{\mu}{\lambda}$. By (11) there is a $T_2 \geqslant T_1$ such thate $\frac{H(t, T_1)}{H(t, T_0)} \geqslant \xi$ for all $t \geqslant T_2$, we conclude that

$$G(t) \geqslant \overline{\mu}, \quad \text{for all } t \geqslant T_2.$$

Since $\overline{\mu} = \frac{\mu}{\lambda}$, and μ is arbitrary number, we get

$$\lim_{t \to \infty} G(t) = \infty. \tag{12}$$

Consider now the number sequence $\{\sigma_n\}_{n=1}^{\infty}$ in (T_0, ∞) such that

$$\lim_{n \to \infty} \sigma_n = \infty$$

and

$$\lim_{n \to \infty} [G(\sigma_n) - F(\sigma_n)] = \liminf_{t \to \infty} [G(t) - F(t)] < \infty.$$

Then, there exists a constant M such that for all sufficiently large n holds:

$$G(\sigma_n) - F(\sigma_n) \leqslant M. \tag{13}$$

Since (12) ensures that

$$\lim_{n \to \infty} G(\sigma_n) = \infty, \tag{14}$$

and (13) implies

$$\lim_{n \to \infty} F(\sigma_n) = \infty. \tag{15}$$

From equations (14) and (15), for sufficiently large n, we derive:

$$\frac{F(\sigma_n)}{G(\sigma_n)} - 1 \geqslant -\frac{M}{G(\sigma_n)} > -\frac{1}{2},$$

i.e. $\frac{F(\sigma_n)}{G(\sigma_n)} > 1$. Therefore, by using (15), we get:

$$\lim_{n \to \infty} \frac{F^{\alpha+1}(\sigma_n)}{G^{\alpha}(\sigma_n)} = \infty. \tag{16}$$

On the other hand, by Hölder's inequality, for every $n \in N$ we have

$$F(\sigma_n) = \frac{1}{\lambda H(\sigma_n, T_0)} \int_{T_0}^{\sigma_n} w(s) h(\sigma_n, s)\, ds =$$

$$= \frac{1}{\lambda} \int_{T_0}^{\sigma_n} \left(\frac{\alpha^{\frac{\alpha}{\alpha+1}}}{H^{\frac{\alpha}{\alpha+1}}(\sigma_n, T_0)} \frac{w(s) H^{\frac{\alpha}{\alpha+1}}(\sigma_n, s)}{p^{\frac{1}{\alpha+1}}(s)}\right) \cdot$$

$$\cdot \left(\frac{\alpha^{-\frac{\alpha}{\alpha+1}}}{H^{\frac{1}{\alpha+1}}(\sigma_n, T_0)} \frac{h(\sigma_n, s) p^{\frac{1}{\alpha+1}}(s)}{H^{\frac{\alpha}{\alpha+1}}(\sigma_n, s)}\right) ds$$

$$\leqslant \frac{1}{\lambda} \left[\frac{\alpha}{H(\sigma_n, T_0)} \int_{T_0}^{\sigma_n} \frac{w^{\frac{\alpha+1}{\alpha}}(s) H(\sigma_n, s)}{p^{\frac{1}{\alpha}}(s)} ds\right]^{\frac{\alpha}{\alpha+1}} \cdot$$

$$\cdot \left[\frac{1}{\alpha^{\alpha} H(\sigma_n, T_0)} \int_{T_0}^{\sigma_n} \frac{p(s) h^{\alpha+1}(\sigma_n, s)}{H^{\alpha}(\sigma_n, s)} ds\right]^{\frac{1}{\alpha+1}}$$

$$= \frac{1}{\lambda} \left(\frac{1}{\lambda}\right)^{-\frac{\alpha}{\alpha+1}} G^{\frac{\alpha}{\alpha+1}}(\sigma_n) \left[\frac{1}{\alpha^{\alpha} H(\sigma_n, T_0)} \int_{T_0}^{\sigma_n} \frac{p(s) h^{\alpha+1}(\sigma_n, s)}{H^{\alpha}(\sigma_n, s)} ds\right]^{\frac{1}{\alpha+1}},$$

which gives

$$\frac{F^{\alpha+1}(\sigma_n)}{G^{\alpha}(\sigma_n)} \leqslant \frac{1}{\lambda\alpha^{\alpha}H(\sigma_n,T_0)}\int\limits_{T_0}^{\sigma_n}\frac{p(s)h^{\alpha+1}(\sigma_n,s)}{H^{\alpha}(\sigma_n,s)}ds$$

$$\leqslant \frac{1}{\lambda\alpha^{\alpha}H(\sigma_n,t_0)}\int\limits_{t_0}^{\sigma_n}\frac{p(s)h^{\alpha+1}(\sigma_n,s)}{H^{\alpha}(\sigma_n,s)}ds.$$

So, because of (16), we have

$$\lim_{n\to\infty}\frac{1}{H(\sigma_n,t_0)}\int\limits_{t_0}^{\sigma_n}\frac{p(s)h^{\alpha+1}(\sigma_n,s)}{H^{\alpha}(\sigma_n,s)}ds = \infty$$

i.e.

$$\lim_{t\to\infty}\frac{1}{H(t,t_0)}\int\limits_{t_0}^{t}\frac{p(s)h^{\alpha+1}(t,s)}{H^{\alpha}(t,s)}ds = \infty,$$

and this is in contradiction with the condition ($\mathbb{C}_2$). Therefore, (9) holds. Now, from (6), we obtain

$$\int\limits_{t_0}^{\infty}\frac{\varphi_+^{\frac{\alpha+1}{\alpha}}(s)}{p^{\frac{1}{\alpha}}(s)}ds \leqslant \int\limits_{t_0}^{T_0}\frac{\varphi_+^{\frac{\alpha+1}{\alpha}}(s)}{p^{\frac{1}{\alpha}}(s)}ds + \lambda^{-\frac{\alpha+1}{\alpha}}\int\limits_{T_0}^{\infty}\frac{w^{\frac{\alpha+1}{\alpha}}(s)}{p^{\frac{1}{\alpha}}(s)}ds < \infty$$

which contradicts with the condition ($\mathbb{C}_4$). This completes the proof.

Since Theorem 4 can be applied in certain cases where it is not possible to apply Theorem 1, the two oscillatory criteria are independent of each other. One such case is described in the following example.

Example 5. Consider the differential equation

$$(E_2)\qquad \left[t^{\nu}\left|u'(t)\right|^{\alpha-1}u'(t)\right]' + \frac{(k+1)^{\alpha-1}}{t}\left|u\left(\frac{t}{3}\right)\right|^{\alpha-1}u\left(\frac{t}{3}\right) = 0$$

for $t \geqslant t_0$, where k,ν,α are constants such that $k > 0, \nu < \alpha, \alpha > 2$.

If for the weight function we take the function $H(t,s) = (t-s)^2$ and constant $\lambda = \left(\frac{1}{\alpha+1}\right)^{\alpha+1}$, we can determine that the condition ($\mathbb{C}_1$) does not apply. Indeed, for $t \geqslant t_0$, we have:

$$\frac{1}{t^2}\int\limits_{t_0}^{t}\left[q(s)H(t,s)\left(\frac{\tau(s)}{s}\right)^{\alpha} - \frac{p(\alpha)h^{\alpha+1}(t,s)}{\lambda(\alpha+1)^{\alpha+1}H^{\alpha}(t,s)}\right]ds \geqslant$$

$$\frac{1}{t^2}\int\limits_{t_0}^{t}\left[\frac{(k+s)^{\alpha-1}}{s}(t-s)^2\left(\frac{1}{3}\right)^{\alpha}\right]ds - \frac{2^{\alpha+1}}{t^2}t^{\nu}\int\limits_{t_0}^{t}(t-s)^{1-\alpha}ds \geqslant$$

$$\frac{1}{t^23^{\alpha}}\frac{(k+t_0)^{\alpha-1}}{t}\frac{(t-t_0)^3}{3} - \frac{2^{\alpha+1}}{t^2}t^{\nu}\frac{1}{2-\alpha}(t-t_0)^{2-\alpha} \geqslant$$

$$\frac{t_0^{\alpha-1}}{3^{\alpha+1}}\left(1-\frac{t_0}{t}\right)^3 - \frac{2^{\alpha+1}}{(2-\alpha)t^{\alpha-1}}\left(1-\frac{t_0}{t}\right)^{2-\alpha}\xrightarrow[t\to\infty]{}c = const < \infty.$$

Hence, condition ($\mathbb{C}_1$) is not satisfied, so we can not apply Theorem 1. We check that the conditions ($\mathbb{C}_2$), ($\mathbb{C}_3$) and ($\mathbb{C}_4$) applies: ($\mathbb{C}_2$)

$$\limsup_{t\to\infty}\frac{1}{t^2}\int\limits_{t_0}^{t}\frac{p(s)h^{\alpha+1}(t,s)}{H^{\alpha}(t,s)}ds = \limsup_{t\to\infty}\frac{1}{t^2}\int\limits_{t_0}^{t}s^{\nu}(t-s)^{1-\alpha}ds$$

$$\leqslant \limsup_{t\to\infty}\frac{t^{\nu}}{t^2(2-\alpha)}(t-t_0)^{2-\alpha}$$

$$= \limsup_{t\to\infty}\frac{1}{2-\alpha}\frac{1}{t^{\alpha-\nu}}\left(1-\frac{t_0}{t}\right)^{2-\alpha} < \infty$$

$$(\mathbb{C}_3)\quad \frac{1}{t^2}\int\limits_{T}^{t}\left[q(s)H(t,s)\left(\frac{\tau(s)}{s}\right)^{\alpha} - \frac{p(s)h^{\alpha+1}(t,s)}{\lambda(\alpha+1)^{\alpha+1}H^{\alpha}(t,s)}\right]ds$$

$$\geqslant \frac{T^{\alpha-1}}{3^{\alpha+1}} - \frac{2^{\alpha+1}}{(2-\alpha)t^{\nu}}\left(1-\frac{T}{t}\right)^{2-\alpha} \geqslant \frac{T^{\alpha-1}}{3^{\alpha+1}} = \varphi(T) > 0$$

$$(\mathbb{C}_4)\qquad \int\limits_{t_0}^{\infty}\frac{\varphi^{\frac{\alpha+1}{\alpha}}(s)}{p^{\frac{1}{\alpha}}(s)}ds =$$

$$= \int\limits_{t_0}^{\infty}\frac{s^{\frac{\alpha+1}{\alpha}(\alpha-1)}3^{\frac{\alpha+1}{\alpha}(-1-\alpha)}}{s^{\frac{\nu}{\alpha}}}ds = \frac{1}{3^{\frac{(\alpha+1)^2}{\alpha}}}\int\limits_{t_0}^{\infty}s^{\frac{\alpha^2-1}{\alpha}-\frac{\nu}{\alpha}}ds = \infty$$

for $\alpha^2 - 1 - \nu > 0$, i.e. for $\nu < \alpha^2 - 1$. Accordingly, all conditions of Theorem 2 are satisfied, and hence, equation (E_2) is oscillatory for $\nu < \min\{\alpha,\alpha^2-1\}$.

Theorem 6. *Suppose that the function* $H \in \widetilde{\mathcal{H}}(D)$ *satisfies the condtion:*

$$(\mathbb{C}_5)\qquad \limsup_{t\to\infty}\frac{1}{H(t,t_0)}\int\limits_{t_0}^{t}q(s)H(t,s)\left(\frac{\tau(s)}{s}\right)^{\alpha}ds < \infty.$$

If there exists constant $\lambda \in (0,1)$ *and function* $\varphi \in C([t_0,\infty))$ *such that hold conditions* ($\mathbb{C}_4$) *and*

$$(\mathbb{C}_6)\qquad \liminf_{t\to\infty}\frac{1}{H(t,T)}\cdot$$

$$\cdot\int\limits_{T}^{t}\left[q(s)\left(\frac{\tau(s)}{s}\right)^{\alpha}H(t,s) - \frac{p(s)h^{\alpha+1}(t,s)}{\lambda(\alpha+1)^{\alpha+1}H^{\alpha}(t,s)}\right]ds \geqslant \varphi(T)$$

for all $T \geqslant t_0$, *then equation* (RHL) *is oscillatory.*

Proof. Suppose, on the contrary, that the equation (RHL) has an nonoscillation solution $u(t)$. Without loss of generality, we assume that $u(t) > 0$ for $t \geqslant T_0$. As in the proof of Theorem 1, holds (4) and (5) for all $t \geqslant T \geqslant T_0$. If we repeat the procedure as in the proof of Theorem 4, using the condition ($\mathbb{C}_6$), we obtain (6). Then from the condition ($\mathbb{C}_5$) we have:

$$\limsup_{t\to\infty}[G(t)-F(t)] \leqslant \frac{w(T_0)}{\lambda} - \liminf_{t\to\infty}\frac{1}{H(t,T_0)}\cdot$$

$$\int\limits_{T_0}^{t}q(s)\left(\frac{\tau(s)}{s}\right)^{\alpha}H(t,s)ds \leqslant \frac{w(T_0)}{\lambda} - \varphi(T_0) < \infty$$

By ($\mathbb{C}_6$) we obtain

$$\varphi(T_0) \leqslant \liminf_{t\to\infty}\frac{1}{H(t,T_0)}\int\limits_{T_0}^{t}q(s)\left(\frac{\tau(s)}{s}\right)^{\alpha}H(t,s)ds-$$

$$-\liminf_{t\to\infty}\frac{1}{H(t,T_0)}\int_{T_0}^{t}\frac{p(s)h^{\alpha+1}(t,s)}{\lambda(\alpha+1)^{\alpha+1}H^{\alpha}(t,s)}ds,$$

and by $(\mathbb{C}_5)$ we have:

$$\liminf_{t\to\infty}\frac{1}{H(t,T_0)}\int_{T_0}^{t}\frac{p(s)h^{\alpha+1}(t,s)}{\lambda(\alpha+1)^{\alpha+1}H^{\alpha}(t,s)}ds<\infty$$

If we form a number sequence $\{\sigma_n\}_{n=1}^{\infty}$ in (T_0,∞) that satisfies the conditions:

$$\lim_{n\to\infty}\sigma_n=\infty$$

and

$$\lim_{n\to\infty}[G(\sigma_n)-F(\sigma_n)]=\limsup_{t\to\infty}[G(t)-F(t)]<\infty$$

and apply the procedure as in the proof of Theorem 4, we can conclude that (9) holds, which with (6) again gives a contradiction to the condition $(\mathbb{C}_4)$.

If, apart from the parametric function $H(t,s)$ introduced as to weight function continuous differential function $\rho:[t_0,\infty]\to\mathbb{R}$, it can be shown the following oscillation criteria for equation (RHL):

Theorem 7. *If exist constant $\lambda\in(0,1)$, positive, nondecreasing function $\rho\in C^1([t_0,\infty))$ and function $H\in\mathcal{H}^+(\mathbb{D})$, such that*

$$(\mathbb{C}_7)\qquad\limsup_{t\to\infty}\frac{1}{H(t,t_0)}\cdot$$

$$\cdot\int_{t_0}^{t}\left[q(s)\left(\frac{\tau(s)}{s}\right)^{\alpha}H(t,s)-\frac{p(s)\rho(s)G^{\alpha+1}(t,s)}{\lambda(\alpha+1)^{\alpha+1}H^{\alpha}(t,s)}\right]ds=\infty$$

where is

$$G(t,s)=h(t,s)+\frac{\rho'(s)}{\rho(s)}H(t,s)$$

then equation (RHL) is oscillatory.

Proof. Let $u(t)$ be a nonoscillatory solution of equation (RHL). Without loss of generality, we assume that $u(t)>0$ for $t\geqslant t'$. Then, according to Lemma 1.1. (Bojičić, 2015) $u'(t)>0$ and $u''(t)<0$ for all $t\geqslant t_0$. Now, we define function

$$W(t):=\rho(t)\frac{p(t)(u'(t))^{\alpha}}{u^{\alpha}(t)}\quad for\,t\geqslant t_0$$

Then, for every $t\geqslant t_0$

$$W'(t)=\rho'(t)\frac{p(t)(u'(t))^{\alpha}}{u^{\alpha}(t)}+\rho(t)\frac{[p(t)(u'(t))^{\alpha}]'}{u^{\alpha}(t)}-$$

$$-\rho(t)\alpha p(t)\left(\frac{u'(t)}{u(t)}\right)^{\alpha+1}.$$

Therefore, according to Lemma 1.2. from (Bojičić, 2015), we obtain

$$W'(s)\leqslant W(s)\frac{\rho'(s)}{\rho(s)}-\rho(s)q(s)\lambda\left(\frac{\tau(s)}{s}\right)^{\alpha}-\alpha\frac{W^{\frac{\alpha+1}{\alpha}}(s)}{(\rho(s)p(s))^{\frac{1}{\alpha}}}\quad(17)$$

za for all $t\geqslant t_0=t_0(\lambda)$.

If we multiply (17) by $H(t,s)$ for $t\geqslant s\geqslant t_0$, integrate from t_0 to t, we get

$$\int_{t_0}^{t}W'(s)H(t,s)\,ds\leqslant$$

$$\int_{t_0}^{t}W(s)\frac{\rho'(s)}{\rho(s)}H(t,s)\,ds-\lambda\int_{t_0}^{t}\rho(s)q(s)\left(\frac{\tau(s)}{s}\right)^{\alpha}H(t,s)\,ds-$$

$$-\int_{t_0}^{t}\alpha\frac{W^{\frac{\alpha+1}{\alpha}}(s)}{(\rho(s)p(s))^{\frac{1}{\alpha}}}H(t,s)\,ds,$$

i.e.

$$-W(t_0)H(t,t_0)-\int_{t_0}^{t}W(s)\frac{\partial H(t,s)}{\partial s}ds\leqslant$$

$$\int_{t_0}^{t}\frac{\rho'(s)}{\rho(s)}W(s)H(t,s)\,ds-\lambda\int_{t_0}^{t}\rho(s)q(s)\left(\frac{\tau(s)}{s}\right)^{\alpha}H(t,s)\,ds-$$

$$-\int_{t_0}^{t}\alpha\frac{W^{\frac{\alpha+1}{\alpha}}(s)}{(\rho(s)p(s))^{\frac{1}{\alpha}}}H(t,s)\,ds.$$

From this we conclude:

$$\lambda\int_{t_0}^{t}\rho(s)q(s)\left(\frac{\tau(s)}{s}\right)^{\alpha}H(t,s)\,ds\leqslant\qquad(18)$$

$$W(t_0)H(t,t_0)+\int_{t_0}^{t}W(s)G(t,s)\,ds-\alpha\int_{t_0}^{t}\frac{W^{\frac{\alpha+1}{\alpha}}(s)}{(\rho(s)p(s))^{\frac{1}{\alpha}}}H(t,s)\,ds.$$

If, again, we use inequality Hardly, Littewood & Polya and put:

$$X=(\alpha H(t,s))^{\frac{\alpha}{\alpha+1}}\frac{W(s)}{(\rho(s)p(s))^{\frac{1}{\alpha+1}}},$$

$$Y=\left(\frac{\alpha}{\alpha+1}\right)^{\alpha}\left(\frac{p(s)\rho(s)}{(\alpha H(t,s))^{\alpha}}\right)^{\frac{\alpha}{\alpha+1}}G^{\alpha}(t,s),$$

$$\gamma=\frac{\alpha+1}{\alpha}$$

we get that for all $t>s\geqslant t_0$ holds

$$\alpha H(t,s)\frac{W^{\frac{\alpha+1}{\alpha}}(s)}{(\rho(s)p(s))^{\frac{1}{\alpha}}}+\frac{1}{(\alpha+1)^{\alpha+1}}\frac{p(s)\rho(s)}{H^{\alpha}(t,s)}G^{\alpha+1}(t,s)-$$

$$-W(s)G(t,s)\geqslant0,$$

which implies

$$W(s)G(t,s)-\alpha H(t,s)\frac{W^{\frac{\alpha+1}{\alpha}}(s)}{(\rho(s)p(s))^{\frac{1}{\alpha}}}\leqslant$$

$$\leqslant\frac{p(s)\rho(s)}{(\alpha+1)^{\alpha+1}H^{\alpha}(t,s)}G^{\alpha+1}(t,s).$$

Now, from (18) we get

$$\lambda\int_{t_0}^{t}\rho(s)q(s)\left(\frac{\tau(s)}{s}\right)^{\alpha}H(t,s)\,ds\leqslant W(t_0)H(t,t_0)+$$

$$+ \int_{t_0}^{t} \frac{p(s)\rho(s)}{(\alpha+1)^{\alpha+1} H^\alpha(t,s)} G^{\alpha+1}(t,s)\, ds,$$

so it is

$$\limsup_{t\to\infty} \frac{1}{H(t,t_0)} \cdot$$

$$\cdot \int_{t_0}^{t} \left[\rho(s) q(s) \left(\frac{\tau(s)}{s} \right)^\alpha H(t,s) - \frac{p(s)\rho(s)}{(\alpha+1)^{\alpha+1} H^\alpha(t,s)} G^{\alpha+1}(t,s) \right] ds$$

$$\leqslant \frac{W(t_0)}{\lambda}$$

which contradicts $(\mathbb{C}_7)$.

Corollary 8. *If exist constant $\lambda \in (0,1)$, positive, nondecreasing function $\rho \in C^1([t_0,\infty))$ and function $H \in \mathcal{H}^+(\mathbb{D})$, such that*

$$(\mathbb{C}_8) \qquad \limsup_{t\to\infty} \frac{1}{H(t,t_0)} \int_{t_0}^{t} \frac{p(s)\rho(s)}{H^\alpha(t,s)} G^{\alpha+1}(t,s)\, ds < \infty$$

and

$$(\mathbb{C}_9) \qquad \limsup_{t\to\infty} \frac{1}{H(t,t_0)} \int_{t_0}^{t} \rho(s) q(s) \left(\frac{\tau(s)}{s} \right)^\alpha H(t,s)\, ds = \infty$$

then equation (RHL) is oscillatory.

The purpose of introducing weighting function $\rho \in C^1([t_0,\infty))$ is justified by the following example:

Example 9. Consider the differential equation

$$(E_3) \qquad \left[t^\nu \left| u'(t) \right|^{\alpha-1} u'(t) \right]' + \frac{1}{t^2} \left| u\left(\frac{t}{3}\right) \right|^{\alpha-1} u\left(\frac{t}{3}\right) = 0$$

where is ν i α constants such that $0 \leqslant \nu < \alpha \neq 2$. If we take that functions $H(t,s) = (t-s)^2$ and $\rho(t) = t^3$, we can prove that the conditions $(\mathbb{C}_8)$ i $(\mathbb{C}_9)$ hold. Indeed:

$$(\mathbb{C}_8) \qquad \frac{1}{t^2} \int_{t_0}^{t} \frac{p(s)\rho(s)}{H^\alpha(t,s)} G^{\alpha+1}(t,s)\, ds =$$

$$= \frac{1}{t^2} \int_{t_0}^{t} \frac{s^{\nu+3}}{(t-s)^{2\alpha}} \left[2(t-s) + \frac{3}{s}(t-s)^2 \right]^{\alpha+1} ds =$$

$$= \frac{1}{t^2} \int_{t_0}^{t} s^{\nu+3} (t-s)^{1-\alpha} \frac{2^{\alpha+1}}{s^{\alpha+1}} \left[s + 3(t-s) \right]^{\alpha+1} ds \leqslant$$

$$\leqslant \frac{2^{\alpha+1}}{t^2} (t + 3(t-t_0))^{\alpha+1} (t-t_0)^{1-\alpha} \frac{t^{\nu+2-\alpha+1} - t_0^{\nu+2-\alpha+1}}{\nu+2-\alpha+1} \leqslant$$

$$\leqslant 2^{\alpha+1} 4^{\alpha+1} t^{\alpha+1+1-\alpha-2} \frac{t^{\nu-\alpha+3}}{\nu-\alpha+3} =$$

$$= \frac{8^{\alpha+1}}{\nu-\alpha+3} t^{\nu-\alpha+3} \xrightarrow[t\to\infty]{} 0,$$

when is $\nu - \alpha + 3 < 0$, i.e. where $\nu < \alpha - 3$ and

$$(\mathbb{C}_9) \quad \frac{1}{t^2} \int_{t_0}^{t} q(s) \left(\frac{\tau(s)}{s} \right)^\alpha \rho(s) H(t,s)\, ds = \frac{1}{t^2} \int_{t_0}^{t} \frac{s}{3^\alpha} (t-s)^2\, ds \geq$$

$$\geq \frac{t_0}{3^{\alpha+1} t^2} (t-t_0)^3 = \frac{t_0 t^3}{3^{\alpha+1}} \left(1 - \frac{t_0}{t} \right)^3 \xrightarrow[t\to\infty]{} \infty.$$

Hence, according to Corollary 5, equation (E_3) is oscillatory.

Using a Riccati's technique and starting from the generality of Riccati's differential inequality (17), i.e. the corresponding integral inequality (18), procedure as in the proof of Theorem 4, i.e. Theorem 6, can be prove the following two oscillation criteria for equation (RHL):

Theorem 10. *Suppose that from $H \in \widetilde{\mathcal{H}}(D)$ hold*

$$\limsup_{t\to\infty} \frac{1}{H(t,t_0)} \int_{t_0}^{t} \frac{p(s)\rho(s)}{H^\alpha(t,s)} G^{\alpha+1}(t,s)\, ds < \infty.$$

If there is function $\varphi \in C([t_0,\infty))$ which satisfies the condition $(\mathbb{C}_4)$ and for some constant $\lambda \in (0,1)$ condition

$$\limsup_{t\to\infty} \frac{1}{H(t,T)} \cdot$$

$$\int_{T}^{t} \left[\rho(s) q(s) \left(\frac{\tau(s)}{s} \right)^\alpha H(t,s) - \frac{p(s)\rho(s)}{\lambda(\alpha+1)^{\alpha+1} H^\alpha(t,s)} G^{\alpha+1}(t,s) \right] ds$$

$$\geqslant \varphi(T)$$

holds for all $T \geqslant t_0$, then equation (RHL) is oscillatory.

Theorem 11. *Suppose that for fuction $H \in \widetilde{\mathcal{H}}(D)$ holds*

$$\limsup_{t\to\infty} \frac{1}{H(t,t_0)} \int_{t_0}^{t} \rho(s) q(s) \left(\frac{\tau(s)}{s} \right)^\alpha H(t,s)\, ds < \infty.$$

If there is function $\varphi \in C([t_0,\infty))$ which satisfies the condition $(\mathbb{C}_4)$ and for some constant $\lambda \in (0,1)$ condition

$$\limsup_{t\to\infty} \frac{1}{H(t,T)} \cdot$$

$$\int_{T}^{t} \left[\rho(s) q(s) \left(\frac{\tau(s)}{s} \right)^\alpha H(t,s) - \frac{p(s)\rho(s)}{\lambda(\alpha+1)^{\alpha+1} H^\alpha(t,s)} G^{\alpha+1}(t,s) \right] ds$$

$$\geqslant \varphi(T)$$

for all $T \geqslant t_0$, then equation (RHL) is oscillatory.

Consider the differential equation
(RHL')
$$\left[p(t) \left| u'(\theta(t)) \right|^{\alpha-1} u'(\theta(t)) \right]' + q(t) |u(\tau(t))|^{\alpha-1} u(\tau(t)) = 0$$

where is functions p, q, τ satisfies conditions $(a)-(d)$ and function θ satisfy conditions
(e)
$$\theta \in C^1([t_0,\infty); [0,\infty)), \ \lim_{t\to\infty} \theta(t) = \infty, \ \theta'(t) \geqslant 0 \text{ for all } t \geqslant t_0$$

and

$$\theta(t) \geqslant t, \quad t \geqslant t_0.$$

Using Lemma 1.1. from (Bojičić, 2015), if $u(t) > 0$, $t \geqslant t_0$ is nonoscillatory solution of equation (RHL') such that $u(\tau(t))$ i $u(\theta(t)) > 0$, $t \geqslant t_0$, then is $u'(t) > 0, u'(\theta(t)) > 0, u''(t) < 0$ i $u''(\theta(t)) < 0$ for $t \geqslant t_0$. For the function $w(t)$ defined by

$$w(t) = \frac{p(t)(u'(\theta(t)))^\alpha}{u^\alpha(t)}, \quad t \geqslant T_0$$

using by Lemma 1.2. from (Bojičić, 2015) we obtain

$$w'(t) = -q(t)\frac{u^\alpha(\tau(t))}{u^\alpha(t)} - \alpha p(t)\frac{(u'(\theta(t)))^\alpha u'(t)}{u^{\alpha+1}(t)}$$

$$\leqslant -\lambda q(t)\left(\frac{\tau(t)}{t}\right)^\alpha - \alpha p(t)\left(\frac{u'(\theta(t))}{u(t)}\right)^{\alpha+1}, \quad t \geqslant T_0 = T_0(\lambda) \geqslant t_0.$$

Hence, for equation (RHL') is valid Riccatie's inequality

$$w'(t) \leqslant -\lambda q(t)\left(\frac{\tau(t)}{t}\right)^\alpha - \alpha\frac{w^{\frac{\alpha+1}{\alpha}}(t)}{p^{\frac{1}{\alpha}}(t)}, \quad t \geqslant T_0,$$

which has the same shape as (2). We conclude that for equation (RHL'), all the above proven results will be valid.

REFERENCES

Bojičić, R. 2015. Oscillation properties of half-linear differential equation with delay. In Proceedings of the Sixth Mathematical Conference of the Republic of Srpska. in Serbian, pp. 122–134.

El-Sheikh, M. & Sallam, R. 2000. Oscillation criteria for second order functional differential equations. Applied Mathematics and Computation, 115(2-3), pp. 113-121.

Elbert, A. 1979. A half-linear second order differential equation. Colloquia Mathematica Societatis Janos Bolyai, 30, pp. 153-180.

Hardly, G., Littlewood, J., & Polya, G. 1988. Inequalities. Cambridge University.

Hsu, H. & Yeh, C. 1996. Oscillations theorems for second-order half-linear differential equations. Applied Mathematics Letters, 9(6), pp. 71-77.

Kusano, T. & Naito, Y. 1997. Oscillation and nonoscillation criteria for second-order quasilinear differential equations. Mathematica Hungarica, 76(1-2), pp. 81-99.

Kusano, T. & Wang, J. 1995. Oscillation properties of halflinear functional differential equation of the second order. Hiroshima Mathematical Journal, 25(2), pp. 371-385.

Li, H. J. 1995. Oscillation Criteria for Second Order Linear Differential Equations. Journal of Mathematical Analysis and Applications, 194(1), pp. 217-234. doi:10.1006/jmaa.1995.1295.

Manojlović, J. 1999. Oscillation criteria for second-order half-linear differential equations. Mathematical and Computer Modelling, 30(5-6), pp. 109-119. doi:10.1016/s0895-7177(99)00151-x.

Mirzov, J. D. 1976. On some analogs of Sturm's and Kneser's theorems for nonlinear systems. Journal of Mathematical Analysis and Applications, 53(2), pp. 418-425. doi:10.1016/0022-247x(76)90120-7.

Philos, C. G. 1989. Oscillation theorems for linear differential equations of second order. Archiv der Mathematik, 53(5), pp. 482-492. doi:10.1007/bf01324723.

Wang, J. 1997. Oscillation and nonoscillation theorems for a class of second order quasilinear functional-differential equations. Hiroshima Mathematical Journal, 27(3), pp. 449-466. doi:10.32917/hmj/1206126963.

FIXED POINT RESULTS FOR WEAK *S*-CONTRACTIONS VIA *C*-CLASS FUNCTIONS

LJILJANA PAUNOVIĆ[1], MÜZEYYEN SANGURLU SEZEN[2], ARSLAN HOJAT ANSARI[3]

[1]Teacher Education Faculty in Prizren-Leposavić, University of Priština, Leposavić, Serbia
[2]Department of Mathematics, Faculty of Science and Arts, Giresun University, Giresun, Turkey
[3]Department of Mathematics, Islamic Azad University, Faculty of Science, Karaj, Iran

ABSTRACT

In this paper, we prove some fixed point results for weak *S*-contraction mappings in partially ordered 2-metric spaces via *C*-class function. Our results are different and more general to the usual methods in the literature.

Keywords: *C*-class function, Weak *S*-contraction, Fixed point.

INTRODUCTION

Banach (1922) proved an important contraction principle. Many authors have been interested in this principle. Kannan (1968) established some contraction conditions in complete metric spaces. Choudhury (2009) and Shukla (see Shukla & Tiwari, 2011) proved some fixed point theorems for weakly *C*-contraction and weakly *S*-contraction mappings in complete metric spaces. Gähler (1963) introduced the notion of a 2-metric. Later, many authors obtained some fixed point theorems (Dung & Hang, 2013; Iseki, 1976). On the other hand, Birgani et al. (2018) established the definition of weak *S*-contraction and they proved some fixed point theorems for weak *S*-contraction. In this paper, we generalize weak *S*-contraction using *C*-class function. We prove some fixed point results in partially ordered 2-metric space. We obtain more general results and extend some known results in the existing literature.

Definition 1.1. (Birgani et al., 2018) Let $(Z, \preceq)$ is a partially ordered set. A mapping $P:Z \to Z$ is said to be monotone non-decreasing if $x, y \in Z$, $x \preceq y$, then $Px \preceq Py$.

Definition 1.2. (Gähler, 1963) Let Z be a non-empty set and $d_z : Z \times Z \times Z \to \mathbb{R}$ be a map such that:

(i) For every pair of distinct point $x, y \in Z$, there exists a point $z \in Z$, such that $d_z(x, y, z) \neq 0$.

(ii) If at least two of three points x, y, z are the same, then $d_z(x, y, z) = 0$.

(iii) For all $x, y, z \in Z$, $d_z(x, y, z) = d_z(x, z, y) = d_z(y, x, z)$
$= d_z(y, z, x) = d_z(z, x, y) = d_z(z, y, x)$.

(iv) For all $x, y, z, p \in Z$,
$d_z(x, y, z) \leq d_z(x, y, p) + d_z(y, z, p) + d_z(z, x, p)$.

Then d_z is called a 2-metric on Z and (Z, d_z) is called a 2-metric space.

Definition 1.3. (Iseki, 1975) Let (Z, d_z) be a 2-metric space and $\{x_n\}$ be a sequence in Z

(i) A sequence $\{x_n\}$ is said to be convergent to x in (Z, d_z), denoted by $\lim_{n \to \infty} x_n = x,$ if $\lim_{n \to \infty} d_z(x_n, x, a) = 0$, for all $a \in Z$.

(ii) A sequence $\{x_n\}$ is a Cauchy sequence if $\lim_{n,m \to \infty} d_z(x_n, x_m, a) = 0$, for all $a \in Z$.

(iii) The 2-metric space (Z, d_z) is called complete if every Cauchy sequence is a convergent.

Definition 1.4. (Birgani et al., 2018) Let $(Z, \preceq, d_z)$ be a partially ordered 2-metric space and $P:Z \to Z$ be a map. Then, P is a called a weak *S*-contractions if there exists $\Psi:[0,\infty)^3 \to [0,\infty)$ which is continuous and $\Psi(\omega, s, p)=0$, if and only if $s=\omega=p=0$ such that

$$d_z(Px, Py, a) \leq \frac{1}{3}\big(d_z(x, Py, a) + d_z(y, Px, a) + d_z(x, y, a)\big) \\ - \Psi\big(d_z(x, Py, a), d_z(y, Px, a), d_z(x, y, a)\big) \qquad (1)$$

for all $x, y, a \in Z$ and $x \preceq y$ or $y \preceq x$.

Definition 1.5. (Ansari, 2014) Let $F:[0,\infty)^2 \to \mathbb{R}$ be mapping, F is said to be *C*-class function if it satisfies following conditions:

1) F is continuous,

2) $F(s, p) \leq s$,

3) $F(s, p) = s$ implies that either $s=0$ or $p=0$, for all $s, p \in [0,\infty)$ and $F(0,0) = 0$.

MAIN RESULTS

In this section, we present our main theorem. Let $\mathcal{C}$ denote all *C*-class functions. In this paper we gives Theorem 2.1 that shows the broadering of Theorem 4 in Birgani et al. (2018) using the *C*-class functions.

* Corresponding author: ljiljana.paunovic@pr.ac.rs

MATHEMATICS, COMPUTER SCIENCE AND MECHANICS

Now we give by the function F generalization of the condition (5) from Birgani et al. (2018) as

$$d_z(Px, Py) \leq F(\frac{1}{3}[d_z(x, Py) + d_z(Px, y) + d_z(x, y)],$$
$$\Psi(d_z(x, Py), d_z(Px, y), d_z(x, y))).$$

Theorem 2.1. Let $(Z, \preceq, d_z)$ be a partially ordered 2-metric space, F is element of $\mathfrak{C}$ and $P : Z \to Z$ is a weak S-contraction such that

(i) P is continuous and non-decreasing.

(ii) There exists $y_0 \in Z$ such that $y_0 \preceq Py_0$.

Then P has a fixed point.

Proof: The first part of proof of this theorem is very similar to the proof of Theorem 4 in Birgani et al. (2018). In our case we using the C-class function.

If $y_0 = Py_0$, then the proof is complete. Let $y_0 \preceq Py_0$. Since P is a non decreasing, we get $y_0 \preceq Py_0 \preceq P^2 y_0 \preceq \ldots \preceq P^n y_0 \preceq \ldots$ Now we take $y_{n+1} = Py_n$. Then, for all $n \geq 1$ and for all $a \in Z$, since y_{n-1} and y_n are comparable and from (1), we obtain

$$d_z(y_{n+1}, y_n, a) = d_z(Py_n, Py_{n-1}, a)$$
$$\leq F(\frac{1}{3}[d_z(y_n, Py_{n-1}, a) + d_z(y_{n-1}, Py_n, a) + d_z(y_n, y_{n-1}, a)],$$
$$\Psi[d_z(y_n, Py_{n-1}, a), d_z(y_{n-1}, Py_n, a), d_z(y_n, y_{n-1}, a)])$$
$$= F(\frac{1}{3}[d_z(y_n, y_n, a) + d_z(y_{n-1}, y_{n+1}, a) + d_z(y_n, y_{n-1}, a)],$$
$$\Psi[d_z(y_n, y_n, a), d_z(y_{n-1}, y_{n+1}, a), d_z(y_n, y_{n-1}, a)])$$
$$= F(\frac{1}{3}[d_z(y_{n-1}, y_{n+1}, a) + d_z(y_n, y_{n-1}, a)],$$
$$\Psi(d_z(y_{n-1}, y_{n+1}, a), d_z(y_n, y_{n-1}, a)))$$
$$\leq \frac{1}{3}[d_z(y_{n-1}, y_{n+1}, a) + d_z(y_n, y_{n-1}, a)] \qquad (2)$$

By putting $a = y_{n-1}$ in (2), we obtain $d_z(y_{n+1}, y_n, y_{n-1}) \leq 0$, that is

$$d_z(y_{n+1}, y_n, y_{n-1}) = 0. \qquad (3)$$

It follow from (2) and (3)

$$d_z(y_{n+1}, y_n, a) \leq \frac{1}{3}[d_z(y_{n-1}, y_n, a) + d_z(y_n, y_{n+1}, a)$$
$$+ d_z(y_{n-1}, y_n, y_{n+1}) + d_z(y_n, y_{n-1}, a)]$$
$$= \frac{2}{3}d_z(y_{n-1}, y_n, a) + \frac{1}{3}d_z(y_n, y_{n+1}, a). \qquad (4)$$

That is

$$d_z(y_{n+1}, y_n, a) \leq d_z(y_{n-1}, y_n, a). \qquad (5)$$

Hence $\{d_z(y_n, y_{n+1}, a)\}$ is a decreasing sequence. So it is convergent sequence. Let

$$\lim_{n \to \infty} d_z(y_{n+1}, y_n, a) = p. \qquad (6)$$

Passing to limit $n \to \infty$ in (4) and from (6), we obtain

$$p \leq \frac{1}{3}\left[\lim_{n \to \infty} d_z(y_{n-1}, y_{n+1}, a) + p\right] \leq \frac{1}{3}(p + p + p) = p.$$

That is

$$\frac{2}{3}p \leq \frac{1}{3}\lim_{n \to \infty} d_z(y_{n-1}, y_{n+1}, a) \leq \frac{2}{3}p.$$

That is

$$2p \leq \lim_{n \to \infty} d_z(y_{n-1}, y_{n+1}, a) \leq 2p.$$

Therefore

$$\lim_{n \to \infty} d_z(y_{n-1}, y_{n+1}, a) = 2p. \qquad (7)$$

Letting $n \to \infty$ in (2) and from (6) and (7), we obtain

$$p \leq F(\frac{1}{3}(2p + p), \Psi(0, 2p, p)) \leq \frac{1}{3}(2p + p) = p. \qquad (8)$$

Then from (6), we have

$$\lim_{n \to \infty} d_z(y_{n+1}, y_n, a) = 0. \qquad (9)$$

From (5), we get if $d_z(y_{n-1}, y_{n+1}, a) = 0$, then $d_z(y_n, y_{n+1}, a) = 0$. Since $d_z(y_0, y_1, y_0) = 0$, we get $d_z(y_n, y_{n+1}, y_0) = 0$. Since $d_z(y_{m-1}, y_m, y_m) = 0$. Thus, we get

$$d_z(y_n, y_{n+1}, y_m) = 0, \text{ for all } n \geq m - 1. \qquad (10)$$

Let $0 \leq n < m - 1$, then, we get $m - 1 \geq n + 1$. From (10) we get $d_z(y_{m-1}, y_m, y_{n+1}) = d_z(y_{m-1}, y_m, y_n) = 0$. It implies that

$$d_z(y_n, y_{n+1}, y_m) \leq d_z(y_n, y_{n+1}, y_{m-1}) + d_z(y_{n+1}, y_m, y_{m-1})$$
$$+ d_z(y_n, y_m, y_{m-1}) = d_z(y_n, y_{n+1}, y_{m-1}). \qquad (11)$$

Since $d_z(y_n, y_{n+1}, y_{n+1}) = 0$ from (11), we obtain

$$d_z(y_n, y_{n+1}, y_m) = 0, \quad \text{for} \quad 0 \leq n < m - 1. \qquad (12)$$

From (10) and (12), we get $d_z(y_n, y_{n+1}, y_m) = 0$, for all $n, m \in \mathbb{N}$. For all $\eta, \mu, \kappa \in \mathbb{N}$ with $\eta > \mu$ we get $d_z(y_{\eta-1}, y_\eta, y_\mu) = d_z(y_{\eta-1}, y_\eta, y_k) = 0$. Therefore

$$d_z(y_\eta, y_\mu, y_k) \leq d_z(y_\mu, y_\eta, y_{\eta-1}) + d_z(y_\eta, y_k, y_{\eta-1})$$
$$+ d_z(y_k, y_\mu, y_{\eta-1}) \leq d_z(y_\mu, y_{\eta-1}, y_k) \qquad (13)$$
$$\leq \ldots \leq d_z(y_\eta, y_\mu, y_k) = 0.$$

Hence, for all $\eta, \mu, \kappa \in \mathbb{N}$, we get

$$d_z(y_\eta, y_\mu, y_\kappa) = 0. \tag{14}$$

Now we show that $\{y_n\}$ is a Cauchy sequence. Suppose to the contrary that $\{y_n\}$ is not a Cauchy sequence. Then there exists $\xi > 0$ for which we can find subsequence $\{y_{n(k)}\}$ and $\{y_{m(k)}\}$ where $n(k)$ is the smallest integer such that $n(k) > m(k) > k$ and $y_{n(k)-1}, y_{m(k)-1}$ are comparable and

$$d_z(y_{n(k)}, y_{m(k)}, a) \geq \xi, \text{ for all } k \in \mathbb{N}. \tag{15}$$

Therefore,

$$d_z(y_{n(k)-1}, y_{m(k)}, a) \geq \xi.$$

Then from (13), (14), (15), we get

$$\xi \leq d_z(y_{n(k)}, y_{m(k)}, a) = d_z(Py_{n(k)-1}, Py_{m(k)-1}, a)$$
$$\leq F(\frac{1}{3}\big[d_z(y_{n(k)-1}, Py_{m(k)-1}, a) + d_z(y_{m(k)-1}, Py_{n(k)-1}, a)$$
$$+ d_z(y_{m(k)-1}, y_{n(k)-1}, a) \big],$$
$$\Psi\big[d_z(y_{n(k)-1}, Py_{m(k)-1}, a), d_z(y_{m(k)-1}, Py_{n(k)-1}, a),$$
$$d_z(y_{m(k)-1}, y_{n(k)-1}, a) \big])$$
$$= F(\frac{1}{3}\big[d_z(y_{n(k)-1}, y_{m(k)}, a) + d_z(y_{m(k)-1}, y_{n(k)}, a)$$
$$+ d_z(y_{m(k)-1}, y_{n(k)-1} a) \big],$$
$$\Psi(d_z(y_{n(k)-1}, y_{m(k)}, a), d_z(y_{m(k)-1}, y_{n(k)}, a),$$
$$d_z(y_{m(k)-1}, y_{n(k)-1}, a))). \tag{16}$$

Now, by using (13), (14) and (15), we obtain

$$\xi \leq d_z(y_{n(k)}, y_{m(k)}, a) \leq d_z(y_{n(k)}, y_{n(k)-1}, a)$$
$$+ d_z(y_{n(k)-1}, y_{m(k)}, a) + d_z(y_{n(k)}, y_{m(k)}, y_{n(k)-1}). \tag{17}$$

Letting $k \to \infty$ in (17), from (9), we get

$$\xi \leq \lim_{k \to \infty} d_z(y_{n(k)}, y_{m(k)}, a) \leq \xi$$

and

$$\xi \leq \lim_{k \to \infty} d_z(y_{m(k)-1}, y_{n(k)}, a) + \lim_{k \to \infty} d_z(y_{m(k)-1}, y_{m(k)}, a)$$
$$+ \lim_{k \to \infty} d_z(y_{m(k)-1}, y_{n(k)}, y_{m(k)}) \leq \xi. \tag{18}$$

Therefore,

$$\lim_{k \to \infty} d_z(y_{m(k)}, y_{n(k)}, a) = \xi,$$
$$\lim_{k \to \infty} d_z(y_{m(k)}, y_{n(k)-1}, a) = \xi,$$
$$\lim_{k \to \infty} d_z(y_{m(k)-1}, y_{n(k)}, a) = \xi. \tag{19}$$

Taking the limit as $k \to \infty$ in (16), using (19), from the continuity of Ψ, we get

$$\xi \leq F(\frac{1}{3}[\xi + \xi + \xi], \Psi(\xi, \xi, \xi)) = F(\xi, \Psi(\xi, \xi, \xi)) \leq \xi.$$

That is,

$$F(\xi, \Psi(\xi, \xi, \xi)) = \xi.$$

From Definition 1.5, we get $\xi = 0$ or $\Psi(\xi, \xi, \xi) = 0$ which is a contradiction. Hence $\{y_n\}$ is a Cauchy sequence. Since Z is complete, there exists $\omega \in Z$ such that $\lim_{n \to \infty} y_n = \omega$. Then, it follows from the continuity of P, we have

$$\omega = \lim_{n \to \infty} y_{n+1} = \lim_{n \to \infty} Py_n = P\omega.$$

Therefore, ω is a fixed point of P. This completes the proof. □

In Birgani et al. (2018) the Theorem 6 represents the basis for defining the following Theorem for the case when F is element of $\mathbb{C}$.

Theorem 2.2. Assume that hypotheses from the previous theorem hold and there exists $\omega \in P$ that is comparable to u and v, for each $u, v \in Z$. Then P has a unique fixed point.

Proof. Let u, v be two fixed points of P. We consider the following two cases.

Case 1: If v is comparable to ω, then $P^n v = v$ is comparable to $P^n \omega = \omega$ for all $n \in \mathbb{N}$. Therefore, for all $a \in Z$, and F is element of $\mathbb{C}$, we have

$$d_z(v, \omega, a) = d_z(P^n v, P^n \omega, a)$$
$$\leq F(\frac{1}{3}\big[d_z(P^{n-1} v, P^{n-1} \omega, a) + d_z(P^{n-1} \omega, P^{n-1} v, a) + d_z(v, \omega, a) \big],$$
$$\Psi(d_z(P^{n-1} v, P^{n-1} \omega, a), d_z(P^{n-1} \omega, P^{n-1} v, a), d_z(v, \omega, a))$$
$$= F(\frac{1}{3}\big[d_z(v, \omega, a) + d_z(\omega, v, a) + d_z(v, \omega, a) \big],$$
$$\Psi(d_z(v, \omega, a), d_z(\omega, v, a), d_z(v, \omega, a))) \leq d_z(v, \omega, a).$$

That is

$$F(d_z(v, \omega, a), \psi(d_z(v, \omega, a), d_z(\omega, v, a), d_z(v, \omega, a))) = d_z(v, \omega, a).$$

Hence, from Definition 1.5, we have $d_z(v, \omega, a) = 0$ or $\Psi(d_z(v, \omega, a), d_z(\omega, v, a), d_z(v, \omega, a))) = 0$. Therefore, we obtain $v = \omega$.

Case 2: If v is not comparable to ω, then there exists $u \in Z$ comparable to v and ω. It shows that $P^n u = u$ is comparable to $P^n v = v$ and $P^n \omega = \omega$ for all $n \in \mathbb{N}$. Therefore, for all $a \in Z$, we get

$$d_z(\omega, P^n u, a) = d_z(P^n \omega, P^n u, a)$$

$$\leq F(\frac{1}{3}\Big[d_z(P^{n-1}\omega, P^n u, a) + d_z(P^{n-1}u, P^n \omega, a) + d_z(P^n \omega, P^n u, a)\Big],$$

$$\Psi(d_z(P^{n-1}\omega, P^n u, a), d_z(P^{n-1}u, P^n \omega, a), d_z(P^n \omega, P^n u, a)))$$

$$= F(\frac{1}{3}\Big[d_z(\omega, P^n u, a) + d_z(P^{n-1}u, \omega, a) + d_z(\omega, P^n u, a)\Big],$$

$$\Psi(d_z(\omega, P^n u, a), d_z(P^{n-1}u, \omega, a), d_z(\omega, P^n u, a)))$$

$$\leq \frac{2}{3}d_z(\omega, P^n u, a) + \frac{1}{3}d_z(\omega, P^{n-1}u, a). \qquad (20)$$

That is

$$d_z(\omega, P^n u, a) \leq d_z(\omega, P^{n-1}u, a).$$

Then we obtain $\lim_{n\to\infty} d_z(\omega, P^n u, a) = m$. Passing to limit $n \to \infty$ in (20), from the continuity of Ψ, we get

$$m \leq F(\frac{1}{3}\Big[m + m + m\Big], \Psi(m, m, m)) \leq m.$$

Then, we obtain $F(m, \Psi(m, m, m)) = m$. From the Definition 1.5, we get $m = 0$ or $\Psi(m, m, m) = 0$. That is $m = 0$. Hence $\lim_{n\to\infty} P^n u = \omega$ and $\lim_{n\to\infty} P^n u = v$. Finally, we obtain $v = \omega$. The theorem is thus proved. □

Also, next Theorem represent an expansion of the Theorem 7 in Birgani et al. (2018) for the case when F is element of $\mathfrak{C}$.

Theorem 2.3. Let $(Z, \preceq, d_z)$ be a partially ordered 2-metric space, F is element of C and $P: Z \to Z$ be a weak S-contraction such that

(i) If $u \preceq v$ for all $u, v \in Z$, then $Pu \succeq Pv$.

(ii) There exists $\omega \in Z$ that is comparable to u and v, for each $u, v \in Z$.

(iii) There exists $u_0 \in Z$ with $u_0 \preceq Pu_0$ or $u_0 \succeq Pu_0$.

Then, $\inf\{d_z(u, Pu, a) : u \in Z \setminus \{a\}\} = 0$, for all $a \in Z$. In particular $\inf\{d_z(u, Pu, a) : u \in Z\} = 0$.

Proof: Bearing in mind the proof of the Theorem 7 in Birgani et al. (2018), we proved Theorem 2.3 taking into account that it is F is element of $\mathfrak{C}$.

We consider the following two cases.

Case 1: Let $u_0 \preceq Pu_0$. By the hypothesis *(i)*, consecutive terms of the sequence $\{P^n u_0\}$ are comparable. For all $a \in Z$, it follows (1) that

$$d_z(P^{n+1}u_0, P^n u_0, a)$$

$$\leq F(\frac{1}{3}\Big[d_z(P^n u_0, P^n u_0, a) + d_z(P^{n-1}u_0, P^{n+1}u_0, a)$$

$$+ d_z(P^{n+1}u_0, P^n u_0, a)\Big],$$

$$\Psi(d_z(P^n u_0, P^n u_0, a), d_z(P^{n-1}u_0, P^{n+1}u_0, a),$$

$$d_z(P^{n+1}u_0, P^n u_0, a)))$$

$$= F(\frac{1}{3}\Big[d_z(P^{n-1}u_0, P^{n+1}u_0, a) + d_z(P^{n+1}u_0, P^n u_0, a)\Big],$$

$$\Psi(d_z(P^{n-1}u_0, P^{n+1}u_0, a), d_z(P^{n+1}u_0, P^n u_0, a)))$$

$$\leq \frac{1}{3}\Big[d_z(P^{n-1}u_0, P^{n+1}u_0, a) + d_z(P^{n+1}u_0, P^n u_0, a)\Big]$$

$$\leq \frac{1}{3}\Big[d_z(P^{n-1}u_0, P^n u_0, a) + d_z(P^n u_0, P^{n+1}u_0, a)$$

$$+ d_z(P^{n-1}u_0, P^n u_0, P^{n+1}u_0) + d_z(P^{n+1}u_0, P^n u_0, a)\Big]. \qquad (21)$$

We have $d_z(u_\eta, u_\mu, u_\kappa) = 0$ for all $\eta, \mu, \kappa \in \mathbb{N}$. Then from (21), we get

$$d_z(P^{n+1}u_0, P^n u_0, a) \leq \frac{1}{3}\Big[d_z(P^{n-1}u_0, P^n u_0, a)$$

$$+ \frac{2}{3}d_z(P^n u_0, P^{n+1}u_0, a)\Big].$$

That is

$$d_z(P^{n+1}u_0, P^n u_0, a) \leq d_z(P^{n-1}u_0, P^n u_0, a).$$

Then there exists $\lim_{n\to\infty} d_z(P^{n+1}u_0, P^n u_0, a) = p$. Therefore, according to the previous theorems, we have $p = 0$. Then $\lim_{n\to\infty} d_z(P^{n+1}u_0, P^n u_0, a) = p$. Hence, $\inf\{d_z(u, Pu, a) : u \in Z\} = 0$.

Case 2: Let $u_0 \succeq Pu_0$. It is shown as in Case 1. This completes the proof. □

Example 2.1. Let $Z = [0, \infty)$ and we define a 2-metric d_z on Z by

$$d_z(x, y, a) = \min\{|x - y|, |y - a|, |x - a|\}.$$

Then it is clear that (Z, d_z) is a complete 2-metric space. We define a partial order on Z as follows:

$x \preceq y$ if and only if $x = y$ for all $x, y \in Z$.

Then $(Z, \preceq, d_z)$ is a complete partially ordered 2-metric space. Define $P: Z \to Z$ by $Px = \frac{1}{8}$, $F: [0, \infty)^2 \to \mathbb{R}$ by $F(s, p) = ks$ for $k \in (0, 1)$ and $\Psi: [0, \infty)^3 \to [0, \infty)$ by $\Psi(u, v, \omega) = \frac{u + v + \omega}{8}$. For all $x, y \in Z$ with $x \preceq y$, we have

$$d_z(Px, Py, a) = 0 \leq \frac{1}{3}k(d_z(x, Py, a)$$

$$+ d_z(y, Px, a) + d_z(x, y, a))$$

$$= F(\frac{1}{3}\Big[d_z(x, Py, a) + d_z(y, Px, a) + d_z(x, y, a)\Big],$$

$$\Psi(d_z(x, Py, a), d_z(y, Px, a), d_z(x, y, a))).$$

Hence P is a weak S-contraction. Then, all the conditions of Theorem 2.1 are satisfied. Therefore, $1/8$ is a unique fixed point of P. Moreover, the condition of Theorem 2.2 does not hold. That is, for this example, it is not necessary condition to show uniqueness of the fixed point.

Example 2.2. Let $Z = [0, \infty)$ and we define a 2-metric d_z on Z by

$$d_z(x, y, a) = \begin{cases} 1 & if \quad x \neq y \neq a \\ 0 & if \quad otherwise \end{cases}$$

Then it is clear that (Z, d_z) is a complete 2-metric space. We define a partial order on Z as follows:

$x \preceq y$ if and only if $x = y$ for all $x, y \in Z$.

Then $(Z, \preceq, d_z)$ is a complete partially ordered 2-metric space.

Define $P : Z \to Z$ by $Px = x$, $F : [0, \infty)^2 \to \mathrm{R}$ by $F(s, p) = s - p$ for $k \in (0,1)$ and $\Psi : [0, \infty)^3 \to [0, \infty)$ by $\Psi(u, v, \omega) = \dfrac{\max\{u, v, \omega\}}{4}$.

Clearly, P is a weak S-contraction and all the conditions of Theorem 2.1 are satisfied. Therefore, for all $x \in Z$, x is a fixed point of P. That is P has more than one fixed point.

Conclusion: By using C-class function, we prove more general fixed point results for weak S-contraction in partially ordered 2-metric space. Also, we show that uniqueness of the fixed point of weak S-contraction with necessary conditions. Finally, we give some examples to support our main theorem. Our results are more general than some known results in the existing literature.

REFERENCES

Ali, M., Kamran, T., & Karapınar, E. 2014. Fixed point of α-ψ-contractive type mappings in uniform spaces. Fixed Point Theory and Applications, 2014(1), p. 150. doi:10.1186/1687-1812-2014-150

Banach, S. 1922. Sur les opérations dans les ensembles abstraits et leur application aux équations intégrales. Fundamenta Mathematicae, 3, pp. 133-181. doi:10.4064/fm-3-1-133-181

Birgani, O. T., Koppelaar, H., & Radenović, S. 2018. Fixed point theorems for weak S-contractions in partially ordered 2-metric spaces. Advances in Fixed Point Theory, doi:10.28919/afpt/3625

Choudhury, B. S. 2009. Unique Fixed Point Theorem for Weakly C-Contractive Mappings. Kathmandu University Journal of Science, Engineering and Technology, 5(1), pp. 6-13. doi:10.3126/kuset.v5i1.2842

Dung, N. V., & Le, H. V. T. 2013. Fixed point theorems for weak C-contractions in partially ordered 2-metric spaces. Fixed Point Theory and Applications, 2013(1). doi:10.1186/1687-1812-2013-161

Gähler, S. 1963. 2-metrische Räume und ihre topologische Struktur. Mathematische Nachrichten, 26(1-4), pp. 115-148. doi:10.1002/mana.19630260109

Iseki, K. 1975. Fixed point theorems in 2-metric spaces. Math. Sem. Notes, 3(1975), pp. 133-136.

Iseki, K. 1976. Mathematics on 2-normed spaces. Bull. Korean Math. Soc, 13(2), pp. 127-135.

Kannan, R. 1968. Some results on fixed points. Bull. Cal. Math. Soc., 60, pp. 71-76.

Shukla, D. P., & Tiwari, S. K. 2011. Unique fixed point theorem for weakly S-contractive mappings. Gen. Math. Notes, 4(1), pp. 28-34.

SYSTEM PERFORMANCES OF SC RECEPTION IN ASYMMETRIC MULTIPATH FADING ENVIRONMENTS

DANIJEL ĐOŠIĆ[1*], ČASLAV STEFANOVIĆ[1], DEJAN MILIĆ[2], MIHAJLO STEFANOVIĆ[2]

[1]Faculty of Natural Science and Mathematics, University of Priština, Kosovska Mitrovica, Serbia
[2]Faculty of Electronic Engineering, University of Niš, Niš, Serbia

ABSTRACT

The paper takes into consideration dual-branch selection combining (SC) diversity reception technique in the presence of dissimilar fading at their branches. We efficiently obtained first and second order closed form statistics at the output of the considered model such as probability density function (PDF), cumulative distribution function (CDF) and average level crossing rate (aLCR). Moreover, obtained results are numerically presented for various sets of system model parameters and mainly confirmed by computer based MATLAB simulations.

Keywords: Selection combining (SC), Nakagami-*m* random variable, *α-µ* random variable, PDF, CDF, aLCR.

INTRODUCTION

Fast fading (multipath) has a large impact on the error probability of a wireless telecommunications systems, as well as on the channel information capacity. What kind of distribution will be used to describe the wireless channel in the presence of the fading depends on: i.) whether there is a dominant component, ii.) whether the conditions at the reception have been met that satisfy a central limit theorem, iii.) whether environment has one or multiple clusters and etc. The most commonly used distributions are Rayleigh, Rice, Nakagami-*m*, *η-µ*, *α-µ*, and *κ-µ* (Simon & Alouini, 2000; Panic et al., 2017; Nakagami, 1960; Yacoub, 2007; Djosic et al., 2016; Stefanović & Đošić, 2016). Various diversity techniques are used to reduce the impact of the fast fading on the system performances. Diversity techniques, due to their ability to minimize the effects of fading, are one of the most adequate ways to improve the reliability of the transmission without increasing transmission power and bandwidth. There are several types of diversity combining techniques whose division can in general be made depending on the constraints regarding the complexity of the communication systems and the availability of channel status information (CSI) at the receiver (Simon & Alouini, 2000; Panic et al., 2017).

Selection combining (SC) receiver is one of the simplest and mainly used diversity combining techniques. The SC receiver may have two, three or more inputs. In the case where the SC receiver has two inputs, the signal at the output is equal to the stronger signal at their inputs. Hardware solution of a commercial SC combiner with two inputs is shown in Fig. 1. (Analog Devices, 2015).

Regardless of the fact that other diversity techniques can provide better results (for example, maximal ratio combining and equal gain combining) (Simon & Alouini, 2000; Panic et al., 2017), SC technique due to its simplicity has important application in various wireless communications systems. The papers (Milic et al., 2016; Stefanović et al., 2013; Panajotović et al., 2013) consider first and second order performance analysis of dual branch SC receiver in the presence of co-channel interference. In paper, referenced as (Stefanović & Đošić, 2016), the macro-diversity system is considered with SC reception at micro-level. Moreover, the paper (Djosic et al., 2016; Stefanovic et al., 2017) consider second order statistics of macro-diversity systems with SC at micro-level as well as at macro-level. The vehicle-to-vehicle (V2V) cooperative relay wireless communications over fading channels with SC are considered in (Stefanović et al., 2018; Bithas et al., 2016) while high speed train (HST) wireless communications with selection techniques are investigated in (Laiyemo et al., 2017). Some further insights in selection scheme strategies for wireless transmission are provided in (Swaminathan et al., 2016; Yılmaz & Kucur, 2014; Stefanovic, 2017).
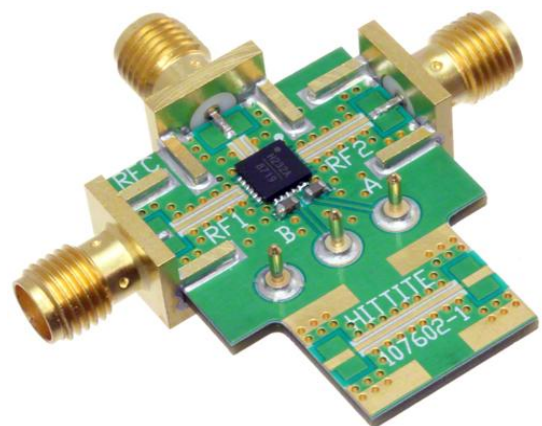

Figure 1. Evaluation board of a commercial dual-branch SC combiner hardware implementation.

This paper analyses SC receiver with two inputs in the presence of Nakagami-*m* fading on one branch and *α-µ* fading on the other branch. Probability density function (PDF), cumulative

* Corresponding author: danijel.djosic@pr.ac.rs

MATHEMATICS, COMPUTER SCIENCE AND MECHANICS

density function (CDF), moments, joint probability density function and level crossing rate (aLCR) of the proposed SC system are calculated, as the closed form expressions and numerically evaluated for various system model set of parameters. Moreover, some obtained results are confirmed by MATLAB simulations.

SYSTEM MODEL

In this section, we consider SC receiver with two inputs. At the first input Nakagami-m multipath fading is presented while at the second input α-μ fading is presented. The block scheme system model is presented in Fig. 2.
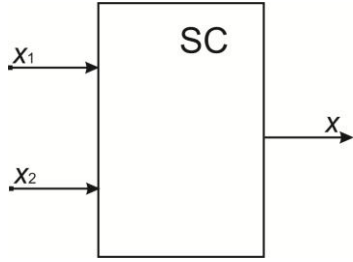

Figure 2. SC block scheme reception with two inputs.

Signals at the inputs are denoted with x_1 and x_2. The output signal is denoted with x. The Nakagami-m distribution describes the signal envelope in linear environments (Nakagami, 1960), while the α-μ distribution describes signal envelope in environment whose dispersion field is not homogeneous (Yacoub, 2007). The probability density function of Nakagami-m random variable x_1 is (Simon & Alouini, 2000; Panic et al., 2017; Nakagami, 1960):

$$p_{x_1}(x_1) = \frac{2}{\Gamma(m_1)}\left(\frac{m_1}{\Omega_1}\right)^{m_1} x_1^{2m_1-1} e^{-\frac{m_1}{\Omega_1}x_1^2}, \quad x_1 \geq 0. \tag{1}$$

where m_1 is fading severity parameter, Ω_1 is mean power. The cumulative distribution function of x_1 is obtained by integration of Nakagami-m probability density function (Simon & Alouini, 2000; Panic et al., 2017; Nakagami, 1960):

$$F_{x_1}(x_1) = \frac{1}{\Gamma(m_1)}\gamma\left(m_1, \frac{m_1}{\Omega_1}x_1^2\right), \quad x_1 \geq 0. \tag{2}$$

The n-th order moment of x_1 or the mean n-th value is equal to (Gradshteyn & Ryzhik, 2000):

$$m_{nx_1} = \overline{x_1^n} = \int_0^\infty dx_1\, x_1 p_{x_1}(x_1) = \frac{2}{\Gamma(m_1)}\left(\frac{m_1}{\Omega_1}\right)^{m_1}$$
$$\times \int_0^\infty dx_1\, x_1^{2m_1-1+n} e^{-\frac{m_1}{\Omega_1}x_1^2} = \frac{1}{\Gamma(m_1)}\left(\frac{\Omega_1}{m_1}\right)^{n/2}\Gamma\left(m_1+\frac{n}{2}\right). \tag{3}$$

The first and second moments of Nakagami-m random variable are:

$$m_1 = \frac{1}{\Gamma(m_1)}\left(\frac{\Omega_1}{m_1}\right)^{1/2}\Gamma\left(m_1+\frac{1}{2}\right). \tag{4}$$

$$m_2 = \overline{x_1^2} = \frac{1}{\Gamma(m_1)}\frac{\Omega_1}{m_1}\Gamma(m_1+1) = \frac{1}{\Gamma(m_1)}\frac{\Omega_1}{m_1}m_1\Gamma(m_1) = \Omega_1. \tag{5}$$

where Ω_1 is by definition the mean square value. The first moment is the mean value, and the second moment is the mean square value. The third-order moment is equal to:

$$m_3 = \frac{1}{\Gamma(m_1)}\left(\frac{\Omega_1}{m_1}\right)^{3/2}\Gamma\left(m_1+\frac{3}{2}\right). \tag{6}$$

Relations can be formed between the usual moments and central moments.

The variance is equal to the difference between the mean square value and the mean value per square. The variation of x_1 is:

$$\sigma_{x_1}^2 = \overline{x_1^2} - \overline{x_1}^2. \tag{7}$$

The joint probability density function from Nakagami-m random process and its first derivative can be obtained as follows. The square of Nakagami-m random process is equal to the sum of $2m$ square Gauss random variables with zero mean values and with the same variations. The variable x_2 has χ^2 distribution (Simon & Alouini, 2000; Panic et al., 2017; Nakagami, 1960). Based on this, x has a Nakagami-m distribution:

$$x^2 = x_1^2 + x_2^2 + ... + x_{2m}^2. \tag{8}$$

The first derivative of x is:

$$\dot{x} = \frac{1}{x}\left(x_1\dot{x}_1 + x_2\dot{x}_2 + ... + x_{2m}\dot{x}_{2m}\right). \tag{9}$$

The first derivative of Gaussian random variable is Gaussian random variable. A linear combination of Gaussian random variables is Gaussian random variable. On this basis the first derivative of x has Gaussian distribution (Middleton, 1960). The mean value is:

$$\overline{\dot{x}} = \frac{1}{x}\left(x_1\overline{\dot{x}_1} + x_2\overline{\dot{x}_2} + ... + x_{2m}\overline{\dot{x}_{2m}}\right) = 0. \tag{10}$$

The mean values of Gaussian first derivatives are equal to zero: $\overline{\dot{x}_1} = \overline{\dot{x}_2} = ... = \overline{\dot{x}_{2m}} = 0$.

The variance of $\dot{x}$ is obtained as the variance summation of each member. The variance of $\dot{x}$ is equal to the product of the square of the constant and the square of the variance of the random variable. Based on this:

$$\sigma_{\dot{x}}^2 = \frac{1}{x^2}\left(x_1^2\sigma_{\dot{x}_1}^2 + x_2^2\sigma_{\dot{x}_2}^2 + ... + x_{2m}^2\sigma_{\dot{x}_{2m}}^2\right). \tag{11}$$

where, $\sigma_{\dot{x}_1}^2 = \sigma_{\dot{x}_2}^2 = \ldots = \sigma_{\dot{x}_{2m}}^2 = 2\pi^2 f_m^2 \sigma^2 = \pi^2 f_m^2 \Omega_1 / m_1$.

The variance of the first derivative is equal to the product of $\pi^2 f_m^2$ a and standard deviation σ^2, the standard deviation is equal to the ratio, Ω_1 / m_1. By substitution:

$$\sigma_{\dot{x}}^2 = \frac{1}{x^2} 2\pi^2 f_m^2 \sigma^2 \left(x_1^2 + x_2^2 + \ldots + x_{2m}^2 \right) = $$
$$= \frac{1}{x^2} 2\pi^2 f_m^2 \sigma^2 x^2 = 2\pi^2 f_m^2 \sigma^2. \tag{12}$$

The probability density function of $\dot{x}$ is Gaussian, since the linear combination of Gaussian random variables is a Gaussian (Middleton, 1960):

$$p_{\dot{x}}(\dot{x}) = \frac{1}{\sqrt{2\pi}\sigma_{\dot{x}}} e^{-\frac{\dot{x}^2}{\sigma_{\dot{x}}^2}}. \tag{13}$$

where $\sigma_{\dot{x}}^2$ is a variance of Gaussian $\dot{x}$ distribution.

Random variables x and $\dot{x}$ are mutually independent. This can be proved numerically. Based on this, joint probability density function of x and $\dot{x}$ is equal to the product of a Nakagami-m random variable and a Gaussian random variable.

$$p_{x_1 \dot{x}_1}(x_1 \dot{x}_1) = \frac{2}{\Gamma(m_1)} \left(\frac{m_1}{\Omega_1} \right)^{m_1} x_1^{2m_1-1} e^{-\frac{m_1}{\Omega_1}x_1^2} \frac{1}{\sqrt{2\pi}\sigma_{\dot{x}_1}} e^{-\frac{\dot{x}_1^2}{2\sigma_{\dot{x}_1}^2}}. \tag{14}$$

To determine the average level crossing rate (aLCR) of the random process, the joint probability density function of the random variable and the first derivative of the random variable should be determined. The aLCR of x_1 can be calculated as mean of the random process (Simon & Alouini, 2000; Panic et al., 2017):

$$N_{x_1} = \int_0^\infty d\dot{x}_1 \, \dot{x}_1 \, p_{x_1 \dot{x}_1}(x_1 \dot{x}_1) = \frac{2}{\Gamma(m_1)} \left(\frac{m_1}{\Omega_1} \right)^{m_1} x_1^{2m_1-1} e^{-\frac{m_1}{\Omega_1}x_1^2} \frac{\sigma_{\dot{x}_1}}{\sqrt{2\pi}}. \tag{15}$$

where: $\sigma_{\dot{x}_1}^2 = \pi^2 f_m^2 \Omega_1 / m_1$.

The random variable x_2 follow an α-μ distribution. The distribution describes signal in a nonlinear and non-homogeneous environment (Simon & Alouini, 2000; Panic et al., 2017; Yacoub, 2007)

$$p_{x_2}(x_2) = \frac{\alpha}{\Gamma(m_2)} \left(\frac{m_2}{\Omega_2} \right)^{m_2} x_2^{\alpha m_2-1} e^{-\frac{m_2}{\Omega_2}x_2^2}, \quad x_2 \ge 0. \tag{16}$$

The relation between x_1 and x_2 is:

$$x_2 = x_1^{2/\alpha}, \quad x_1 = x_2^{2/\alpha}. \tag{17}$$

In this case, x_1 follows a Nakagami-m distribution, and x_2 follows an α-μ distribution. The following relation is between Nakagami-m and α-μ distribution, $m=\mu$. The cumulative distribution probability of x_2 is obtained by integrating the Nakagami-m distribution (Simon & Alouini, 2000; Nakagami, 1960):

$$F_{x_2}(x_2) = \int_0^{x_2} dt \, p_{x_2}(t) = \frac{\alpha}{\Gamma(m_2)} \left(\frac{m_2}{\Omega_2} \right)^{m_2} \int_0^{x_2} dt \, t^{\alpha m_2-1} e^{-\frac{m_2}{\Omega_2}t^\alpha} =$$
$$= \frac{1}{\Gamma(m_2)} \gamma \left(m_2, \frac{m_2}{\Omega_2} x_2^\alpha \right), \quad x_2 \ge 0. \tag{18}$$

The n-th order moment of x_2 is (Simon & Alouini, 2000):

$$m_{nx_2} = \overline{x_2^n} = \int_0^\infty dx_2 \, x_2^n \, p_{x_2}(x_2) =$$
$$= \frac{\alpha}{\Gamma(m_2)} \left(\frac{m_2}{\Omega_2} \right)^{m_2} \int_0^\infty dx_2 \, x_2^{\alpha m_2-1+n} e^{-\frac{m_2}{\Omega_2}x_2^2} = \tag{19}$$
$$= \frac{\alpha}{\Gamma(m_2)} \left(\frac{\Omega_2}{m_2} \right)^{m_2+n/\alpha} \Gamma \left(m_2 + \frac{n}{\alpha} \right).$$

The mean value for the α-μ random variate is obtained for $n=1$:

$$m_{x_{21}} = \frac{1}{\alpha} \left(\frac{\Omega_2}{m_2} \right)^{m_2+1/2} \Gamma \left(m_2 + \frac{1}{\alpha} \right). \tag{20}$$

The mean squared value for the α-μ random variate is obtained for $n=2$:

$$m_{22} = \frac{1}{\Gamma(m_2)} \left(\frac{\Omega_2}{m_2} \right)^{m_2+\frac{2}{\alpha}} \Gamma \left(m_1 + \frac{2}{\alpha} \right). \tag{21}$$

The joint probability density function of α-μ random variable and the first derivative of α-μ random variable is obtained by following transformations (Panic et al., 2017; Yacoub, 2007):

$$x_2 = x_1^{2/\alpha}, \quad x_1 = x_2^{\alpha/2}, \quad \dot{x}_2 = \frac{2}{\alpha} x_1^{2/\alpha-1} \dot{x}_2, \quad \dot{x}_1 = \frac{\alpha}{2} x_2^{\alpha/2-1} \dot{x}_1. \tag{22}$$

The joint probability density function of α-μ random variable and the first derivative of α-μ random variable can be used to calculate the aLCR of α-μ random process. The joint probability density function of x_2 is:

$$p_{x_2 \dot{x}_2}(x_2 \dot{x}_2) = |J| \, p_{x_1 \dot{x}_1} \left(x_2^{\alpha/2}, \frac{\alpha}{2} x_2^{\alpha/2-1} \dot{x}_2 \right). \tag{23}$$

where J is the Jacobian of the transformation, given as:

$$J = \begin{vmatrix} \dfrac{\partial x_1}{\partial x_2} & \dfrac{\partial x_1}{\partial \dot{x}_2} \\ \dfrac{\partial \dot{x}_1}{\partial x_2} & \dfrac{\partial \dot{x}_1}{\partial \dot{x}_2} \end{vmatrix} = \begin{vmatrix} \dfrac{\alpha}{2} x_2^{\alpha/2-1} & 0 \\ 0 & \dfrac{\alpha}{2} x_2^{\alpha/2-1} \end{vmatrix} = \frac{\alpha^2}{4} x_2^{\alpha-2}. \tag{24}$$

By substitution, the combined probability density function of the α-μ random variable and the first derivative of the α-μ random variable is obtained:

MATHEMATICS, COMPUTER SCIENCE AND MECHANICS

$$p_{x_2\dot{x}_2}\left(x_2\dot{x}_2\right)=\frac{\alpha^2}{4}x_2^{\alpha-2}p_{x_1\dot{x}_1}\left(x_2^{\alpha/2},\frac{\alpha}{2}x_2^{\alpha/2-1}\dot{x}_2\right)=\frac{\alpha^2}{4}x_2^{\alpha-2}$$

$$\times\frac{2}{\Gamma\left(m_1\right)}\left(\frac{m_1}{\Omega_1}\right)^{m_1}x_2^{\frac{\alpha}{2}\left(2m_1-1\right)}e^{-\frac{m_1}{\Omega_1}x_2^\alpha}\frac{1}{\sqrt{2\pi}\sigma_{\dot{x}_1}}e^{-\frac{1}{2\sigma_{\dot{x}_1}^2}\frac{\alpha^2}{4}x_2^{\alpha-2}\dot{x}_2^2} \quad (25)$$

$$=\frac{\alpha^2}{2\Gamma\left(m_1\right)}\left(\frac{m_1}{\Omega_1}\right)^{m_1}x_2^{\alpha m_1+\frac{\alpha}{2}+2}\frac{1}{\sqrt{2\pi}\sigma_{\dot{x}_1}}e^{-\frac{m_1}{\Omega_1}x_2^\alpha}e^{-\frac{\alpha^2}{4\sigma_{\dot{x}_1}^2}x_2^{\alpha-2}\dot{x}_2^2}.$$

The aLCR of x_2 is obtained as the mean of the first derivative of the α-μ random variable x_2. The aLCR of the signal at the second input of the SC receiver is (Simon & Alouini, 2000; Panic et al., 2017):

$$N_{x_2}=\int_0^\infty d\dot{x}_2\,\dot{x}_2\,p_{x_2\dot{x}_2}\left(x_2\dot{x}_2\right)=\frac{\alpha^2}{2\Gamma\left(m_1\right)}\left(\frac{m_1}{\Omega_1}\right)^{m_1}$$

$$\times x_2^{\alpha m_1+\frac{\alpha}{2}+2}e^{-\frac{m_1}{\Omega_1}x_2^\alpha}\int_0^\infty d\dot{x}_2\,\dot{x}_2\,e^{-\frac{\alpha^2}{4\sigma_{\dot{x}_1}^2}x_2^{\alpha-2}\dot{x}_2^2}\frac{1}{\sqrt{2\pi}\sigma_{\dot{x}_2}}= \quad (26)$$

$$=\frac{1}{2\sqrt{2\pi}\sigma_{\dot{x}_2}\Gamma\left(m_1\right)}\left(\frac{m_1}{\Omega_1}\right)^{m_1}x_2^{\alpha m_1+\frac{\alpha}{2}+2}e^{-\frac{m_1}{\Omega_1}x_2^\alpha}\frac{1}{2}\frac{4\sigma_{\dot{x}_1}^2}{x_2^{\alpha-2}}.$$

The signal probability density function at the output from the SC receiver is obtained as follows. Signal at the output of the SC receiver is received as a signal from the first input when this signal is greater than the signal at another input or as a signal from another input when the signal at the second input is greater than the signal at the first input. The signal probability at the output from the SC receiver is calculated using the formula:

$$p_x\left(x\right)=p_{x_1}\left(x\right)F_{x_2}\left(x\right)+p_{x_2}\left(x\right)F_{x_1}\left(x\right)=$$

$$\times\frac{2}{\Gamma\left(m_1\right)}\left(\frac{m_1}{\Omega_1}\right)^{m_1}x^{2m_1-1}e^{-\frac{m_1}{\Omega_1}x^2}\frac{1}{\Gamma\left(m_2\right)}\gamma\left(m_2,\frac{m_2}{\Omega_2}x^\alpha\right)+ \quad (27)$$

$$+\frac{\alpha}{\Gamma\left(m_2\right)}\left(\frac{m_2}{\Omega_2}\right)^{m_2}x^{\alpha m_2-1}e^{-\frac{m_2}{\Omega_2}x^\alpha}\frac{1}{\Gamma\left(m_1\right)}\gamma\left(m_1,\frac{m_1}{\Omega_1}x^2\right).$$

The cumulative probability at the output from the SC receivers with two inputs is obtained as a product of cumulative probability from the first and second inputs:

$$F_x\left(x\right)=F_{x_1}\left(x\right)F_{x_2}\left(x\right)=$$

$$=\frac{1}{\Gamma\left(m_1\right)}\gamma\left(m_1,\frac{m_1}{\Omega_1}x^2\right)\frac{1}{\Gamma\left(m_2\right)}\gamma\left(m_2,\frac{m_2}{\Omega_2}x^\alpha\right). \quad (28)$$

where $\gamma\left(n,x\right)$ is an incomplete Gama function, n is the order of Gama function, and x is the argument (Gradshteyn & Ryzhik, 2000).

Moments are important features of the telecommunication random signals. The n-th moment of the signal at the output from the SC receiver can be calculated as:

$$m_{nx}=\overline{x^n}=\int_0^\infty dx\,x^n\,p_x\left(x\right)=\frac{2}{\Gamma\left(m_1\right)}\left(\frac{m_1}{\Omega_1}\right)^{m_1}x^{2m_1+n-1}$$

$$\times e^{-\frac{m_1}{\Omega_1}x^2}\frac{1}{\Gamma\left(m_2\right)}\gamma\left(m_2,\frac{m_2}{\Omega_2}x^\alpha\right)+\frac{\alpha}{\Gamma\left(m_2\right)}\left(\frac{m_2}{\Omega_2}\right)^{m_2} \quad (29)$$

$$\times x^{\alpha m_2+n-1}e^{-\frac{m_2}{\Omega_2}x^\alpha}\frac{1}{\Gamma\left(m_1\right)}\gamma\left(m_1,\frac{m_1}{\Omega_1}x^2\right).$$

The joint probability density function at the output from the SC receiver and its first derivative is:

$$p_{x\dot{x}}\left(x\dot{x}\right)=p_{x_1\dot{x}_1}\left(x\dot{x}\right)F_{x_2}\left(x\right)+p_{x_2\dot{x}_2}\left(x\dot{x}\right)F_{x_1}\left(x\right)=$$

$$=\frac{2}{\Gamma\left(m_1\right)}\left(\frac{m_1}{\Omega_1}\right)^{m_1}x^{2m_1-1}e^{-\frac{m_1}{\Omega_1}x^2}\frac{1}{\sqrt{2\pi}\sigma_{\dot{x}_1}}e^{-\frac{\dot{x}^2}{2\sigma_{\dot{x}_1}^2}}\frac{1}{\Gamma\left(m_2\right)}$$

$$\times\gamma\left(m_2,\frac{m_2}{\Omega_2}x^\alpha\right)+\frac{\alpha^2}{2\Gamma\left(m_2\right)}\left(\frac{m_2}{\Omega_2}\right)^{m_2}x^{\alpha m_2+\alpha/2+2}e^{-\frac{m_2}{\Omega_2}x^\alpha} \quad (30)$$

$$\times\frac{1}{\sqrt{2\pi}\sigma_{\dot{x}_2}}e^{-\frac{\alpha^2}{4\sigma_{\dot{x}_1}^2}x^{\alpha-2}\dot{x}^2}\frac{1}{\Gamma\left(m_1\right)}\gamma\left(m_1,\frac{m_1}{\Omega_1}x^2\right).$$

The previous expression can be used to determine the average level crossing rate (aLCR).

The aLCR of the signal at the output of the SC receiver is calculated as the mean of the first derivative of the output signal of the SC receiver. Averaging is done as the integration of the product of the first derivative and the joint probability. The aLCR of x is:

$$N_x=\int_0^\infty d\dot{x}\,\dot{x}\,p_{x\dot{x}}\left(x\dot{x}\right)=\frac{2}{\Gamma\left(m_1\right)}\left(\frac{m_1}{\Omega_1}\right)^{m_1}x^{2m_1-1}e^{-\frac{m_1}{\Omega_1}x^2}$$

$$\times\frac{1}{\Gamma\left(m_2\right)}\gamma\left(m_2,\frac{m_2}{\Omega_2}x^\alpha\right)\int_0^\infty d\dot{x}\,\dot{x}\,\frac{1}{\sqrt{2\pi}\sigma_{\dot{x}_1}}e^{-\frac{\dot{x}^2}{2\sigma_{\dot{x}_1}^2}}$$

$$+\frac{\alpha^2}{2\Gamma\left(m_2\right)}\left(\frac{m_2}{\Omega_2}\right)^{m_2}x^{\alpha m_2+\alpha/2-2}e^{-\frac{m_2}{\Omega_2}x^\alpha}\frac{1}{\Gamma\left(m_1\right)}$$

$$\times\gamma\left(m_1,\frac{m_1}{\Omega_1}x^2\right)\int_0^\infty d\dot{x}\,\dot{x}\,\frac{1}{\sqrt{2\pi}\sigma_{\dot{x}_2}}e^{-\frac{\alpha^2}{4\sigma_{\dot{x}_1}^2}x^{\alpha-2}\dot{x}^2}= \quad (31)$$

$$=\frac{2}{\Gamma\left(m_1\right)}\left(\frac{m_1}{\Omega_1}\right)^{m_1}x^{2m_1-1}e^{-\frac{m_1}{\Omega_1}x^2}\frac{1}{\Gamma\left(m_2\right)}\frac{1}{\sqrt{2\pi}}\sigma_{\dot{x}_1}$$

$$\times\gamma\left(m_2,\frac{m_2}{\Omega_2}x^\alpha\right)+\frac{\alpha^2}{2\Gamma\left(m_2\right)}\left(\frac{m_2}{\Omega_2}\right)^{m_2}x^{\alpha m_2+\alpha/2-2}$$

$$\times e^{-\frac{m_2}{\Omega_2}x^\alpha}\frac{1}{\Gamma\left(m_1\right)}\gamma\left(m_1,\frac{m_1}{\Omega_1}x^2\right)\frac{1}{\sqrt{2\pi}}\frac{2\sigma_{\dot{x}_2}}{\alpha^2 x^{\alpha-2}}.$$

NUMERICAL RESULTS

The numerical results are obtained, on the basis of expression (27), and are graphically shown in Figure 3. Moreover, analytical results are confirmed by MATLAB

simulations. The signal probability density function at the output from the SC receiver with two inputs depending on the signal envelope is shown with the constant coefficient of non-linearity of the parameter α, and for different values of the number of the cluster μ, the Nakagami-m fading severity m and the mean values of the signal Ω_1 and Ω_2. The increase of the severity fading parameter m and the number of clusters μ results in narrowing the range of the function at the reception, as well as increasing the maximum value achieved for higher values of the received signal level. Increasing the value of the mean signal power Ω_1 and Ω_2 results in the expansion of function range of the signal probability function, as well as the reduction of the maximum value, which also confirms the simulation.
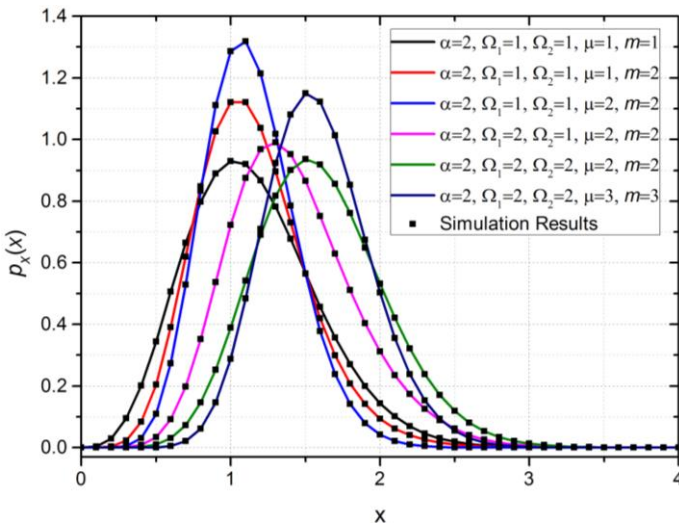

Figure 3. Graphical representation of PDF at the output from the SC receivers with two inputs versus the signal envelope, for different number of cluster μ, the fading severity m and the mean powers of the signals Ω_1 and Ω_2.

The numerical and simulation results for CDF are obtained, and based on expression (28), are graphically plotted versus the envelope signal in Figure 4. The cumulative probability of the signal at the output from the SC receiver with two inputs is shown with the same non-linearity coefficient parameter α, and for different values of the number of clusters μ, Nakagami-m fading severity m and mean powers of signal Ω_1 and Ω_2. Based on analytical expressions, numerical and computer simulation of the obtained results, it can be concluded that with the increase in the amplitude of the signal x, the cumulative probability tends to one. The growth of the cumulative probability is more dominant for the higher values of the parameters, μ and m. Furthermore, with the increase in the mean power values of the signals Ω_1 and Ω_2, CDF decreases.

Using the expression (31), in Figure 5. the normalized aLCRis graphically depicted, versus the normalized envelope of the signal x and the square root of the mean power of the signal Ω, where $\Omega=\Omega_1=\Omega_2$. The figure is presented with the constant values of the fading severity parameter m, and for different

values of the nonlinearity parameter α as well as for different values of the clusters μ. The maximum of the aLCR is higher for the higher values of the clusters μ. Moreover, with the increase in α and μ, the aLCR decreases faster, since less variation of the output signal can be observed.
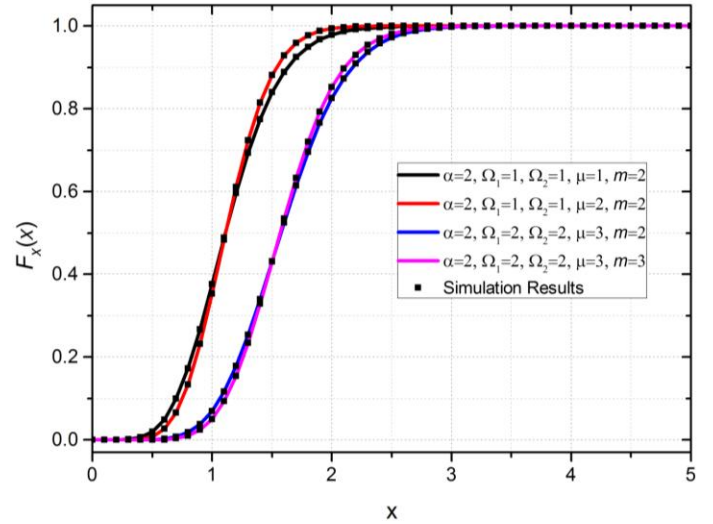
Figure 4. Graphical representation of the numerical results of the CDF signals at the output from the SC receiver with two inputs versus signal envelope, for different cluster values μ, fading severity m and with different mean signal powers Ω_1 and Ω_2.
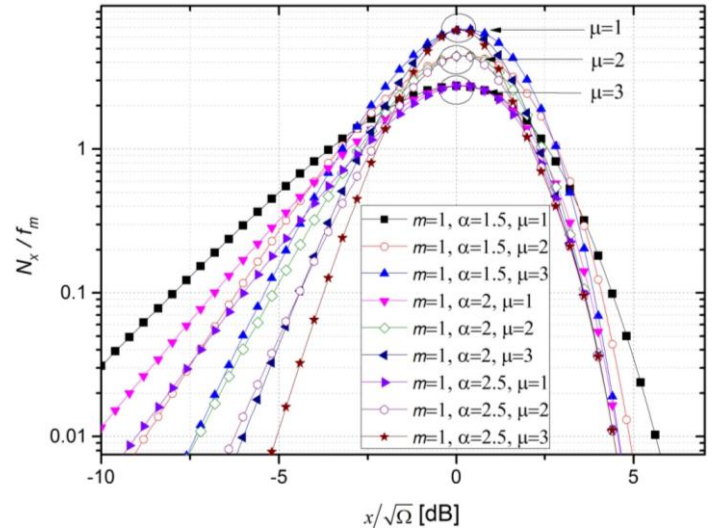
Figure 5. Normalized average number of crossing rates of the signal at the output from the SC receiver with two inputs versus normalized envelope signal, for the different values of the non-linear coefficient α and the number of clusters μ, and for the constant m.

In Figure 6. the normalized aLCR is shown graphically, versus the envelope of the signal xi normalized by the square root of the signal power Ω, where $\Omega=\Omega_1=\Omega_2$, with equal values of the clusters μ, and for the different values of the nonlinearity parameter α as well as with different values of fading severity

parameter m. The maximum of the aLCR is more likely to be higher for the higher m. With the rise in the parameter α and m, the aLCR decreases faster, since less variation of the signal can be noticed.

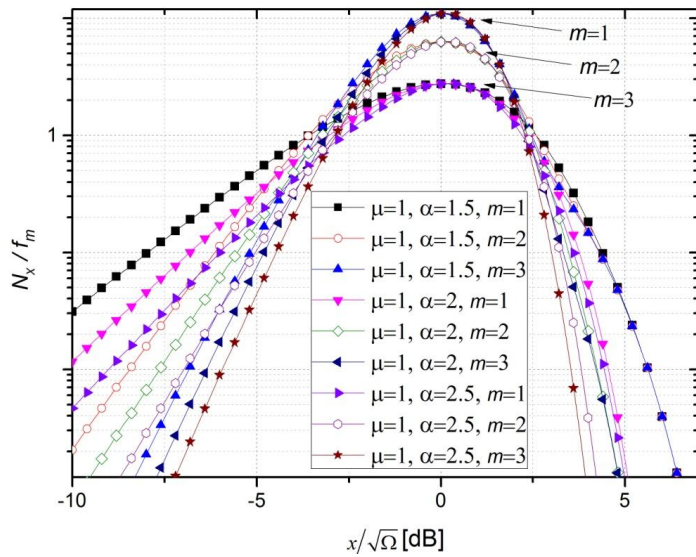**Figure 6.** Normalized aLCR of the signal at the output from the SC receiver with two inputs versusthe envelope signal, for different values of the fading severity parameter m and the non-linearity coefficient α.

CONCLUSION

This paper considers first and second order performance measures of dissimilar dual-branch SC reception in the presence of Nakagami-m and α-μ multipath fading at their asymmetric inputs. The closed form expressions for PDF, CDF, moments, JPDF and aLCR are derived and numerically presented for various values of system parameters. Moreover, the obtained results are verified by MATLAB simulations. It can be concluded, that for higher values of non-linearity parameter α, number of clusters μ as well as fading severity parameter m, the system performances in general can be improved. Our future is going to consider performance measures of dissimilar multi-branch SC reception.

ACKNOWLEDGMENTS

REFERENCES

Analog Devices, "GaAs MMIC SPDT Non-Reflective Switch, DC-12 GHz", HMC232ALP4E datasheet, 2015 [Revised: Aug. 2018]

Bithas, P. S., Efthymoglou, G. P., & Kanatas, A. G. 2016. A cooperative relay selection scheme in V2V communications under interference and outdated CSI. In 2016 IEEE 27th Annual International Symposium on Personal, Indoor, and Mobile Radio Communications (PIMRC). Institute of Electrical and Electronics Engineers (IEEE)., pp. 1-6. doi:10.1109/pimrc.2016.7794741

Djosic, D. B., Stefanovic, D. M., & Stefanovic, C. M. 2016. Level Crossing Rate of Macro-diversity System with Two Micro-diversity SC Receivers over Correlated Gamma Shadowed α–µ Multipath Fading Channels. IETE Journal of Research, 62(2), pp. 140-145. doi:10.1080/03772063.2015.1075913

Gradshteyn, I. S., & Ryzhik, I. M. 2000. Table of Integrals, Series, and Products. New York: Academic. 6th ed.

Laiyemo, A. O., Pennanen, H., Pirinen, P., & Latva-aho, M. 2017. Transmission Strategies for Throughput Maximization in High-Speed-Train Communications: From Theoretical Study to Practical Algorithms. IEEE Transactions on Vehicular Technology, 66(4), pp. 2997-3011. doi:10.1109/tvt.2016.2586118

Middleton, D. 1960. An introduction to statistical communication theory. New York: McGraw-Hill.

Milic, D., Djosic, D., Stefanovic, C., Panic, S., & Stefanovic, M. 2015. Second order statistics of the SC receiver over Rician fading channels in the presence of multiple Nakagami- m interferers. International Journal of Numerical Modelling: Electronic Networks, Devices and Fields, 29(2), pp. 222-229. doi:10.1002/jnm.2065

Nakagami, M. 1960. The m-Distribution—A General Formula of Intensity Distribution of Rapid Fading. In Statistical Methods in Radio Wave Propagation.Elsevier BV., pp. 3-36. doi:10.1016/b978-0-08-009306-2.50005-4

Panajotović, A., Sekulović, N., Drača, D., Stefanović, M., & Stefanović, Č. 2013. Average Fade Duration of Dual Selection Diversity over Correlated Unbalanced Nakagami-m Fading Channels in the Presence of Cochannel Interference. Frequenz, 67(11-12). doi:10.1515/freq-2013-0005

Panic, S., Stefanovic, C., & Milosevic, H. 2017. SIR Based Performance Analysis of Dual-Branch SC Over Correlated kappa-mu Fading Channels. In E. Sabir, A. A. García, M. Ghogho, & M. Debbah Eds., Cham: Springer Science and Business Media LLC., pp. 542-549. doi:10.1007/978-3-319-68179-5_47

Simon, M. K., & Alouini, M. 2000. Digital Communication Over Fading Channels. New York, USA: Wiley. doi:10.1002/0471200697

Stefanović, Č., Pratesi, M., & Santucci, F. 2018. Performance evaluation of cooperative communications over fading channels in vehicular networks. In 2nd URSI Atlantic Science Radio Meeting (AT-RASC).

Stefanovic, C., Panic, S., Jovkovic, S., Simonovic, M., & Stefanovic, M. 2017. Outage Probability of SIR Based SC Macro-Diversity Reception in Gamma Shadowed Rayleigh Multipath Fading Environment. In 2017 Sensor Signal Processing for Defence Conference (SSPD). Institute of Electrical and Electronics Engineers (IEEE)., pp. 1-5. doi:10.1109/sspd.2017.8233255

MATHEMATICS, COMPUTER SCIENCE AND MECHANICS

Stefanovic, C. M. 2017. LCR of amplify and forward wireless relay systems in general alpha-mu fading environment. In 2017 25th Telecommunications Forum (TELFOR). Institute of Electrical and Electronics Engineers (IEEE), pp. 1-6. doi:10.1109/telfor.2017.8249344

Stefanović, Č., & Đošić, D. 2016. The LCR of wireless macrodiversity SSC receiver in the presence of gamma shadowed kappa-mu fading. The University Thought - Publication in Natural Sciences, 6(2), pp. 32-37. doi:10.5937/univtho6-12527

Stefanović, Č., Jakšić, B., Spalević, P., Panić, S., & Trajčevski, Z. 2013. Performance analysis of selection combining over correlated Nakagami-m fading channels with constant correlation model for desired signal and cochannel interference. Radioengineering, 22(4), pp. 1176-1181.

R, S., Roy, R., & Selvaraj, M. D. 2016. Performance Comparison of Selection Combining With Full CSI and Switch-and-Examine Combining With and Without Post-Selection. IEEE Transactions on Vehicular Technology, 65(5), pp. 3217-3230. doi:10.1109/tvt.2015.2434836

Yacoub, M. D. 2007. The alpha-mu Distribution: A Physical Fading Model for the Stacy Distribution. IEEE Transactions on Vehicular Technology, 56(1), pp. 27-34. doi:10.1109/tvt.2006.883753

Yilmaz, A., & Kucur, O. 2014. Performances of Transmit Antenna Selection, Receive Antenna Selection, and Maximal-Ratio-Combining-Based Hybrid Techniques in the Presence of Feedback Errors. IEEE Transactions on Vehicular Technology, 63(4), pp. 1976-1982. doi:10.1109/tvt.2013.2267962

MATHEMATICS, COMPUTER SCIENCE AND MECHANICS

ISOMORPHIC TRANSFORMATION AND ITS APPLICATION TO THE MODULO (2ⁿ + 1) CHANNEL FOR RNS BASED FIR FILTER DESIGN

NEGOVAN STAMENKOVIĆ[1],[★]

[1]Faculty of Natural Sciences and Mathematics, University of Priština, Kosovska Mitrovica, Serbia

ABSTRACT

In this paper, the implementation of a Finite Impulse Response (FIR) filter in the Residue Number System (RNS), is presented, in which a modulo multiplier based on the isomorphism technique is used to perform multiplication in the (2ⁿ + 1) channel. An RNS modular multiplication in the Galois Field GF(2ⁿ + 1) is presented in detail in this paper. The multiplication is based on the isomorphic mapping technique adapted to the residue arithmetic. The isomorphic encoder and decoder look-up tables in the GF(2⁸ + 1) are given. An architecture for FIR filter design based on distributed arithmetic for multiplication and accumulation in mentioned (2ⁿ + 1) channel is also presented. This architecture is discussed in details and compared with with architecture based on isomorphing technique.

Keywords: Galois field, Multiplication, Lookup table, Modular arithmetic, Distributed arithmetic.

INTRODUCTION

Modulo $(2^n + 1)$ multipliers of various types have been considered in literature (a) both inputs in standard representation, (b) one input in standard form and another in diminished-1 form and (c) both inputs in diminished-1 representation.

This paper develops an enhanced algorithm for the arithmetic modular (2^n+1) multiplication problem in the Residue Number System. The proposed algorithm is based on Galois finite field theory (Pradhan, 1978). Galois field (GF(m)) is a number system with a finite number of elements, m, and two main arithmetic operations, called addition and multiplication. Other operations such as division can be derived from those two (Chen et al., 2007). Some of the formal properties of a finite field the following. They consist of a set number of GF(m), and two operations, modular addition (+) and modular multiplication (∗). The result of adding or multiplying two numbers from the finite field is always an element in the field.

Mapping the arithmetic multiplication problem over the Galois field GF(m) eliminates many of the limitations of existing algorithms for modular $(2^n + 1)$ multiplication. And advantage of the proposed algorithm is that it has no restriction on the multiplier and the multiplicand, no diminished one multiplication, and no based extension operation.

A prime Galois field as a multiplier

A prime Galois field $GF(m)$ is a finite field of order m (m is the number of elements) where m is a prime positive integer (Kitsos et al., 2003; Chen et al., 2014). They consist of two operations, modular addition (denoted by +) and modular multiplication (de-

noted by ∗), both operations are communicative and associative, that satisfies the usual arithmetic properties:

(a) The $(GF, +)$ is an Abelian group with an additive neutral element denoted by 0, such that $a + 0 = a$ for any element $a \in GF(m)$.

(b) The $(GF \backslash 0, *)$ excluding the zero element is an Abelian group with a multiplicative neutral element denoted by 1, such that $a * 1 = a$ for any element $a \in GF(m)$.

(c) For every element $a \in GF(m)$, there is an additive inverse element $-a$, such that $a + (-a) = 0$.

(d) For every nonzero element $b \in GF(m)$ there is a multiplicative inverse element b^{-1} such that $b * b^{-1} = 1$.

(c) Multiplication distributes across addition as: $(a + b)c = ac + bc$ and $c(a + b) = ca + cb$ for all $a, b, c \in GF(m)$.

These properties can be satisfied if the field size is any prime number or any integer power of a prime.

The organization of the paper is as follows: Section 2 gives a brief overview of the index mapping method; Section 3 gives a short explanation of the design $(2^4 + 1)$ channel for RNS based FIR filter design using the index mapping method given in Section 2; Section 4 deals with distributed arthmetic and its comparison with isomorphing transformatin; Section 5 deals with the conclusion of the work. Isomorphing encoded and decoded tables for modulu $(m = 2^8 + 1)$ are given in Appendix.

THE INDEX MAPPING OVERVIEW

In the residue number system (RNS), an analogous method which can be, as logarithms multiplication used, to call index calculus (Padmavathy & Bhagvati, 2012). Using index mapping over

---

MATHEMATICS, COMPUTER SCIENCE AND MECHANICS

the Galois Field GF(*m*), the multiplication operation can be implemented by the addition. The multiplication operation in RNS is a modular operation, therefore, multiplication can be done as an addition in RNS, which is easier than multiplication (Qi et al., 2012).

The groups $(G_1, *)$ and $(G_2, \odot)$ are said to be isomorphic if there is a one-to-one correspondence (bijection) $f : G_1 \rightarrow G_2$ that preserves the group operation, in other words, $f(a * b) = f(a) \odot f(b)$, for all $a, b \in G_1$.

The input and output index mapping of RNS numbers is based on the following definitions.

Definition 1. The Euler's $\varphi(n)$ function or the totient function of a positive integer n is the number of integers in the range $(1, 2, \ldots, n - 1)$ which are relatively prime or co-prime to n. If m is prime then $\varphi(m) = m - 1$. □

For example, $\varphi(5) = 4$, the numbers 1, 2, 3, 4 are relatively prime to 5, but 5 is not. If $n = p_1^{k_1} p_2^{k_2} \cdots p_m^{k_m}$, where $p_1, p_2, \ldots, p_m$ are distinct prime divisors of n and $k_i \geq 1$, then

$$\varphi(n) = n(1 - \frac{1}{p_1})(1 - \frac{1}{p_2}) \cdots (1 - \frac{1}{p_m})$$

To calculate Euler's function, the Matlab string given in Listing 1 can be used.

Listing 1. Euler's $\varphi(n)$ function

```
N = 48;          % for example
n = 1:N-1;
ind = gcd(n,N)==1;
tot = n(ind)
```

Definition 2. Let $a \neq 0$ and $m > 0$ be relatively prime. Then x is called the order of a modulo n, denoted $x = \text{ord}_m(a)$ if x is the smallest natural number so that $\langle a^x \rangle_m = 1$. □

For example, order of $a = 3$ modulo $m = 11$ is $\text{ord}_{11}(3) = 5$ because $\langle 3^5 \rangle_{11} = 1$.

Definition 3. Let $m \in N$ and $g \in \mathbb{Z}$ be such that $\gcd(g, m) = 1$. Then g is called a primitive root modulo m if $\text{ord}_m g = \varphi(m)$, i.e. if the order of g is equal to the maximal possible value. In other words, an integer g is a primitive root modulo m if the powers of g generate all residue classes coprime to m. □

For example, let $m = 17$ be a second order Femat number , then the number $g = 3$ is the primitive roots of the prime m.

Listing 2. The number $g = 3$ is a primitive root modulo 17

```
m = 17;          % for example
k = 1:m-1;
g = 3;
ind = mod(g.^k,m);
ind = sort(ind)

ind =
    1 2 3 4 5 6 7 8 9 10 11 12 13 14 15 16
```

Definition 4. Let m be any prime number, and let g be any primitive root of m, then to each integer a, relative prime to m, there is a unique integer (index) i, denoted as $i = \text{ind}_g a$, such that

$$a = \langle g^i \rangle_m, \qquad 0 \leq i < m - 1 \qquad \square$$

Indexes over Galois field GF(*m*) have the following important properties:

1. $\text{ind}_g 1 = 0$,
2. $\text{ind}_g(a \times b) = \langle \text{ind}_g a + \text{ind}_g b \rangle_{m-1}$,
3. $\text{ind}_g a^n = \langle n \times \text{ind}_g a \rangle_{m-1}$,
4. $\text{ind}_g a = \langle \text{ind}_g g' + \text{ind}_g a \rangle_{m-1}$, where g' is any other primitive root.

Definition 5. For integer numbers a, b and m, notation $b = \langle a \rangle_m$ means $a - b$ is divisible by m, that is $m|(a - b)$ or, equivalently, $a - b = km$ for some integer k. □

For any integer a, $r = \langle a \rangle_m$ shall denote the unique integer remainder r, $0 \leq r \leq m - 1$, obtained upon dividing a by m; this operation is called reduction modulo m.

A special technique, based on isomorphic transformations (Jullien, 1980), can be used in RNS to transform the modular multiplication into a simpler modular addition. It is based on the concept of indices that are similar to logarithms, and primitive roots g which are similar to logarithm bases. It is possible to demonstrate that if the number m is a prime there exists a number of primitive roots (the number of the primitive roots can be computed by using the Eulers function) that share the following property: every element of the field $GF(m) = 0, 1, \ldots, m - 1$ excluding the zero element can be generated by using the following equation

$$x = \langle g^k \rangle_m \qquad (1)$$

where k (index) is an integer number and g a primitive root. In this way, an isomorphism exists between the multiplicative group $\{x\} = \{1, 2, \ldots, m - 1\}$ with the multiplication modulo m, and the additive group $\{k_x\} = \{0, 1, \ldots, m - 2\}$ with the addition modulo $m - 1$. Multiplication of two integers can now be performed by adding the corresponding indices mod $(m - 1)$, and then finding its inverse index value. Thus, the product of x and y is given by

$$\langle x \times y \rangle_m = \langle g^{k_x} \rangle_m \times \langle g^{k_y} \rangle_m = g^{\langle k_x + k_y \rangle_{m-1}} \qquad (2)$$

This approach is known as index calculus. By using isomorphisms, the product of the two residue numbers is mapped into the sum of their indexes which are obtained by an isomorphic mapping. The scheme for an index calculus multiplier is shown in Figure 1. This multiplication needs three ROM look-up tables and an addition modulo $(m-1)$.
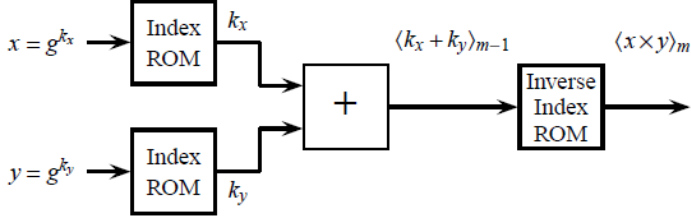

Figure 1. An index calculus multiplier.

The modulo $(m-1)$ adder has two n-bit inputs and one n-bit output, were $n = \lceil \log_2(m-2) \rceil$.

Proposed applications can only be computed with only index ROM and inverse index ROM look-up tables and addition modulo $m-1$.

APPLICATION ISOMORPHING TRANSFORMATION TO THE MODULO $(2^4 + 1)$ CHANNEL FIR FILTER

An m channel of N taps (degree) for RNS based FIR filters is described by the ordinary expression

$$y_n = \sum_{k=0}^{N-1} A_k x_{n-k} \qquad (3)$$

where $x(n)$ is the input to the filter, A_k represents the filter coefficients and y_n is the otput of the filter. This can be implemented using a single Multiply Accumulate (MAC) engine, but it would require N MAC cycles, before the next input sample can be processed. Clearly, it is necessary to apply modular arithmetic.

Two direct isomorphic transformations to obtain $A_n \to k_{A_n}$ and $x_{n-k} \to k_{x,n-k}$, and one inverse isomorphic transformation to obtain $y_n \to \langle k_{A_n} + k_{x,n-k} \rangle_{16}$, are performed. Because of the complexity of modular multiplication, we used the isomorphism technique to implement the product of residues.

The prime number $m = 2^4 + 1 = 17$ is a second order Fermat number and it has 7 primitive roots. The complete list of primitive roots for GF(17) is: $\{3, 5, 6, 7, 10, 11, 12\}$. In isomorphism Table 1 the elements of prime field GF(17), which are generated by using mapping equation, (1), for primitive root $g = 3$, are given.

Table 1. The isomorphism table for $m = 17$ and $g = 3$.

GF(17)	1	3	9	10	13	5	15	11	16	14	8	7	4	12	2	6
k	0	1	2	3	4	5	6	7	8	9	10	11	12	13	14	15

The modular product of two integer elements x and y belonging to the Galois field with m elements is implemented in the following way

1. Forward mapping of $x \in$ GF(m) and $y \in$ GF(m) in the corresponding indices k_x ans k_y.
2. Addition modulo $(m-1)$ of the two indexes.
3. Reverse mapping of the result of the addition to obtain the final result of the modular product.

The block diagram of a typical isomorphic implementation of the three tap modulo 17 channel of RNS FIR filter is shown in Fig. 2.
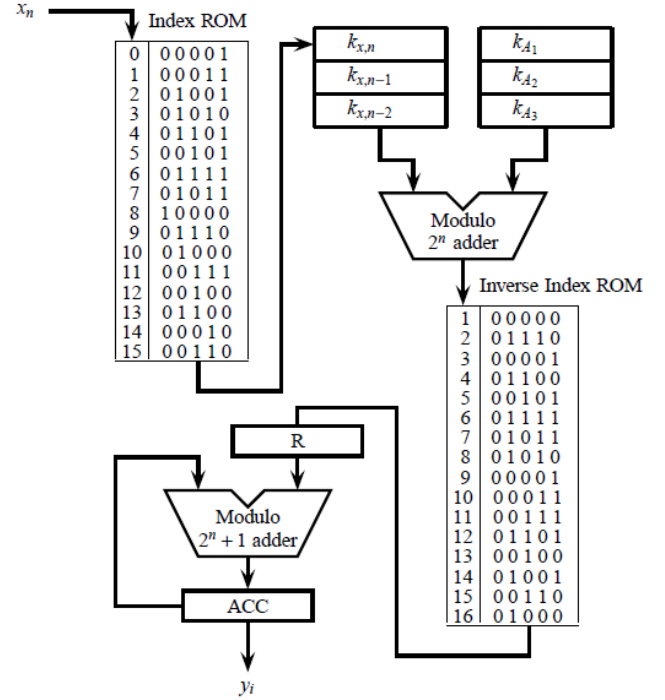

Figure 2. Isomorphic multiplication based Implementation of a 3-tap modulo 17 channel for RNS based FIR Filter.

Product $A_k x_{n-k}$ is transferred into Register R. The modulo $(2^4 + 1)$ adder in the next stage adds the present sum to the previous sum fed back from Register ACC, which is initialized to zero, thus accumulating the summation of the products $A_k x_{n-k}$, over the interval $i = 1, \ldots, N$. The final sum is left in Register ACC.

The architecture shown in figure 2 is also suitable for the modulo $2^8 + 1$ channel of the RNS based FIR filter design. Isomorphing encoded and decoded tables for modulu $(m = 2^8 + 1)$ are given in Appendix.

For example, for the modular multiplication in the GF (17) of the integers $x = 15$ and $y = 16$ the corresponding indices are $k_x = 6$ and $k_y = 8$ respectively, and these can be found in Table 1. Addition modulo 16 is

$$\langle k_x + k_y \rangle_{m-1} = \langle 6 + 8 \rangle_{16} = 14$$

Reverse isomorphic mapping of the index 14 gives product $\langle 15 \times 16 \rangle_{17}$ in the field GF(17) which is equal to 2. Thus

$$\langle 3^{14} \rangle_{17} = \langle 15 \times 16 \rangle_{17} = 2$$

Although theoretically multiplication by zero can not be performed using isomorphing technique, notice that by using used look-ups one can solve the problem by adding an additional code to every ROM.

DISTRIBUTED ARITHMETIC AECHITECTURE

Distributed arithmetic (DA) (NagaJyothi & SriDevi, 2017) is a well known method for the calculation of the sum of products to perform Multiplication and Accumulation (MAC). It is a very common method in many Digital Signal Processing (DSP) Algorithms. It should be noted that the DA method is applicable only to cases where the (MAC) operation involves fixed coefficients.

Let the variable y hold the result of an inner product operation between a integer data vector x_i and a integer coefficient vector A_n, $i = 0, 1, 2, \ldots, N - 1$. The distributed arithmetic representation of the inner modular product operation is as follows:

$$y = \sum_{n=0}^{N-1} A_n x_n \tag{4}$$

where A_n are constant coefficient values (e.g. coefficients of FIR filter) and $x_n = [b_{n,0}, b_{n,1}, \ldots, b_{n,K-1}]$ is the corresponding data vector with N inputs, each binary encoded with bit length of N. Using the standard multiply and accumulate approach, it is obvious that the calculation of this inner product will take N multiply and accumulate execution cycles, corresponding to the number of coefficients used in (4).

Now consider expressing each input in the data vector, x_n, in the unsigned binary number form as

$$x_n = \sum_{k=0}^{K-1} b_{n,k} 2^k, \quad b_{n,k} \in [0.1] \tag{5}$$

where $K - 1$ is binary word lengrth.

The inner product y in (4) can then be written in the form associating it directly with the bit values of the inputs in the data vector

$$y = \sum_{k=0}^{K-1} \left\{ \sum_{n=0}^{N-1} A_n b_{n,k} \right\} 2^k = \sum_{k=0}^{K-1} f(A_n, b_{n,k}) 2^k \tag{6}$$

where

$$f(A_n, b_{n.k}) = \sum_{n=0}^{N-1} A_n b_{n.k} \tag{7}$$

The function (6) contains values representing the sum of products A_n with the individual binary bit value $b_{n.k}$ of the data vector x_n. Since the $b_{n,k}$ bit value is either 0 or 1, while the value of each A_n is constant, there are 2^N possible combination values of $f(A_n, b_{n,k})$.

Applying RNS arithmetic using a moduli set, for example RNS modulo basis is $\mathcal{B} = \{m_1, m_2, \ldots, m_L\}$ where one of them is $m_i = 2^p + 1$, for the inner product in (6), it can be rewritten in terms of its residue m_i, i.e.

$$y_i = \left\langle \sum_{k=0}^{K-1} f(A_n, b_{n,k}) 2^k \right\rangle_{m_i} \tag{8}$$

By applying the algebra of RNS we get follows:

$$y_i = \left\langle \sum_{k=0}^{K-1} f_{m_i}(A_n, b_{n,k}) \langle 2^k \rangle_{m_i} \right\rangle_{m_i} \tag{9}$$

Hence values of $f_{m_i}(A_n, b_{n,k}) = \langle f(A_n, b_{n,k}) \rangle_{m_i}$ can be precomputed and stored in the Look Up Table LUT, which can be subsequently clocked out by using the bit-serial stream of the input vector for the accumulation operation. However each of the value needs to be first scaled with the $\langle 2^n \rangle_{m_i}$ factor, which is difficult to be implemented in hardware due to its modulo operation with respect to modulo m_i.

The evaluation of a polynomial y_i of degree N allows only N multiplications and N additions. This is optimal, since there are polynomials of degree N that cannot be evaluated with fewer arithmetic operations.

$$y_i = \langle f_{m_i}(A_n, b_{n,0}) + f_{m_i}(A_n, b_{n,1}) 2 + f_{m_i}(A_n, b_{n,2}) 2^2 + \cdots$$
$$+ f_{m_i}(A_n, b_{n,K-2}) 2^{K-2} + f_{m_i}(A_n, b_{n,K-1}) 2^{K-1} \rangle_{m_i} \tag{10}$$

Using Horners method for evaluating a polynomial we can rewrite

$$y_i = \langle f_{m_i}(A_n, b_{n,0}) + [f_{m_i}(A_n, b_{n,1}) + [f_{m_i}(A_n, b_{n,2})$$
$$+ [f_{m_i}(A_n, b_{n,3}) + \cdots$$
$$+ [f_{m_i}(A_n, b_{n,K-2}) + f_{m_i}(A_n, b_{n,K-1}) 2] 2] \cdots 2] 2 \rangle_{m_i} \tag{11}$$

The basic distributed arithmetic architecture of a three tap ($N = 3$) FIR filter is shown in Fig. 3. The bank of shift registers in Fig. 1 stores four consecutive input samples. The concatenation of the rightmost bits of the shift registers becomes the address of the LUT. The shift registers are shifted right at every clock cycle. The corresponding LUT entries are also shifted and accumulated N consecutive times where N is the precision of the input data.

Example. Let $N = 3$ and $K = 5$ for $m_i = 17$. Equation (11) is reduced to

$$y_i = f_{17}(A_n, b_{k,0}) + 2 \Big[f_{17}(A_n, b_{k,1}) + 2 \big[f_{17}(A_n, b_{k,2})$$
$$+ 2[f_{17}(A_n, b_{k,3}) + 2[f_{17}(A_n, b_{k,4}) + 0]] \big] \Big] \tag{12}$$

where $[b_{2,4} b_{1,4} b_{0,4}]$ create a memory address which is loaded into the memory address register, and

$$f_{17}(A_n, b_{k,n}) = \sum_{k=0}^{2} \langle A_n b_{k,n} \rangle_{17}, \tag{13}$$

for $n = 0, 1, 2, 3, 4$. For $n = 4$ we have

$$f_{17}(A_n, b_{k,n}) = \langle A_0 b_{0,4} + A_1 b_{1,4} + A_2 b_{2,4} \rangle_{17}$$

The DA of FIR filter consists of the LUT, shift registers and scaling accumulator. The block diagram of a typical distributed arithmetic implementation of the three taps RNS FIR filter for modulo 17 channel is shown in Fig. 3.
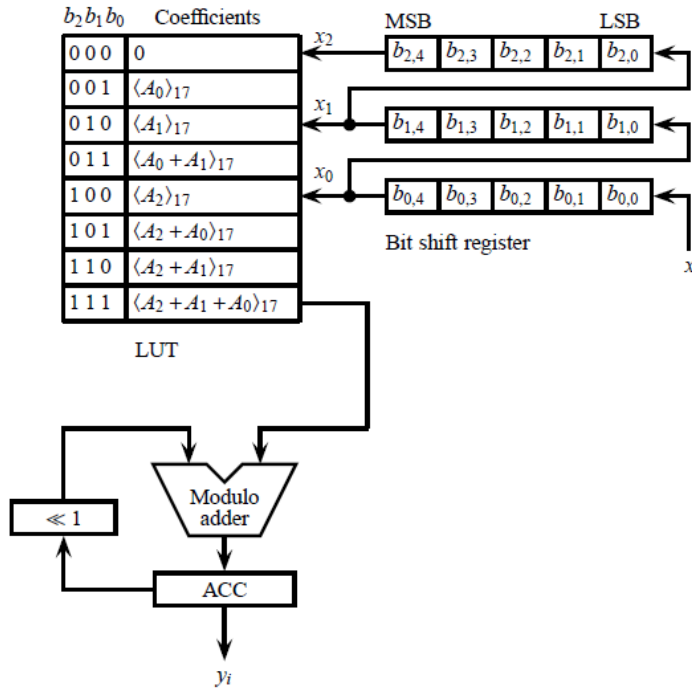
Figure 3. Distributed Arithmetic based Implementation of a 3-tap RNS FIR Filter. Each coefficient has $N = 5$ bits of precision.

We can store data in a look-up table of 2^K words addressed by K-bits. The multiplication by 2 can be implemented with a one-bit shift to the left.

The look-up-table size increases exponentially with the filter coefficients. A smaller number of coefficients can be realized very ealisy with a LUT of a smaller size. When dealing with larger coefficients, they will take up a lot of storage space in the LUT, for implementation and also reduce the calculation speed.

CONCLUSIONS

The proposed algorithm over Galois field GF(m) provides an efficient algorithm for the modulo $2^8 + 1$ multiplication problem. Efficient procedures were proposed to convert the multiplication problem to the addition problem. The proposed algorithm and mapping procedure can be implemented using lookup tables, which means that multiplication in RNS can be computed very fast. The results of this research research can be used to design a general purpose multimoduli ALU.

A modulo multiplier based on the isomorphism technique is compared with those realized as the distributed arithmetic. Isomorphing technique has the following advantages. It does not contain shift registers and memory size is not in the correlation with the FIR filter degree.

APPENDIX

Isomorphic transformation for $m = 2^8 + 1$

Prime number $2^8 + 1 = 257$ is a Fermat number order three and it has 128 primitive roots. The smallest primitive root of modulo 257 is 3, because $\mathrm{ord}_{257}(3) = \varphi(257) = 256$. Acording to Definition 2, $\langle 3^{256} \rangle_{257} = 1$ is calcuated

The Encoder in Table 2 is determined from the mapping $\langle 3^k \rangle_{257}$ for indices $k = 1, 2, \ldots, 256$.

Table 2. The isomorphism encoder table for $m = 257$, and primitive root $g = 3$.

$\langle 3^k \rangle_m$	k	$\langle 3^k \rangle_m$	k	$\langle 3^k \rangle_m$	k	$\langle 3^k \rangle_m$	k
1	0	65	161	129	208	193	160
2	48	66	245	130	209	194	215
3	1	67	100	131	7	195	162
4	96	68	216	132	37	196	10
5	55	69	29	133	210	197	24
6	49	70	188	134	148	198	246
7	85	71	163	135	58	199	14
8	144	72	146	136	8	200	254
9	2	73	44	137	72	201	101
10	103	74	11	138	77	202	123
11	196	75	111	139	38	203	179
12	97	76	221	140	236	204	217
13	106	77	25	141	62	205	74
14	133	78	155	142	211	206	249
15	56	79	22	143	46	207	30
16	192	80	247	144	194	208	42
17	120	81	4	145	149	209	65
18	50	82	67	146	92	210	189
19	125	83	15	147	171	211	204
20	151	84	182	148	59	212	185
21	86	85	175	149	227	213	164
22	244	86	255	150	159	214	79
23	28	87	95	151	9	215	6
24	145	88	84	152	122	216	147
25	110	89	102	153	122	217	71
26	154	90	105	154	73	218	235
27	3	91	191	155	41	219	45
28	181	92	124	156	203	220	91
29	94	93	243	157	78	221	226
30	104	94	109	158	70	222	12
31	242	95	180	159	90	223	40
32	240	96	241	160	39	224	69
33	197	97	167	161	113	225	112
34	168	98	218	162	52	226	114
35	140	99	198	163	237	227	232
36	98	100	206	164	115	228	222
37	219	101	75	165	252	229	53
38	173	102	169	166	63	230	131
39	107	103	201	167	233	231	26
40	199	104	250	168	230	232	238
41	19	105	141	169	212	233	17
42	134	106	137	170	223	234	156
43	207	107	31	171	127	235	116
44	36	108	99	172	47	236	214
45	57	109	187	173	54	237	23
46	76	110	43	174	143	238	253
47	61	111	220	175	195	239	178
48	193	112	21	176	132	240	248
49	170	113	66	177	119	241	64
50	158	114	174	178	150	242	184
51	121	115	83	179	27	243	5
52	202	116	190	180	153	244	234
53	89	117	108	181	93	245	225
54	51	118	166	182	239	246	68
55	251	119	205	183	139	247	231
56	229	120	200	184	172	248	130
57	126	121	136	185	18	249	16
58	142	122	186	186	35	250	213
59	118	123	20	187	60	251	177
60	152	124	82	188	157	252	183
61	138	125	165	189	88	253	224
62	34	126	135	190	228	254	129
63	87	127	81	191	117	255	176
64	32	128	80	192	33	256	128

Table 3. The isomorphism decoder table for $m = 257$, and primitive root $g = 3$.

k	$\langle 3^k\rangle_m$	k	$\langle 3^k\rangle_m$	k	$\langle 3^k\rangle_m$	k	$\langle 3^k\rangle_m$
0	1	64	241	128	256	192	16
1	3	65	209	129	254	193	48
3	27	67	82	131	230	195	175
4	81	68	246	132	176	196	11
5	243	69	224	133	14	197	33
6	215	70	158	134	42	198	99
7	131	71	217	135	126	199	40
8	136	72	137	136	121	200	120
9	151	73	154	137	106	201	103
10	196	74	205	138	61	202	52
11	74	75	101	139	183	203	156
12	222	76	46	140	35	204	211
13	152	77	138	141	105	205	119
14	199	78	157	142	58	206	100
15	83	79	214	143	174	207	43
16	249	80	128	144	8	208	129
17	233	81	127	145	24	209	130
18	185	82	124	146	72	210	133
19	41	83	115	147	216	211	142
20	123	84	88	148	134	212	169
21	112	85	7	149	145	213	250
22	79	86	21	150	178	214	236
23	237	87	63	151	20	215	194
24	197	88	189	152	60	216	68
25	77	89	53	153	180	217	204
26	231	90	159	154	26	218	98
27	179	91	220	155	78	219	37
28	23	92	146	156	234	220	111
29	69	93	181	157	188	221	76
30	207	94	29	158	50	222	228
31	107	95	87	159	150	223	170
32	64	96	4	160	193	224	253
33	192	97	12	161	65	225	245
34	62	98	36	162	195	226	221
35	186	99	108	163	71	227	149
36	44	100	67	164	213	228	190
37	132	101	201	165	125	229	56
38	139	102	89	166	118	230	168
39	160	103	10	167	97	231	247
40	223	104	30	168	34	232	227
41	155	105	90	169	102	233	167
42	208	106	13	170	49	234	244
43	110	107	39	171	147	235	218
44	73	108	117	172	184	236	140
45	219	109	94	173	38	237	163
46	143	110	25	174	114	238	232
47	172	111	75	175	85	239	182
48	2	112	225	176	255	240	32
49	6	113	161	177	251	241	96
50	18	114	226	178	239	242	31
51	54	115	164	179	203	243	93
52	162	116	235	180	95	244	22
53	229	117	191	181	28	245	66
54	173	118	59	182	84	246	198
55	5	119	177	183	252	247	80
56	15	120	17	184	242	248	240
57	45	121	51	185	212	249	206
58	135	122	153	186	122	250	104
59	148	123	202	187	109	251	55
60	187	124	92	188	70	252	165
61	47	125	19	189	210	253	238
62	141	126	57	190	116	254	200
63	166	127	171	191	91	255	86

Consider the modulo multiplication of integers $X = 100$ and $Y = 234$ using modulo $m = 257$. Using Table 2, the index codes for $X = 100$ and $Y = 234$ are $k_x = 206$ and $k_y = 156$ respectively. The indices k_x and k_y are binary added modulo $m_1 = 256$, giving a result of 106. Since modulo m_1 has the form 2^8, addition modulo 2^8 is very simple. This is obtaind as the remainder of the division of sum by 2^8.

$$
\begin{array}{cccccccccc}
 & 1 & 1 & 0 & 0 & 1 & 1 & 1 & 0 & \quad k_x = 206 \\
+ & 1 & 0 & 0 & 1 & 1 & 1 & 0 & 0 & \quad k_y = 156 \\
\leftarrow \boxed{1} & 0 & 1 & 1 & 0 & 1 & 0 & 1 & 0 & \quad \langle k_x + k_y\rangle_{256} = 106
\end{array}
$$

This represents the final product of 13 that is given in Table 3. It can easily verified that $\langle 100 \times 234\rangle_{257} = 13$. The scheme in Fig. 1 should be completed by a few gates to detect when one of the two operands is zero (no corresponding index in the isomorphism). When a zero is detected, the product is set to zero. Because isomorphic multipliers use modular adders in combination with two isomorphic tables, the modular adder in Fig. 1 should be replaced by a binary adder and incorporated in the inverse isomorphic mapping table. The resulting scheme will be faster and consumes less power, as detailed in (Nannarelli et al., 2003).

REFERENCES

Chen, G., Bai, G., & Chen, H. (2007). A New Systolic Architecture for Modular Division. IEEE Transactions on Computers, 56(2), pp. 282-286. doi:10.1109/tc.2007.20

Chen, R. J., Fan, J. W., & Liao, C. H. (2014). Reconfigurable Galois Field multiplier. In 2014 International Symposium on Biometrics and Security Technologies (ISBAST). Institute of Electrical and Electronics Engineers (IEEE)., pp. 112-115. doi:10.1109/isbast.2014.7013104

Jullien, G. A. (1980). Implementation of Multiplication, Modulo a Prime Number, with Applications to Number Theoretic Transforms. IEEE Transactions on Computers, C-29(10), pp. 899-905. doi:10.1109/tc.1980.1675473

Kitsos, P., Theodoridis, G., & Koufopavlou, O. (2003). Theodoridis, G., & Koufopavlou, O. 2003. An efficient reconfigurable multiplier architecture for Galois field GF(2m). Microelectronics Journal, 34(10), pp. 975-980. doi:10.1016/s0026-2692(03)00172-1

NagaJyothi, G. & SriDevi, S. (2017). Distributed arithmetic architectures for FIR filters-A comparative review. In 2017 International Conference on Wireless Communications, Signal Processing and Networking (WiSPNET). Institute of Electrical and Electronics Engineers (IEEE)., pp. 2684-2690. doi:10.1109/wispnet.2017.8300250

Nannarelli, A., Cardarilli, G. C., & Re, M. (2003). Power-delay tradeoffs in residue number system. In Proceedings of the 2003 International Symposium on Circuits and Systems, 2003. ISCAS '03..Institute of Electrical and Electronics Engineers (IEEE)., pp. 413-416. doi:10.1109/iscas.2003.1206300

Padmavathy, R. & Bhagvati, C. (2012). Discrete logarithm problem using index calculus method. Mathematical and Computer Modelling, 55(1-2), pp. 161-169. doi:10.1016/j.mcm.2011.02.022

Pradhan, D. K. (1978). A Theory of Galois Switching Functions. IEEE Transactions on Computers, C-27(3), pp. 239-248. doi:10.1109/tc.1978.1675077

Qi, H., Kim, Y. B., & Choi, M. (2012). A high speed low power modulo 2n + 1 multiplier design using carbon-nanotube technology. In 2012 IEEE 55th International Midwest Symposium on Circuits and Systems (MWSCAS). Institute of Electrical and Electronics Engineers (IEEE)., pp. 406-409. doi:10.1109/mwscas.2012.6292043

EFFECT OF THE CASCADE NEUTRALIZATION ENERGY ON THE SURFACE MODIFICATION BY THE IMPACT OF SLOW HIGHLY CHARGED IONS

MILENA MAJKIC[1,*]**, NATAŠA NEDELJKOVIĆ**[2]**, MARKO MIRKOVIĆ**[3]

[1]Faculty of Technical Sciences, University of Priština, Kosovska Mitrovica, Serbia
[2]Faculty of Physics, University of Belgrade, Belgrade, Serbia
[3]University College of Civil Engineering and Geodesy, Belgrade, Serbia

ABSTRACT

We consider the neutralization dynamics of slow highly charged ions in the interaction with a metal surface covered with a thin dielectric film from the standpoint of the surface modification. The quasi-resonant two-state vector model and the micro staircase model are used for the calculation of cascade neutralization energy for the Ar^{Z+}, Kr^{Z+} and Xe^{Z+} ions. The population of several ionic Rydberg states at each step of the neutralization cascade is demonstrated. The correlation between the neutralization and the potential energy is presented for moderate and very low ionic velocities and the relevance of this relation for the surface nanostructure formation is briefly discussed for a different angle of incidence and different dielectric materials.

Keywords: Metal - dielectric surface, Highly charged ions, TVM, Rydberg states, Collision geometry, Neutralization energy, Surface nanostructures.

INTRODUCTION

Detailed study of the interaction of slow highly charged ions (HCI) with solid surfaces is of great interest for the analysis of the surface modification by their individual impact (Nedeljković et al., 2016). Depending on the ionic velocity and on the type of the solid surface, different surface structures (features) can be created (Aumayr et al., 2011; El-Said et al., 2008, 2016). During the ion-surface interaction, the electrons from the surface are captured into the intermediate ionic Rydberg states, which results in the neutralization cascade. The cascade neutralization energy has an important role in the surface modification, i.e., in the formation of different types of the surface nanostructures (Majkić et al., 2017). That is, the size of the created features is in a direct correlation with the ionic neutralization energy. For very low ionic velocity the size of the formed surface nanostructures is directly proportional to the ionic potential energy; for example, the pit volume is proportional to the potential energy of the Xe^{Z+} ions interacting with KBr (Heller et al., 2008). However, for moderate ionic velocities, the surface modification is governed by the ionic neutralization energy which is less than the potential energy due to the incomplete neutralization. In that case, both the neutralization and the deposited kinetic energy contribute to the surface modification (Majkić et al., 2017, 2019).

The aim of the present article is twofold. The first aim is to correlate the neutralization and the potential energy of the HCI impinging upon a metal surface covered with a thin dielectric film for different collision geometry and film properties.The neutralization process will be considered within the quasi-resonant two-state

vector model (TVM) for the population probabilities of the ionic intermediate Rydberg states and the micro staircase model for the multielectron neutralization. From the final ionic charge estimated quantum-mechanically within the proposed models, we directly obtain the required neutralization energy, the quantity necessary for the nanostructure formation. For the sake of simplicity, first we calculate the neutralization energy in the absence of dielectric film (metal-vacuum MV-system). The cascade neutralization energy, in the presence of dielectric film (metal-dielectric-vacuum, MDV-system), we calculate by using the principle of equivalence (Majkić et al., 2017), which correlates the quantities in the MV- and the MDV-system via the concept of the effective core charge. The second aim is an analysis of the role of the cascade neutralization energy in the surface modification. That is, we correlate the size of the formed surface nanostructures and the obtained neutralization energy. The correlation of that type has been obtained between the size and the potential energy for the very low ionic velocities (Aumayr et al., 2011; El-Said et al., 2010, 2016).

This article is organized as follows. First, we present the TVM for the calculation of the population probabilities for the Ar^{Z+}, Kr^{Z+} and Xe^{Z+} ions. Applying the micro staircase model we calculate the neutralization energy of these ions within the MDV-system. In the subsequent analysis, we consider the correlation between the neutralization and the potential energy for Xe^{Z+}, for different angle of incidence and different material of the dielectric film. We analyze the obtained correlation for Ar^{Z+}, Kr^{Z+} and Xe^{Z+} ions for two characteristic ionic velocities and discuss the corresponding relation between the surface nanostructure size and the

---

* Corresponding author: milena.majkic@pr.ac.rs

obtained neutralization energy. Atomic units ($e^2 = \hbar = m_e = 1$) will be used throughout the paper unless indicated otherwise.

NEUTRALIZATION DYNAMICS OF THE HCI IN THE MDV-SYSTEM

We consider the HCI with initial charge $Z \gg 1$ approaching a metal surface covered with a thin dielectric film at velocity v. Two velocity regions will be considered: the moderate velocity case ($v = 0.25$ a.u.), characteristic for the crater formation within the MDV-system (Lake et al., 2011), and the very low velocity case ($v = 0.1$ a.u.) characteristic for the hillocks created in the interaction of HCI with HOPG-surface (Aumayr et al., 2011). For the metal surface parameters, within the Sommerfeld model, we use the value of the work function $\phi = 5$eV and for the potential depth $U_0 = 15$eV. The dielectric film is characterized by the width s_0, and by the dielectric constants $\epsilon = 2, 4$ and 8.We analyze the arbitrary collision geometry for the angles of incidence $\Phi_{in} = \pi/2, 3\pi/8$ and $\pi/4$.Due to the interaction of the HCI with solid surface the ionic charge decreases in time according to the cascade neutralization scenario $Q = Z \rightarrow Z - 1 \rightarrow .... \rightarrow Q_{\text{fin}}$, see Fig. (1).
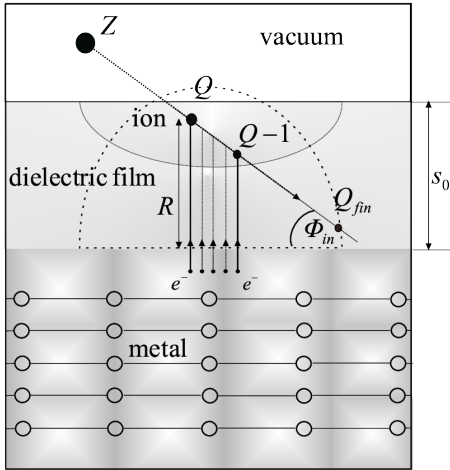
Figure 1. Cascade neutralization of the HCI in the MDV-system and the formation of the nanocrater; the hillock formation is presented by dashed line, schematically.

The neutralization process in the MDV-system we treat within the framework of the TVM and micro-staircase model (Majkić et al., 2017, 2019). According to the TVM the state of the active electron e^- is described by two state vectors $|\Psi_1(t)\rangle$ and $|\Psi_2(t)\rangle$, which simultaneously evolve in two opposite directions of time. The first state evolves from the initial state $|\Psi_1(t_{in})\rangle$ (electron in metal) towards the future, and the second state evolves towards the fixed final state $|\Psi_2(t_{fin})\rangle$ (electron captured by the ion). The states of the active electron at the time t (at ion-surface distance R) between the initial time t_{in} and the final time t_{fin} are expressed via intermediate eigenstates $|\mu_M(R)\rangle$ and $|\nu_A(R)\rangle$ of the in-Hamiltonian $\hat{H}_1(R)$ and the out-Hamiltonian $\hat{H}_2(R)$, respectively (Nedeljković et al., 2012; Nedeljković et al., 2016). By the ap-

propriate expressions of the Hamiltonians $\hat{H}_1(R)$ and $\hat{H}_2(R)$ we take into account the polarization of the metal surface and the polarization of the ionic core, respectively, as well as the effect of the dielectric film (Majkić et al., 2017). The corresponding eigenenergies are $E_M = -\gamma_M^2/2$ (γ_M is the continous energy parameter) and $E_A = -\gamma_A^2(R)/2 = -\tilde{\gamma}_A^2/2 + (2Z - 1)/4R$, where $-\tilde{\gamma}_A^2/2$ is the eigenenergy of the atomic Hamiltonian. The effect of the arbitrary collision geometry is taken into account by the Galilean invariance, i.e. by the translation factor in the function $|\Psi_2(t)\rangle$ (Nedeljković et al., 2012; Nedeljković et al., 2016) expressed via perpendicular velocity component $v_\perp$, and the energy shift $E_M \rightarrow E_M' = -\gamma_M'^2/2$ in the function $|\Psi_1(t)\rangle$, which depends on the parallel velocity component $v_\parallel$.

The population probability of the ionic intermediate Rydberg state within the MDV-system is governed by the corresponding quantity in the MV-system. In that case we use the relation between the transition probability density $T_{\mu_M',\nu_A}(t)$ and the mixed flux $I_{\mu_M',\nu_A}(t)$, the main quantity within the TVM:

$$T_{\mu_M',\nu_A}(t) = \left| \int_{t_{in}}^{t} I_{\mu_M,\nu_A}(t)dt \right|^2. \tag{1}$$

The mixed flux we calculate through the fictive Firsov plane S_F (Demkov & Ostrovskii, 1975; Nedeljković & Majkić, 2007), which separates the metal surface and the ionic region. The S_F plane is positioned sufficiently far both from the surface and on the ionic core so that we use the asymptotic expressions of the wavefunctions $\Psi_1(\mathbf{r}, t)$ and $\Psi_2(\mathbf{r}, t)$ for the calculation of the mixed flux (Nedeljković et al., 2012). For an arbitrary collision geometry and moderate ionic velocities the electrons are captured quasi-resonantly from the overall metallic states $|\mu_M\rangle$ into the ionic Rydberg state $|\nu_A\rangle$ through the potential barrier formed between the surface and the ionic core. For very low ionic velocities the population process is resonant. In the more general velocity case, the intermediate population probability is given by $P_{\nu_A}(R) = 1 - \exp\left[-T_{\nu_A}(t)\right]$ (Nedeljković et al., 2016), where $T_{\nu_A}(t)$ is calculated by the integration of the transition probability density $T_{\mu_M',\nu_A}(t)$ (Nedeljković et al., 2012):

$$T_{\nu_A}(t) = 2\pi\mathcal{E}(R; v_\parallel, v_\perp)T_{\nu_A}^{(0)} \frac{v_\perp}{\gamma_A|\tilde{\beta}|}\langle f\rangle_{\Omega_{\mathbf{k}'}}$$

$$\times f_\gamma(\gamma_M')\left[\gamma_M' + \gamma_A(R)\right]^2\left(1 + \frac{2\tilde{\alpha}}{\tilde{\beta}}\frac{1}{R}\right)R^{2\tilde{\alpha}}e^{-2\tilde{\beta}R}. \tag{2}$$

All quantities in (2) are defined for the quasi-resonant electron transitions, i.e. at ion-surface distance R we have $\gamma_M' = \gamma_A(R)$; the influence of the energy levels with $\gamma_M' \neq \gamma_A(R)$ is expressed via $\mathcal{E}$ (Nedeljković et al., 2016). The quantity $\langle f\rangle_{\Omega_{\mathbf{k}'}}$ represents the angle-averaged Fermi-Dirac distribution of the electron momenta in solid (Nedeljković et al., 2012). The parameters $\tilde{\alpha}$ and $\tilde{\beta}$ in (2) are defined by $\tilde{\alpha} = Z/\tilde{\gamma}_A - 1/2 + 1/4\gamma_M'$ and $\tilde{\beta} = \gamma_M' + (\tilde{\gamma}_A - \gamma_M')/2$, respectively. The explicit expressions for the factors $T_{\nu_A}^{(0)}$ and $f_\gamma(\gamma_M')$ are given in (Nedeljković et al., 2012).

Within the framework of the micro-staircase model, characteristic for the moderate ionic velocity (Nedeljković et al., 2016),

the neutralization of the ion of the initial charge Z and intermediate core charge Q, occurs through the neutralization cascades (macro-steps), which consist of the appropriate micro-cascades. The Rydberg levels with principal quantum numbers $n_A = n_Z - j + 1$ of the particular micro-cascade (core charge Q) are populated with probabilities $P^{(Q,j)} \equiv \mathcal{P}_{n_A} = 2 \sum_{l_A, m_A} P_{\nu_A}^{\max}$. For the probability $P_{\nu_A}^{\max}$ we take the maximal value of the population probability $P_{\nu_A}(R)$ at the neutralization distance $R = R_c^N \equiv R_c^{Q,j}$ ($j \in [j_{\min}^{(Q)}, j_{\max}^{(Q)}]$). The neutralization cascade $Q \to Q - 1$, see Fig. (1), can be expressed by the following scheme (Nedeljković et al., 2016):

$$Q \to \quad Q - P^{(Q,j_{\min}^{(Q)})} \to$$
$$Q - \left[P^{(Q,j_{\min}^{(Q)})} + P^{(Q,j_{\min}^{(Q)}+1)} \right] \dots \to$$
$$Q - \sum_{j=j_{\min}^{(Q)}}^{j_{\max}^{(Q)}} P^{(Q,j)} \approx Q - 1. \tag{3}$$

For very low velocity case the fine structure of the population process vanishes. Each macro cascade consists of only one micro step (staircase model) (Nedeljković et al., 2012).
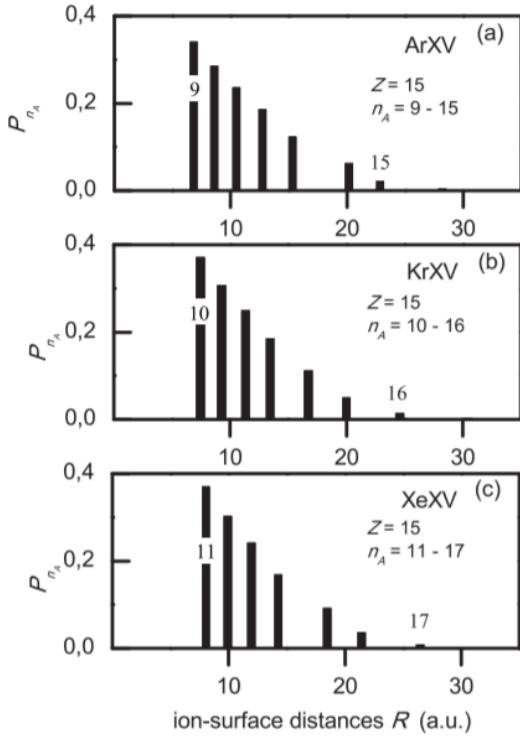
Figure 2. The first step of the cascade neutralization for Ar^{Z+}, Kr^{Z+} and Xe^{Z+} ions in the MV-system.

In Fig. (2) we present the first step $Q = Z \to Q = Z - 1$ of the neutralization cascade within the MV-system of the ArXV, KrXV and XeXV ions ($Z = 15$) approaching a metal surface at velocity $v = 0.25$ a.u. for $\Phi_{in} = \pi/2$. The considered step consists of the population of the series of Rydberg levels n_A with probabilities $\mathcal{P}_{n_A}$ at neutralization distances $R = R_c^N$. In the considered case the Rydberg levels with principal quantum numbers from $n_A = 15$ to $n_A = 9$ for ArXV, $n_A = 16$ to $n_A = 10$ for KrXV and $n_A = 17$

to $n_A = 11$ for XeXV are populated before other available levels, with $\sum \mathcal{P}_{n_A} \approx 1$. For the same ionic charge $Z = 15$, different Rydberg levels of these ions are populated in each particular step, but at nearly the same ion-surface distances R_c^N with the same population probability maxima, compare the neutralization distances for $n_A = 9, 10$ and 11 in Fig. (2) (a), (b) and (c), respectively. In the next macro neutralization step ($Q = Z - 1 \to Q = Z - 2$), not presented in figure, the population dynamics is similar to those presented in Fig. (2), but the number of populated levels decreases, because each successive macro step begins after the previous step ends, see figure 6 in (Nedeljković et al., 2016).

The neutralization dynamics within the MDV-system can be obtained from the corresponding one in the MV-system using the principle of equivalence based on the concept of the effective ionic charge Z_{eff} (Majkić et al., 2017, 2019).

RELATION BETWEEN THE CASCADE NEUTRALIZATION ENERGY AND THE POTENTIAL ENERGY AND THEIR ROLE IN THE SURFACE MODIFICATION

The neutralization energy we compute by using the relation established for the MV-system: $W^{(Z,MV)} = W_{Z,pot} - W_{Q_{fin}^{MV},pot}$, where the first term $W_{Z,pot}$ represents the potential energy at the initial stages of the ionic trajectory, and the second term describes the potential energy at the last macro step of the neutralization cascade in front of the surface. The neutralization energy $W^{(Z,MDV)}$ in the MDV-system can be obtained from the corresponding quantities in MV-system according to the relation

$$W^{(Z,MDV)} = W^{(Z_{eff},MV)}, \tag{4}$$

where the effective ionic charge Z_{eff} is calculated in (Majkić et al., 2017) for a given film properties (ϵ, s_0). We note that the final ionic charges for different geometries in the MV-system are the same due to the behaviour of the population probabilities maxima (see Fig. (2) and Fig.2 in (Majkić et al., 2019). The corresponding neutralization energies differ due to the difference in their potential energies.

The neutralization energy $W^{(Z,MDV)}$ obtained during the neutralization process $Z \to Q_{fin}$ is deposited into the surface. It represents the necessary amount of the energy for the nanofeatures formation. The surface modification simultaneously occurs with the proposed cascade neutralization of the ions. Consequently, the dielectric film is strongly perturbed and the corresponding dielectric constant ϵ is significantly lower in comparison to the unperturbed dielectric case.

The experimental results concerning the nanostructure formation by the impact of individual HCI are available for the very low ionic velocities and different types of surfaces and for the moderate velocities and the MDV-system. The experiments of the first class show the dependence of the size of the formed nanostructures on the HCI⸱s potential energy. The impact of the HCI on different materials such as alkali and alkaline earth halides, polymers, oxides, HOPG, etc. has been studied (Aumayr et al.,

2011). For these experiments it is characteristic that the neutralization process is complete, i.e. $Q_{fin}^{MV} = 0$ and $W^{(Z,MV)} = W_{Z,pot}$. For moderate ionic velocity, within the MDV-system as it has been obtained in experiments (Lake et al., 2011)), the neutralization is incomplete. For that reason, the corresponding neutralization energy differs from the ionic potential energy. It motivates us to correlate the neutralization and the potential energies of the ions.
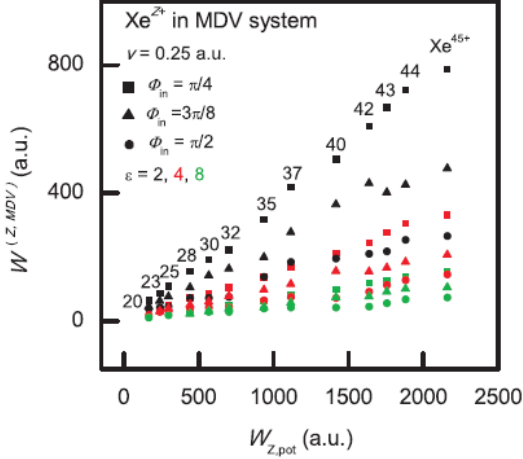

Figure 3. Neutralization energy $W^{(Z,MDV)}$ via initial potential energy $W_{Z,pot}$ of the Xe^{Z+} ions impinging at velocity $v = 0.25$ a.u. upon a metal surface ($\phi = 5$ eV, $U_0 = 15$ eV) covered with a thin dielectric film ($\epsilon = 2, 4$ and 8) of width $s_0 = 27$ a.u., for the angles of incidence $\Phi_{in} = \pi/2, 3\pi/8$ and $\pi/4$.

In Fig. (3) we present the cascade neutralization energy via initial potential energy for the Xe^{Z+} ions interacting with metal surface covered with a thin dielectric film for different collision geometries and different dielectric materials (dielectric constants $\epsilon = 2, 4$, and 8). We consider three angles of incidence $\Phi_{in} = \pi/2, 3\pi/8$ and $\pi/4$. From Fig. (3) we can conclude that the neutralization energy depends on the combinations Φ_{in} and ϵ. The same amount of the neutralization energy can be achieved with appropriate combination of these parameters; for example for $Z = 40$ the same energy is for $\Phi_{in} = 3\pi/8$ and $\epsilon = 8$ and $\Phi_{in} = \pi/2$ and $\epsilon = 4$. The highest core charge Xe^{45+} has the highest neutralization energy for $\Phi_{in} = \pi/4$ and $\epsilon = 2$, which corresponds to the highly perturbed dielectric. Having in mind that the formation of the particular surface nanostructure is determined by the available neutralization energy, we conclude that the nanostructure of the desired size can be obtained depending on the collision geometry and the surface type (ϵ).

In Fig. (4) we plot the neutralization energy via initial potential energy for the Ar^{Z+}, Kr^{Z+} and Xe^{Z+} ions for two velocities $v = 0.25$ a.u. and $v = 0.1$ a.u. For the ionic velocity $v = 0.25$ a.u. we consider the angle of incidence $\Phi_{in} = \pi/4$ and dielectric film of dielectric constants $\epsilon = 2$. In the case $v = 0.1$ a.u. we consider the neutralization energy in the absence of dielectric film ($\epsilon = 1$). The corresponding neutralization energy coincides with the ionic potential energy. From Fig. (4) we recog-
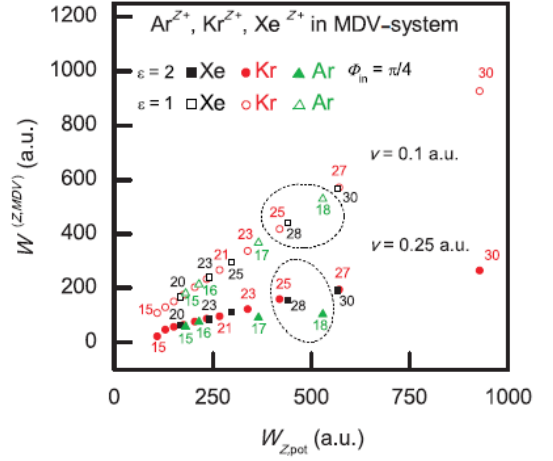

Figure 4. Neutralization energy $W^{(Z,MDV)}$ via initial potential energy $W_{Z,pot}$ of the Ar^{Z+}, Kr^{Z+} and Xe^{Z+} ions impinging at velocity $v = 0.25$ a.u. upon a metal surface ($\phi = 5$ eV, $U_0 = 15$ eV) covered with a thin dielectric film of width $s_0 = 27$ a.u. and $\epsilon = 2$ for the angle of incidence $\Phi_{in} = \pi/4$, and for $v = 0.1$ a.u. and $\epsilon = 1$.

nize the effect of the ionic velocity; for example, for $v = 0.25$ a.u. $W(Ar^{18+}) < W(Kr^{25+}) \approx W(Xe^{28+})$, while for $v = 0.1$ a.u $W(Ar^{18+}) > W(Kr^{25+}) \approx W(Xe^{28+})$. This circumstance allows us to connect the neutralization energy to the size of the surface nanostructrues. For very slow ionic projectile when the potential energy plays a decisive role in the surface modification, the largest nanofeatures can be fabricated by the Ar^{18+} in comparison with the Kr^{25+} and Xe^{28+} ions. For slow, but moderate ionic velocity ($v = 0.25$ a.u.), the neutralization energy together with the deposited kinetic energy influence to the nanostructure formation. In that case, the Kr^{25+} and the Xe^{28+} ions will create the nanostructures of larger size in comparison to the Ar^{18+} ions.

In Fig. 5 we present the dependence of the cascade neutralization energy on the potential energy for Xe^{Z+} ions impinging a metal surface covered with a thin dielectric film of width $s_0 = 27$ a.u. for two characteristic ionic velocities. We consider the very low ionic velocity $v = 0.1$ a.u. case for the system parameters $(\Phi_{in}, \epsilon) = (\pi/2, 1)$, Fig. 5 (a), and the moderate ionic velocity $v = 0.25$ a.u. case for the system parameters $(\Phi_{in}, \epsilon) = (\pi/2, 2)$, Fig. 5 (b) (Majkić et al., 2019). In Figs. 5 (a) and (b), as an inset, we present the experimental results for the hillock diameter r within the HOPG-surface ((Aumayr et al., 2011)), and the crater depth d for the system Co+Al_2O_3 ((Lake et al., 2011)), respectively, obtained for the two considered velocities. Nanostructure sizes are presented in atomic units: atomic unit length = 0.0529 nm.

From Fig. 5 we see the similar linear dependence of the neutralization energy $W^{(Z,MDV)}$ on the potential energy $W_{Z,pot}$ and the surface nanostucture sizes r and d expressed via $W_{Z,pot}$. According to the observed functional dependencies we conclude that the neutralization energy crucially determines the size of the created surface features (craters and hillocks). We note that the contribu-
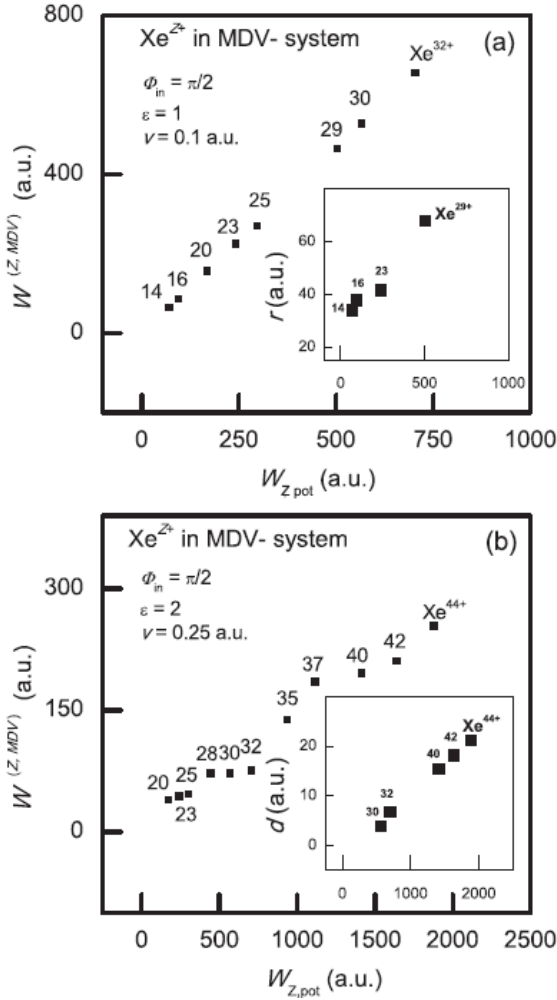
Figure 5. Neutralization energy $W^{(Z,MDV)}$ via potential energy $W_{Z,pot}$ for Xe^{Z+} ion for $\Phi_{in} = \pi/2$. (a) Velocity $v = 0.1$ a.u. and $\epsilon = 1$; Inset: hillock diameter r obtained experimentally (Aumayr et al., 2011) within HOPG system. (b) Velocity $v = 0.25$ a.u. and $\epsilon = 2$; Inset: crater depth d obtained experimentally (Lake et al., 2011) within the $Co+Al_2O_3$.

tion of the neutralization energy in the surface modification depends on the ionic velocity; for very low ionic velocities neutralization energy $W^{(Z,MDV)} \approx W_{Z,pot}$ directly governed the surface features size, while for the moderate ionic velocities the quantity $W^{(Z,MDV)} < W_{Z,pot}$ represents only the part of the deposited energy necessary for the considered nanostructure formation. The effect of the neutralization energy in the surface modification also depends on the surface type and the collision geometry.

CONCLUDING REMARKS

In this paper, for the first time, we presented the detailed analysis of the relation between the cascade neutralization energy $W^{(Z,MDV)}$ and the initial potential energy $W_{Z,pot}$ of the HCI (charge Z) impinging upon a metal surface covered with a thin dielectric film for arbitrary collision geometry and film properties. We consider the Ar^{Z+}, Kr^{Z+} and Xe^{Z+} ions for dielectric constants $\epsilon = 2, 4$

and 8, and for three different angles of incidence $\Phi_{in} = \pi/2, 3\pi/8$ and $\pi/4$. By the impact of the individual HCI upon a surface the nanostuctures (craters and hillocks) are created. We discussed the role of the cascade neutralization energy for the surface modification.

From the similarity of the obtained linear dependence between the quantities $W^{(Z,MDV)}$ and $W_{Z,pot}$ and the corresponding experimental relation between the size of the nanostructures and the potential energy, we conclude that the nanostructure sizes are directly governed by the cascade neutralization energy. Concerning the influence of the projectile velocity on the cascade neutralization energy, we demonstrated the velocity dependence of the effect of the neutralization energy on the surface modification. For very low ionic velocity characteristic for the complete neutralization, the potential energy has the main role in the creation of the surface nanofeatures. For low, but moderate ionic velocity, the cascade neutralization energy, which is less than the potential energy due to incomplete neutralization, plays a decisive role in the surface modification.

REFERENCES

Aumayr, F., Facsko, S., El-Said, A. S., Trautmann, C., & Schleberger, M. 2011. Single ion induced surface nanostructures: a comparison between slow highly charged and swift heavy ions. Journal of Physics: Condensed Matter, 23(39), p. 393001. doi:10.1088/0953-8984/23/39/393001.

Demkov, Y. N. & Ostrovskii, V. N. 1975. Zh. Eksp. Teor. Fiz, 69, pp. 1582.

El-Said, A. S., Heller, R., Aumayr, F., & Facsko, S. 2010. Pyramidal pits created by single highly charged ions in BaF 2 single crystals. Physical Review B, 82(3). doi:10.1103/physrevb.82.033403.

El-Said, A. S., Wilhelm, R. A., Heller, R., et al. 2008. Creation of Nanohillocks on CaF 2 Surfaces by Single Slow Highly Charged Ions. Physical Review Letters, 100(23). doi:10.1103/physrevlett.100.237601.

El-Said, A. S., Wilhelm, R. A., Heller, R., et al. 2016. Tuning the Fabrication of Nanostructures by Low-Energy Highly Charged Ions. Physical Review Letters, 117(12). doi:10.1103/physrevlett.117.126101.

Heller, R., Facsko, S., Wilhelm, R. A., & Möller, W. 2008. Defect Mediated Desorption of the KBr(001) Surface Induced by Single Highly Charged Ion Impact. Physical Review Letters, 101(9). doi:10.1103/physrevlett.101.096102.

Lake, R., Pomeroy, J. M., Grube, H., & Sosolik, C. E. 2011. Charge State Dependent Energy Deposition by Ion Impact. Physical Review Letters, 107(6). doi:10.1103/physrevlett.107.063202.

Majkić, M. D., Nedeljković, N. N., & Dojčilović, R. J. 2017. Interaction of slow highly charged ions with a metal surface covered with a thin dielectric film. The role of the neutralization energy in the nanostructures formation. Materials Research Express, 4(9), p. 95027. doi:10.1088/2053-1591/aa8bc7.

Majkić, M. D., Nedeljković, N. N., & Mirković, M. A. 2019. Neutralization energy contribution to the nanostructure creation by the impact of highly charged ions at arbitrary angle of incidence upon a metal surface covered with a thin dielectric film. Vacuum, 165, pp. 62-67. doi:10.1016/j.vacuum.2019.04.002.

Nedeljković, N. N. & Majkić, M. D. 2007. Intermediate stages of the Rydberg-level population of multiply charged ions escaping solid surfaces. Physical Review A, 76(4). doi:10.1103/physreva.76.042902.

Nedeljković, N. N., Majkić, M. D., Božanić, D. K., & Dojčilović, R. J. 2016. Dynamics of the Rydberg state population of slow highly charged ions impinging a solid surface at arbitrary collision geometry. Journal of Physics B: Atomic, Molecular and Optical Physics, 49(12), p. 125201. doi:10.1088/0953-4075/49/12/125201.

Nedeljković, N. N., Majkić, M. D., & Galijaš, S. M. D. 2012. Grazing incidence collisions of multiply charged ions on solid surfaces. Influence of the formation of intermediate Rydberg states. Journal of Physics B: Atomic, Molecular and Optical Physics, 45(21), p. 215202. doi:10.1088/0953-4075/45/21/215202.

UNCONDITIONALLY POSITIVE FINITE DIFFERENCE AND STANDARD EXPLICIT FINITE DIFFERENCE SCHEMES FOR POWER FLOW EQUATION

BRANKO DRLJAČA[1*], SVETISLAV SAVOVIĆ[2]

[1]Faculty of Sciences, University of Priština, Kosovska Mitrovica, Serbia
[2]Faculty of Sciences, University of Kragujevac, Kragujevac, Serbia

ABSTRACT

Power flow equation for step-index glass optical fiber was solved using recently reported unconditionally-positive finite difference (UPFD) scheme. Solution obtained using UPFD scheme was compared with solution obtained using standard explicit finite difference (EFD) scheme. For accuracy testing both schemes were compared with analytical solution for steady state distribution of given fiber. The advantage of UPFD is reflected in stability of the scheme regardless of discretization step taken. Nevertheless EFD scheme has better concurrence with analytical solution than UPFD. This is due to the additional truncation-error terms in the approximations of the first and second derivatives with respect to θ.

Keywords: Parabolic equation, Numerical schemes, Step index optical fiber.

INTRODUCTION

Partial differential equations are used to model a wide variety of problems in natural sciences. Usually those are physical, chemical, biological and engineering problems such as transmission of light through optical fibers, heat transfer, transport and reaction of chemical species, solid state physics, adsorption of pollutants in soil and diffusion of radon and neutrons (Bear et al., 2007; Hetrick, 1971; Kevkic et al., 2019; Murray, 2002; Petrović, 2017; Shih, 1984). Often those equations are parabolic differential equations with no, or limited, analytical solution and their solvation requires various numerical techniques (Djordjevich 2013; Savović et al., 2009; Savović et al., 2012; Savović et al., 2013a; Savović et al., 2013b). In case of three-dimensional problems solutions are often obtained by the finite element method (Urošević et al., 2003). If problems are one-dimensional they are much easier solved by finite difference method (Savović et al., 2013b). Both methods have advantages and limitations, and the choice between two methods is mostly conditioned by geometry of the problem. For neither does the standard finite discretization explicitly constrain the solutions to positive values, which may lead to numerical instabilities and oscillations of the solution. Moreover there is no unanimous opinion of choice between different finite difference methods for diverse applications.

With the development of computers most algorithms for numerical methods were implemented in a variety of programming languages. In the beginning, during 1970s and 1980s, implicit finite difference methods (IFDMs) were generally first choice. Being often unconditionally stable, the IFDM allows larger step lengths. Despite, this does not increase IFDM's computational efficiency because extremely large matrices must be manipulated at each calculation step. With further advancement of the computers this trend has been changing, shifting the emphasis to explicit finite difference methods (EFDMs). Although EFDM is not unconditionally stable we found that it is also simpler in addition to being computationally more efficient (Savović et al., 2009; Savović et al., 2012; Simovic et al., 2014).

The constant development of numerical methods in search of the best possible solution has led to the proposition of new solutions. Several authors propose new numerical solution of the parabolic differential equations that guarantees positivity of the solutions and that is independent both of the step size in z direction and mesh size (Chen-Charpentier et al., 2013; Liu et al., 2010; Quang et al., 2006). The method works with reaction terms that are the sum of a positive function and a negative function of the unknown – either or both may be zero. It is applicable to both, problems where either advection or diffusion dominates. In this work, a recently reported UPFD scheme and a standard EFD scheme for solving power flow equation are compared to analytical solution for steady-state distribution for glass optical fiber CGW-CGE-68 (Drljaca, 2011).

THEORETICAL PART

Power distribution in optical fiber can be determined by using one of the three methods: ray-tracing method, wave approach and Gloge`s power flow equation. The simplest way that can describe evolution of the power in the multimode optical fibers and account for all important characteristics of the fiber is Gloge`s power flow equation. The Gloge's power flow equation is given as (Gloge, 1972):

$$\frac{\partial P(\theta,z)}{\partial z} = -\alpha(\theta)P(\theta,z) + \frac{D}{\theta}\frac{\partial}{\partial\theta}\left(\theta\frac{\partial P(\theta,z)}{\partial\theta}\right) \qquad (1)$$

where $P(\theta,z)$ is the angular power distribution, z is distance from the input end of the fiber, θ is the propagation angle with respect to the core axis, D is the coupling coefficient assumed constant (Garito et al. 1998; Savovic et al., 2015) and $\alpha(\theta)$ is the modal attenuation. The boundary conditions are $P(\theta_c,z)=0$, where θ_c is the critical angle of the fiber, and $D(\partial P/\partial\theta)=0$ at $\theta=0$. Condition $P(\theta_c,z)=0$ implies that modes with infinitely high loss do not carry power. Condition $D(\partial P/\partial\theta)=0$ at $\theta=0$ indicates that the coupling is limited to the modes propagating with $\theta>0$. After simplification equation (1) becomes (Djordjevich et al., 2000):

$$\frac{\partial P(\theta,z)}{\partial z} = \frac{D}{\theta}\frac{\partial P(\theta,z)}{\partial\theta} + D\frac{\partial^2 P(\theta,z)}{\partial\theta^2} \qquad (2)$$

Numerical solution of equation (2) is obtained by EFDM, used in our previous works (Drljaca, 2011; Savović et al. 2013a; Savovic et al., 2015) and UPFDM proposed by other authors (Chen-Charpentier et al., 2013; Liu et al., 2010; Quang et al., 2006.]. The results thus obtained are compared to the analytical solution of steady-state distribution for the given glass optical fiber:

$$P(\theta,z) = J_0\left(2.405\frac{\theta}{\theta_c}\right)\exp(-\gamma_0 z) \qquad (3)$$

where J_0 is the Bessel function of the first kind and zero order and $\gamma_0\left[\mathrm{m}^{-1}\right] = 2.405^2\ D/\theta_c^2$ is the attenuation coefficient (Drljaca, 2011).

NUMERICAL METHOD

In order to compare results obtained by EFD and UPFD method we considered equation (2) for the same input data used previously (Drljaca, 2011), subjected to following initial and boundary conditions: $P(\theta_c,z)=0$; $D\frac{\partial P(\theta_{=0},z)}{\partial\theta}=0$ (Djordjevich et. al. 2000; Drljaca, 2011; Savović et al., 2013b; Savović et al., 2015; Simovic et al., 2014).

Standard Explicit Finite Difference Method

After applying EFD scheme (Anderson, 1995):

$$\left(\frac{\partial P(\theta,z)}{\partial\theta}\right)_{m,n} = \frac{P_{m+1,n}-P_{m-1,n}}{2\Delta\theta}$$

$$\left(\frac{\partial^2 P(\theta,z)}{\partial\theta^2}\right)_{m,n} = \frac{P_{m+1,n}-2P_{m,n}+P_{m-1,n}}{(\Delta\theta)^2} \qquad (4)$$

$$\left(\frac{\partial P(\theta,z)}{\partial z}\right)_{m,n} = \frac{P_{m,n+1}-P_{m,n}}{\Delta z}$$

equation (2) becomes:

$$\frac{P_{m,n+1}-P_{m,n}}{\Delta z} = \frac{D}{\theta}\frac{P_{m+1,n}-P_{m-1,n}}{2\Delta\theta} + $$
$$+ D\frac{P_{m+1,n}-2P_{m,n}+P_{m-1,n}}{(\Delta\theta)^2} \qquad (5)$$

Truncation errors of the scheme are $O(\Delta\theta^2, \Delta z)$.
When (5) is rewritten in explicit form it becomes:

$$P_{m,n+1} = P_{m,n} + \frac{\Delta z D}{\theta}\frac{P_{m,n+1}-P_{m-1,n}}{\Delta\theta} + $$
$$+ \Delta z D\frac{P_{m+1,n}-2P_{m,n+1}+P_{m-1,n}}{\Delta\theta^2} \qquad (6)$$

Unconditionally Positive Finite Difference Method

After applying UPFD scheme:

$$\left(\frac{\partial P(\theta,z)}{\partial\theta}\right)_{m,n} = \frac{P_{m,n+1}-P_{m-1,n}}{\Delta\theta}$$

$$\left(\frac{\partial^2 P(\theta,z)}{\partial\theta^2}\right)_{m,n} = \frac{P_{m+1,n}-2P_{m,n+1}+P_{m-1,n}}{(\Delta\theta)^2} \qquad (7)$$

$$\left(\frac{\partial P(\theta,z)}{\partial z}\right)_{m,n} = \frac{P_{m,n+1}-P_{m,n}}{\Delta z}$$

equation (2) becomes:

$$\frac{P_{m,n+1}-P_{m,n}}{\Delta z} = \frac{D}{\theta}\frac{P_{m,n+1}-P_{m-1,n}}{\Delta\theta} + D\frac{P_{m+1,n}-2P_{m,n+1}+P_{m-1,n}}{\Delta\theta^2} \qquad (8)$$

When equation (8) is rewritten in explicit form it becomes:

$$P_{m,n+1} = \frac{\hat{D}P_{m+1,n}+P_{m,n}/\Delta z+(\hat{u}+\hat{D})P_{m-1,n}}{1/\Delta z+\hat{u}+2\hat{D}} \qquad (9)$$

where $\hat{u}=-D/\Delta\theta\cdot\theta$ and $\hat{D}=D/\Delta\theta^2$. If the parameters D/θ, and D are all non-negative, and therefore $\hat{u}$ and $\hat{D}$ are both positive, then the numerical scheme represents a UPFD method for any $\Delta z>0$ and $\Delta\theta>0$. In this way, the solutions of the scheme are always positive independently of the choice of space and angle steps [Chen-Charpentier et al., 2013.]. If $D/\theta < 0$, Chen-Charpentier and Kojouharov (Chen-Charpentier et al., 2013) proposed that this term is discretized as $+\frac{D}{\theta}\frac{P_{m,n}-P_{m-1,n+1}}{\Delta x}$ so that the UPFD solution would remain positive. In that case power flow equation is written in the following form:

$$P_{m,n+1} = \frac{\hat{D}\Delta\theta^2 P_{m+1,n} + P_{m,n}(1/\Delta z - \hat{u})}{1/\Delta z + 2\hat{D}} +$$
$$+ \frac{\hat{D}P_{m-1,n} + \hat{u}P_{m-1,n+1}}{1/\Delta z + 2\hat{D}} \qquad (10)$$

Truncation error of the scheme is $O(\Delta\theta + \Delta z)$.

The method (7) proposed by Chen-Charpentier and Kojouharov (Chen-Charpentier et al., 2013) is simultaneously explicit and unconditionally positive, but it is not unconditionally consistent. There are extra truncation error terms because the approximations of the first and second derivatives with respect to θ are evaluated at different lengths. One way to reduce this error is to choose the length step depending on the mesh size so that the inconsistent terms approach zero when the mesh is refined. Second approach is to incorporate these terms into the numerical scheme to achieve a consistent approximation of the original partial differential equation (Chen-Charpentier et al., 2013).

RESULTS

In order to present obtained far-field intensity patterns for numerical calculations we used same fiber that was previously used in different experiments and numerical simulations - CGW-CGE-68 glass optical fiber. The fiber has critical angle $\theta_c = 7.26°$ measured inside the fiber and $\theta_c = 10.6°$ measured in air. Coupling coefficient for this fiber is $D=7.9\times10^{-7}$ rad²/m at room temperature and was used for numerical calculations (Drljaca, 2011). Attenuation coefficient is calculated as $\gamma_0 = 2.86\times10^{-4}$m⁻¹.
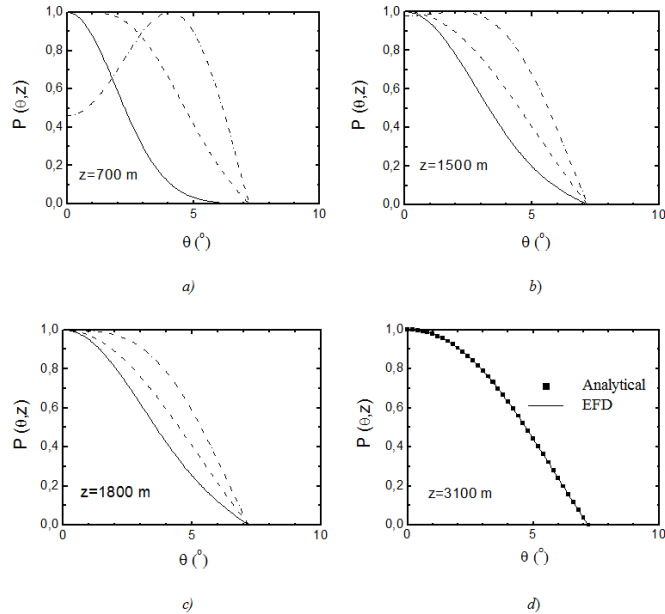

Figure 1. Normalized output angular power distribution obtained by EFD method at different locations along the CGW-CGE-68 fiber for three Gaussian input angles $\theta_0 = 0°$ (solid line), 3° (dashed line) and 6° (dotted line) at: (a) $z = 700$ m ; (b) $z = 1500$ m ; (c) $z = 1800$ m and (d) $z = 3100$ m. [Drljaca, 2011.].

Figure 1. shows normalized far field patterns for different lengths and three different launch angles (θ_0=0, 3 and 6°) obtained by standard EFD method, and analytical solution of power flow equation (2) (Drljaca, 2011). In Figure 2. numerical solutions obtained by UPFD method are presented.

As could be seen from Fig. 1 and Fig. 2 that both EFD and UPFD methods have a good agreement with analytical solution of equation (2). However it could be seen that UPFD scheme is less accurate than EFD scheme when compared to analytical solution. This is due to additional truncation error that occurs in UPFD scheme.
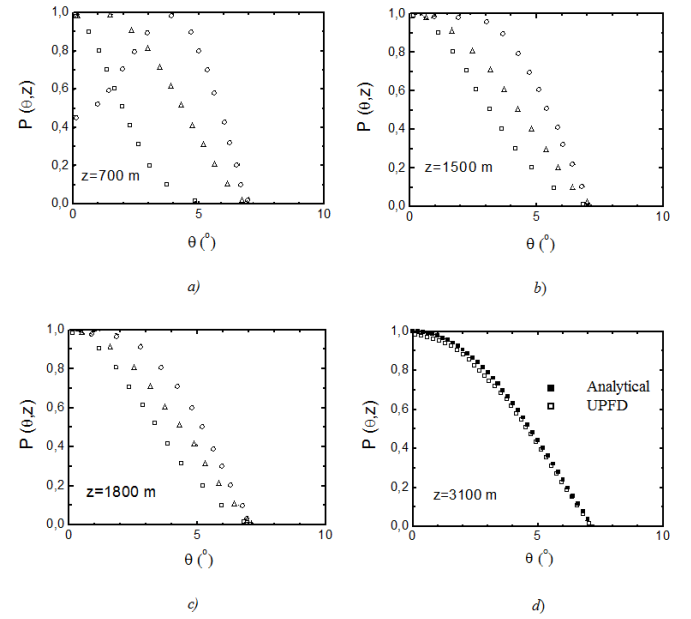

Figure 2. Normalized output angular power distribution obtained by UPFD method at different locations along the CGW-CGE-68 fiber for three Gaussian input angles $\theta_0 = 0°$ (squares), 3° (triangles) and 6° (circles) at: (a) $z = 700$ m ; (b) $z = 1500$ m ; (c) $z = 1800$ m and (d) $z = 3100$ m.

CONCLUSION

Standard explicit finite difference (EFD) scheme and recently reported unconditionally positive finite difference (UPFD) scheme for solving parabolic differential equations are compared to previously obtained analytical solution of power flow equation. We have shown that this scheme is less accurate, even though UPFD scheme guarantees the positivity of the solutions for arbitrary step sizes, and is stable. The reason for this is additional truncation error in the approximations to the first and second derivatives with respect to θ, which are evaluated at different lengths, which is contained in the UPFD scheme. If the accuracy of the numerical scheme over stability is needed we propose usage of EFD scheme before UPFD scheme.

REFERENCES

Anderson, J. D. 1995. Computational fluid dynamics. New York: McGraw-Hill.

Bear, J. 2007. Hydraulics of Groundwater. Dover - Minneola.

Chen-Charpentier, B. M., & Kojouharov, H. V. 2013. An unconditionally positivity preserving scheme for advection–diffusion reaction equations. Mathematical and Computer Modelling, 57(9-10), pp. 2177-2185. doi:10.1016/j.mcm.2011.05.005

Dang, Q. A., & Ehrhardt, M. 2006. Adequate numerical solution of air pollution problems by positive difference schemes on unbounded domains. Mathematical and Computer Modelling, 44(9-10), pp. 834-856. doi:10.1016/j.mcm.2006.02.016

Djordjevich, A., & Savović, S. 2000. Investigation of mode coupling in step index plastic optical fibers using the power flow equation. IEEE Photonics Technology Letters, 12(11), pp. 1489-1491. doi:10.1109/68.887704

Djordjevich, A., & Savović, S. 2013. Solute transport with longitudinal and transverse diffusion in temporally and spatially dependent flow from a pulse type source. International Journal of Heat and Mass Transfer, 65, pp. 321-326. doi:10.1016/j.ijheatmasstransfer.2013.06.002

Drljaca, B. 2011. Modelovanje prostiranja svetlosti kroz višemodna optička vlakna sa stepenastim indeksom prelamanja primenom jednačine protoka snage. Kragujevac: PMF Kragujvac.

Garito, A. F., Wang, J., & Gao, R. 1998. Effects of Random Perturbations in Plastic Optical Fibers. Science, 281(5379), pp. 962-967. doi:10.1126/science.281.5379.962

Gloge, D. 2013. Optical Power Flow in Multimode Fibers. Bell System Technical Journal, 51(8), pp. 1767-1783. doi:10.1002/j.1538-7305.1972.tb02682.x

Hetrick, D. K. 1971. Dynamics of Nuclear Reactors. Chicago: University of Chicago.

Kevkic, T., Stojanovic, V., & Petkovic, D. 2019. Solving Schrödinger Equation for a Particle in One-Dimensional Lattice: An Homotopy Perturbations Approach. Romanian Reports in Physics, 71(101).

Liu, L., Clemence, D. P., & Mickens, R. E. 2010. A nonstandard finite difference scheme for contaminant transport with kinetic Langmuir sorption. Numerical Methods for Partial Differential Equations, 27(4), pp. 767-785. doi:10.1002/num.20551

Murray, J. D. 2002. Mathematical Biology I. Berlin: Springer-Verlag.

Petrović, M., Kontrec, N., & Panić, S. 2017. Determination of accelerated factors in gradient descent iterations based on Taylor's series. The University Thought - Publication in Natural Sciences, 7(1), pp. 41-45. doi:10.5937/univtho7-14337

Savović, S., & Caldwell, J. 2009. Numerical solution of Stefan problem with time-dependent boundary conditions by variable space grid method. Thermal Science, 13(4), pp. 165-174. doi:10.2298/tsci0904165s

Savović, S., Djordjevich, A., & Ristić, G. 2012. Numerical solution of the transport equation describing the radon transport from subsurface soil to buildings. Radiation Protection Dosimetry, 150(2), pp. 213-216. doi:10.1093/rpd/ncr397

Savović, S., Drljača, B., & Djordjevich, A. 2013. Influence of launch-beam distribution on bandwidth in step-index plastic optical fibers. Applied Optics, 52(6), p. 1117. doi:10.1364/ao.52.001117

Savović, S., & Djordjevich, A. 2013. Numerical solution for temporally and spatially dependent solute dispersion of pulse type input concentration in semi-infinite media. International Journal of Heat and Mass Transfer, 60, pp. 291-295. doi:10.1016/j.ijheatmasstransfer.2013.01.027

Savovic, S., Kovacevic, M. S., Bajic, J. S., Stupar, D. Z., Djordjevich, A., Zivanov, M., Drljaca, B., Simovic, A., & Oh, K. 2015. Temperature Dependence of Mode Coupling in low-NA Plastic Optical Fibers. Journal of Lightwave Technology, 33(1), pp. 89-94. doi:10.1109/jlt.2014.2375515

Shih, T. 1984. Numerical Heat Transfer. Berlin: Springer-Verlag.

Simović, A., Savović, S., Drljača, B., & Djordjevich, A. 2014. Influence of intermediate layer on transmission characteristics of W-type optical fibers. Optics and Laser Technology, 57, pp. 209-215. doi:10.1016/j.optlastec.2013.10.024

Urošević, V., & Nikezić, D. 2003. Radon transport through concrete and determination of its diffusion coefficient. Radiat. Prot. Dosim, 104, pp. 65-70.

PHYSICS

Available Online

This journal is available online. Please visit http://www.utnsjournal.pr.ac.rs or http://www.utnsjournal.com to
search and download published articles.